CHARACTERIZATION OF SURFACE PLASMON RESONANCE (SPR) ACTIVE NANOHOLE ARRAY SENSING PLATFORMS:

DEVELOPMENT AND APPLICATION OF NOVEL INSTRUMENTATION AND METHODOLOGY

by

Laurel L. Kegel

A dissertation submitted to the Faculty of the University of Delaware in partial fulfillment of the requirements for the degree of Doctor of Philosophy in Chemistry and Biochemistry

Fall 2013

ProQuest LLC.
789 East Eisenhower Parkway
P.O. Box 1346
Ann Arbor, MI 48106 - 1346

CHARACTERIZATION OF SURFACE PLASMON RESONANCE (SPR) ACTIVE NANOHOLE ARRAY SENSING PLATFORMS:

DEVELOPMENT AND APPLICATION OF NOVEL INSTRUMENTATION AND METHODOLOGY

by

Laurel L. Kegel

Approved: _____

Murray Johnston, Ph.D.
Chair of the Department of Chemistry and Biochemistry

Approved: _____

George H. Watson, Ph.D.
Dean of the College of Arts and Sciences

Approved: _____

James G. Richards, Ph.D.
Vice Provost for Graduate and Professional Education

I certify that I have read this dissertation and that in my opinion it meets the academic and professional standard required by the University as a dissertation for the degree of Doctor of Philosophy.

Signed: _____

Karl Booksh, Ph.D.
Professor in charge of dissertation

I certify that I have read this dissertation and that in my opinion it meets the academic and professional standard required by the University as a dissertation for the degree of Doctor of Philosophy.

Signed: _____

Murray Johnston Ph.D.
Member of dissertation committee

I certify that I have read this dissertation and that in my opinion it meets the academic and professional standard required by the University as a dissertation for the degree of Doctor of Philosophy.

Signed: _____

Sharon Rozovsky, Ph.D.
Member of dissertation committee

I certify that I have read this dissertation and that in my opinion it meets the academic and professional standard required by the University as a dissertation for the degree of Doctor of Philosophy.

Signed: _____

Siu-Tat Chui, Ph.D.
Member of dissertation committee

ACKNOWLEDGEMENTS

I extend many thanks to those who have supported and motivated my doctoral research. The culmination of my graduate school research was preceded by a path full of encouragement and guidance from many. First, I wish to acknowledge my adviser, Karl Booksh, for guiding me through the research process from initial research thoughts to dissemination of results. I have greatly advanced in the way of technical knowledge and more confident, independent thinking through his discussion, facilitation, and ideas. I also thank my colleagues in the Booksh lab, for their discussion, humor, and own interesting research. I have grown through observation and interaction with all of them and am glad to have had enjoyable lab mates. In particular, I would like to thank Nicola Menegazzo for countless discussions, ideas, and inspiration and Devon Boyne for innumerable professional and personal discussions and her giving nature.

I would like to thank the Department of Chemistry and Biochemistry at University of Delaware for providing a rich environment for study, research, and collaboration. I have developed many professional and personal relationships that enhanced my life greatly through insight and friendship. Additionally, the facilities and staff were invaluable to productivity with their knowledge, resources, and kindness. I would like to thank my committee members and collaborators at University of Delaware as well for sharing their wisdom regarding the doctoral process and particulars of ongoing research projects.

I also have tremendous gratitude for the companionship and love from my family and friends. Their relationships offer balance, understanding, wisdom, and fun. I thank my parents, Kim Kegel and J. David Kegel, parents-in-law, Omer and Charmayne Brubaker, and grandparents, Richard and Dawn Kettering, for their support, encouraging words, and camraderie. I also wish to express my appreciation to my siblings for their continued humor, inspiration, and ease of friendship. Of most personal importance, I wish to thank my wonderful husband, Nicholas Brubaker. I appreciate the great character that he exemplifies and am grateful for his unwavering support, spirit, and insight. He is an unconditionally calm, joyful presence, that is a prominent source of positivity and motivation in my life.

TABLE OF CONTENTS

LIST OF TABLES . . . . . **ix**
LIST OF FIGURES . . . . . **x**
ABSTRACT . . . . . **xv**

Chapter

1 INTRODUCTION **1**

1.1 Motivation 1
1.2 Surface plasmon resonance spectroscopy 5
1.3 SPR sensors 8
1.4 Plasmonic nanostructures 12
1.5 Nanostructured SPR sensors 13
1.6 Surface plasmon coupling and gap mode SPR spectroscopy 15
1.7 Overview of dissertation 18

2 NANOHOLE ARRAY SP FEATURES IN VARIOUS OPTICAL CONFIGURATIONS **23**

2.1 Introduction 23
2.2 Nanohole array surface plasmon resonance modes 25
2.3 Nanohole array fabrication by nanosphere lithography 29
2.4 Kretschmann configuration SPR 32
2.5 Transmission mode SPR 35
2.6 Reflection mode SPR 38
2.7 Short range plasmons with azimuthal angle 39
2.8 Conclusion 43

3 DEVELOPMENT AND CHARACTERIZATION OF NIR-SPR INSTRUMENTATION **45**

3.1 Introduction 45

3.2 Experimental methods . . . 47

3.2.1 Instrumentation . . . 47
3.2.2 Gold surface preparation . . . 48
3.2.3 Beam path and optical alignment . . . 48
3.2.4 Bulk Sensitivity . . . 51
3.2.5 Angular calibration and SPR wavelength determination . . . 51

3.3 Incident angle and bulk sensitivity calibration . . . 52
3.4 Parameter selection for high throughput and SPR dip quality . . . 54
3.5 Evaluation of stability metrics for two NIR-SPR accessories . . . 56
3.6 Capability for kinetic measurements . . . 58
3.7 Conclusion . . . 60

4 ADSORBATE-METAL BOND EFFECT ON EMPIRICAL DETERMINATION OF SURFACE PLASMON PENETRATION DEPTH . . . 61

4.1 Introduction . . . 61
4.2 Experimental methods . . . 65

4.2.1 SPR spectroscopy measurements . . . 65
4.2.2 Gold sensor surface preparation . . . 66
4.2.3 Bulk sensitivity calibration . . . 66
4.2.4 Monolayer formation . . . 67
4.2.5 Polyelectrolyte multilayer formation . . . 67
4.2.6 Atomic force microscopy . . . 68

4.3 Determination of penetration depth by alkanethiolate monolayer formation . . . 69
4.4 Toward determination of penetration depth by PEM formation . . . 77
4.5 Calculation of penetration depth of nanohole array surface plasmons . 82
4.6 Conclusion . . . 83

5 SENSITIVITY OF NANOHOLE ARRAY NEAR INFRARED-SURFACE PLASMON RESONANCE SPECTROSCOPY . . . 85

5.1 Introduction . . . 85
5.2 Experimental methods . . . 88

5.2.1 SPR spectroscopy measurements . . . 88
5.2.2 Gold nanohole array sensor surface preparation . . . 89

5.2.3 Sensitivity measurements . . . 89
5.2.4 Atomic force microscopy . . . 90

5.3 Physical characterization . . . 90
5.4 Nanohole array SPR features . . . 90
5.5 Bulk sensitivity . . . 98
5.6 Surface sensitivity . . . 101
5.7 Adsorbate attachment effect on nanohole array l_d and m_{surf} . . . 106
5.8 Conclusion . . . 107

6 PLASMONIC INTERACTION BETWEEN A SINGLE NANOPARTICLE AND A NANOHOLE ARRAY . . . 109

6.1 Introduction . . . 109
6.2 Experimental methods . . . 112

6.2.1 Nanohole array fabrication . . . 112
6.2.2 Atomic force microscopy . . . 112
6.2.3 Integrated AFM-darkfield measurements . . . 113

6.3 Darkfield spectroscopy of nanohole array substrate . . . 116
6.4 Integrated AFM-darkfield spectroscopic imaging . . . 117
6.5 SNP-nanohole array interaction . . . 118
6.6 Additional instrumentation characterization . . . 124
6.7 Conclusion . . . 125

7 CONCLUSION . . . 126

7.1 Main Conclusions . . . 126
7.2 Empirical findings . . . 127
7.3 Implications . . . 129
7.4 Future directions . . . 132

BIBLIOGRAPHY . . . 137

Appendix

A LIST OF ACRONYMS AND SYMBOLS . . . 151

A.1 Acronyms . . . 151
A.2 Symbols . . . 151

B CURRICULUM VITAE . . . 153

C PERMISSION FOR MATERIAL REPRINT 159

LIST OF TABLES

2.1 Procedural details for nanosphere lithography template formation . 31

2.2 Size of single orientation area for different periodicity nanohole arrays 33

3.1 Comparison of the stability metrics for the IR-SPR v2 and Autoseagull accessories 59

4.1 Penetration depth calculated from experimental data with and without adsorbate-metal bond compensation compared to theoretical determination 74

5.1 Theoretical and experimental sensitivity of sample sensitive Bragg SPs supported on various periodicity nanohole arrays 97

5.2 Surface sensitivity improvement for nanohole array as compared to continuous gold substrate 106

6.1 $\Delta\lambda_{SPR}$ from average λ_{SPR} observed for SNP probe or AFM probe in near-contact with stationary nanohole array (n > 40) 122

LIST OF FIGURES

1.1 Proposed lab-on-a-chip device with nanostructured SPR sensing pad 4

1.2 Surface plasmon diagram 6

1.3 SPR spectroscopy excitation diagram and example spectrum 7

1.4 Evanescent surface plasmon field. 8

1.5 SPR sensing principle illustrated as binding of analyte to receptor at SPR sensor surface and corresponding shift in SPR excitation wavelength 9

1.6 Diagram of sample changes which constitute bulk sensitivity and surface sensitivity 10

1.7 LSPR spectroscopy excitation diagram and example spectrum. . . . 13

1.8 Illustration of gap mode SPR enhancement between two nearby plasmonic structures 16

1.9 Factors affecting SPR spectroscopy surface sensitivity 19

1.10 Comparison of penetration depth of continuous gold film and plasmonic nanostructures. 20

2.1 Number of publications on plasmonic hole arrays listed by year . . 24

2.2 Diagram of nanohole array SP modes 26

2.3 Different SPR optical configurations 28

2.4 Schematic of nanohole array fabrication by nanosphere lithography 30

2.5 SEM images of polystyrene bridges formed between nanospheres due to anisotropic reactive ion etching 32

2.6 Optical setup for Kretschmann configuration SPR in the visible region 34

2.7 Representative SPR spectra in visible Kretschmann configuration . 35

2.8 Transmission spectra in air for various periodicity and diameter nanohole arrays 36

2.9 Transmission spectra of nanohole array in air and sucrose solutions 37

2.10 Representative reflectance spectra of nanohole array 39

2.11 Azimuthal angle and different Bragg resonance orders displayed with respect to nanohole array reciprocal lattice 40

2.12 Theoretical Bragg SP λ_{SPR} as a function of azimuthal angle for various periodicity nanohole arrays 41

2.13 Rotational prism-SPR substrate holder for changing azimuthal angle within the Autoseagull NIR-SPR accessory. 42

2.14 Experimental reflection spectra of nanohole array and respective λ_{SPR} at various azimuthal angle 43

3.1 SP penetration depth fitting to different analytes. 46

3.2 IR-SPR Accessory beam-path schematic, photograph, gear schematic, and gear system photograph 50

3.3 Experimental and theoretical IR-SPR spectra at different incident angles 53

3.4 IR-SPR bulk sensitivity at various incident angles 55

3.5 SPR minimum (λ_{SPR}) and peak FWHA/A for various aperture and iris size 56

3.6 Comparative temporal stability of v2 and modified Autoseagull IR-SPR accessories 57

4.1 Diagram of penetration depth of evanescent surface plasmon 63

4.2 Diagram of polyelectrolyte multilayer formation on gold surface . . 68

4.3 SPR shift and SP penetration depth calculated with and without adsorbate-metal bond compensation at various adsorbate thicknesses 70

4.4 Bulk sensitivity of bare and alkanethiolate functionalized gold . . . 71

4.5 Penetration depth as a function of SPR wavelength 76

4.6 Sensorgram of polyelectrolyte multilayer buildup and Measured SPR shift vs. polyelectrolyte thickness 78

4.7 Height determination of bare gold and polyelectrolyte multilayers by AFM 79

4.8 AFM thickness and SPR shift as a function of polyelectrolyte layer number 80

4.9 Polyelectrolyte multilayer refractive index calculated with and without adsorbate-gold bond compensation 82

4.10 Nanohole array surface plasmon penetration depth calculated with and without adsorbate bond effect 83

5.1 Diagram of nanohole array in Kretschmann configuration with sensing and adsorbate volumes illustrated 86

5.2 AFM images of nanohole arrays with various diameter and periodicity 91

5.3 Representative nanohole array SPR spectra demonstrating Bragg and propagating surface plasmons 92

5.4 Nanohole array SPR spectra in air demonstrating Bragg SPs for various nanohole periodicity and diameter 93

5.5 Theoretical excitation wavelength as a function of azimuthal angle and experimental spectra of nanohole array Bragg SPs in air and water for various periodicity nanohole arrays 94

5.6 Theoretical and experimental Bragg SP λ_{SPR} for various periodicity nanohole arrays and Bragg resonance orders 96

5.7 Bulk sensitivity and λ_{SPR} of various diameter nanohole arrays as a function of incident angle 99

5.8 Bulk sensitivity of various diameter nanohole arrays as a function of λ_{SPR} . . . 100

5.9 Bulk sensitivity of various periodicity nanohole arrays as a function of incident angle and λ_{SPR} . . . 101

5.10 SP penetration depth, SPR response to 10 nm thick polyelectrolyte multilayer, and surface sensitivity of various diameter nanohole array substrates . . . 103

5.11 SP penetration depth, SPR response to 10 nm thick polyelectrolyte multilayer, and surface sensitivity of various periodicity nanohole array substrates . . . 104

5.12 SP penetration depth, SPR response to 10 nm thick polyelectrolyte multilayer, and surface sensitivity of continuous gold and nanohole array substrates throughout the near-infrared . . . 105

6.1 Simplified integrated scanning probe microscope and optical spectrometer schematic . . . 114

6.2 Representative normalized darkfield spectrum of nanohole array. . . . 116

6.3 AFM image of nanohole array acquired with SNP probe . . . 117

6.4 AFM image acquired simultaneously with darkfield spectral acquisition, corresponding λ_{SPR} at each measurement point, and SPR image of nanohole array λ_{SPR}. . . . 118

6.5 λ_{SPR} of stationary nanohole array with SNP probe positioned at various spots represented as spatial image and corresponding λ_{SPR} and scatter intensity at each measurement point . . . 119

6.6 λ_{SPR} of stationary nanohole array with SNP positioned at various spots represented as a spatial image, corresponding λ_{SPR} and scatter intensity at each measurement point, and AFM image of nanohole array outlining proposed scanned area . . . 121

7.1 Toward mapping different TERS probe-nanohole array distances and diameters . . . 134

7.2 Proposed nanohole array-nanoparticle sensor with variable gap distance transduction system . . . 135

7.3 Different SPM probe nanoparticle geometries 136

ABSTRACT

Surface plasmon resonance (SPR) active nanohole array substrates offer a diverse biosensing platform with high sensitivity and unique characteristics. This dissertation investigates the sensitivity and fundamental SP features of various nanohole array substrates and demonstrates higher sensitivity than conventional continuous gold platforms, tunability to specific analytes, and great enhancement of the local field intensity. Novel instrumentation and analytical techniques are developed and utilized to assess the nanohole array SPR sensing substrates in the near infrared as well as with interaction of other nanostructures.

The nanohole array substrates are evaluated throughout the near-infrared (NIR) region by novel SPR instrumentation and methodology that extends the working SPR wavelength range and measurement reliability. Development of a robust NIR-SPR instrument allows access to higher wavelength ranges where sensitivity is improved and novel SP modes and plasmonic materials may be investigated. Different aspects of the NIR-SPR instrument, including temporal stability, mechanical resilience and sensitivity, are evaluated and presented. Furthermore, a method is developed for improving precision and accuracy of empirically determined SP penetration depth, a merit of SPR spectroscopy sensitivity. The technique incorporates an adsorbate-metal bonding effect which improves the consistency in the penetration depth value calculated at different adsorbate thicknesses from 41-1089% relative deviation (without bonding effect) to 2-11% relative deviation (with bonding effect). It also improves the experimental agreement with theory, increases the accuracy of assessing novel plasmonic materials and nanostructures, and increases the precision in adsorbate parameters calculated from the penetration depth value, such as thickness, binding affinity, and surface coverage.

Utilizing this NIR-SPR instrument and improved technique for calculation of penetration depth, the sensitivity and various SP modes of the nanohole arrays throughout the NIR range are evaluated, and an improvement in sensitivity compared to conventional continuous gold is observed. Both the Bragg SPs arising from diffraction by the periodic holes and the traditional propagating SPs are characterized with emphasis on sensing capability of the propagating SPs. There are numerous studies on the transmission spectroscopy of nanohole arrays; however this dissertation presents one of the few studies in Kretschmann mode, and the first in the near infrared, where greater surface sensitivity is observed. The sensitivity profile of various nanohole array parameters (periodicity, diameter, excitation wavelength) and SP modes is also presented.

Further control and enhancement of the SP field is pursued by interaction between nanohole array substrate and nanoparticles to exploit field intensification between plasmonic structures, i.e. ,gap mode enhancement. Under specific conditions, the SPs couple together and the electric field between the structures is amplified and localized, which may be exploited for sensing purposes and surface enhanced techniques, including tip enhanced Raman spectroscopy (TERS) or surface enhanced Raman spectroscopy (SERS). A technique for observing nanohole array-nanoparticle distance dependent SP interaction is developed and utilized to demonstrate SP interaction. Scanning probe microscopy controls the position of a single nanoparticle (SNP) affixed to an atomic force microscope probe, and the location specific interaction of the SNP-nanohole array surface plasmons is measured by darkfield surface plasmon resonance spectroscopy. Coupling of the nanoparticle to the nanohole array exhibits a maximum when the SNP resides within a nanohole, which resulted in a maximum SPR wavelength shift of 17 nm and an increase in scatter intensity. This dissertation presents the first empirical observations of SPM controlled gap mode enhancement of more complex nanostructures and allows for optimization of positioning prior to use in sensing.

Chapter 1

INTRODUCTION

1.1 Motivation

The field of plasmonics is extensively studied due to wide-ranging applications including photothermal cancer treatment [1], proteomics [2, 3], biomolecular interaction studies [4, 5], medical diagnostics [6, 7], drug development [8, 9, 10], surface enhanced spectroscopies (fluorescence, Raman, infrared) [11, 12], optics (polarization control, filtering, switching, nonlinear optics, waveguiding, superlensing) [13, 14, 15, 16, 15, 17, 18, 19], data storage [20, 21, 22], photovoltaics [23, 24], and potentially, cloaking [25]. Of these areas, many of the applications utilize the sensing facility of SPR spectroscopy. This dissertation focuses on the characterization of novel substrates and the development of novel techniques for surface plasmon resonance (SPR) spectroscopy sensing, both of which have implications to other applications as well. SPR is sensitive to refractive index changes, and it may be used for detecting sample changes near the sensor surface within a couple hundred nanometers. This length scale is suited for detection of proteins (antibodies [26, 27, 28, 29, 30, 31], antigens [27, 28], enzymes [32]) and small molecules ($<$ 1000 kDa; DNA [33, 34], hormones[35, 36], glucose [37], ammonia[38, 39], pesticides,[40, 41, 42]) in various surface attachment schemes. The sensing capabilities of SPR spectroscopy are employed in medical diagnostics, food safety, environmental monitoring, biomolecular interaction studies, and pharmaceutical development (details of specific SPR sensing analytes are available in several reviews and books on the subject).[7, 43, 6, 44, 45]

SPR sensors exhibit comparable sensitivity to the state-of-the-art techniques for protein quantification in medical diagnostics and demonstrate added advantages

that should advance SPR sensors into the forefront of protein assaying and other sensing technology. The generally used technique is enzyme linked immunosorbent assay (ELISA) which is based on detection of fluorescent markers; however, SPR sensors have demonstrated comparable sensitivity [46, 47] and have added advantages, such as reduced analysis time ($<$ 5 min), small sample volume (μL), and lower cost (approximately \$2 per SPR analysis chip). Additionally, SPR spectroscopy uses smaller instrumentation and may be integrated into lab-on-a-chip type technologies, further reducing the instrument footprint and accessibility (briefly discussed below). Portable SPR instruments are commercially available, whereas ELISA instruments are relatively large bench top instruments. Also, label-free SPR measurements are a better tool for investigating biomolecular interactions, compared to ELISA measurements which require fluorescent labels that affects protein binding interaction.

Current SPR sensing research topics focus on advancements in miniaturization and increasing selectivity and sensitivity.[43, 7, 6] Selectivity is controlled by surface attachment chemistry and passivation chemistry to induce selective attachment of desired analyte and preclude nonspecific adsorption to the sensor. Generally, a linker layer is attached to the sensor surface, followed by the biorecognition element which will bind the analyte in solution. (Details on current research regarding improving selectivity and attachment chemistry are discussed in reviews by Couture et. al. [6] and Homola et. al. [7].) Research on increasing sensitivity involves measurements in the near-infrared rather than conventional visible wavelengths [48, 49], long range surface plasmons (LRSP) [50, 51], nanostructured SPR materials rather than conventional thin continuous films [52, 53, 43, 54], and phase modulation measurements [7]. Of these methods, the investigation of supporting dielectric materials for LRSP is necessary to overcome its decreased SPR imaging capability and decreased surface sensitivity [50, 51] and phase modulation SPR spectroscopy involves interferometry with more complicated analysis and optical setup.[7] Therefore, this dissertation work seeks to investigate increasing sensitivity by use of nanostructures and increased excitation wavelength. A vast amount of research has been conducted on SPR sensing properties

of plasmonic nanostructures,[52, 53, 43] and direct comparison of conventional continuous thin film SPR biosensors to SPR active nanohole arrays (thin metallic films patterned with an array of nanoscale perforations) in the visible wavelength region have demonstrated improved sensitivity for the nanohole arrays.[55] However, other SPR nanostructures have demonstrated little difference from thin film SPR;[56, 57, 58, 59] therefore, this dissertation focuses on the sensing properties of nanohole arrays. Additional advantages of nanostructured SPR sensors include plasmonic field confinement, better spatial resolution, [52, 60, 61], highly tunable SP properties, and unique excitation schemes allowing for in vivo measurements in cells or tissues. [52, 60, 61] The sensing capabilities can be further improved by coupling of nearby surface plasmons,[62] so the improvement of SPR spectroscopy sensitivity of nanohole arrays by coupling with the SP of nearby plasmonic nanostructures is also of interest.

The increased sensitivity of nanohole array SPR substrates could be easily implemented by facile substitution of conventional continuous thin films in current SPR sensing schemes. For example, nanohole arrays SPR sensing pads could be practically realized in lab-on-a-chip type devices [63] that combine pretreatment of crude sample and SPR spectroscopy of the analyte (Figure 1.1). This type of device could be implemented for point-of-care measurements in commercially available portable SPR instruments. SPR active nanohole arrays could also be employed in multiplexed setups where several analytes in specific locations on the sensors surface are simultaneously imaged and quantified. Generally, analyte specific areas are distinguished by patterning complementary biorecognition elements on thin films.[64, 65] Nanostructures offer distinct domains which facilitate additional improvements in spatial resolution and greater multiplexing capacity.[52, 66] Additionally, nanohole array fabrication is fairly facile, and nanohole array SPs may be excited in alternative excitation modes which allow for further miniaturization and simplification of instrumental setup.[6] The ease of implementation and the aforementioned advantages over conventional continuous thin film SPR further motivate the investigation of improved sensitivity of such SPR active nanohole arrays. Herein, the characterization of nanohole array SPR sensing substrates

and development of analytic SPR techniques and instrumentation are presented.

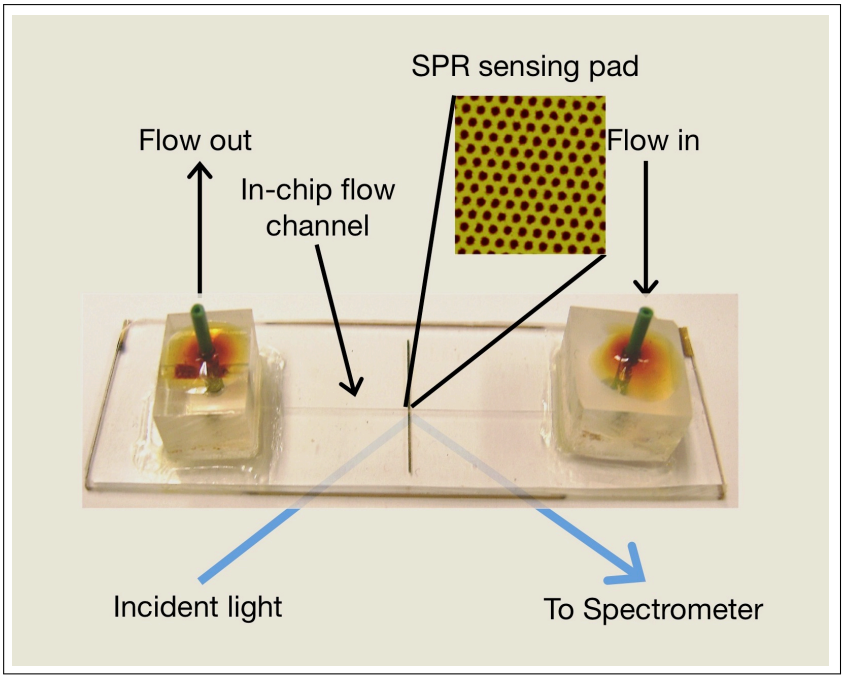

Figure 1.1: Proposed lab-on-a-chip device with nanostructured SPR sensing pad.

This dissertation investigates the combined power of individually proposed methods for increasing sensitivity; nanohole array sensing substrates, increased excitation wavelength value and range, and interaction of nanostructured SPs. The properties and sensitivity of SPR active nanohole array sensing substrates are investigated in the near infrared and in interaction with a gold nanosphere. Novel instrumentation and techniques are also presented with the motivation to explore different wavelength regions, determine region of greatest sensitivity, allow tunability, and investigate interaction of nanohole array SPs with a nanoparticle. Additionally, the accuracy and consistency of a method for assessing a primary surface plasmon property, penetration depth into the sample, is improved and invoked in analysis. These novel instrumentation and analytical techniques are developed and utilized to assess the properties and increased sensitivity of nanohole array SPR sensing substrates in the near infrared and with interaction of other nanostructures.

1.2 Surface plasmon resonance spectroscopy

The first characterization of the phenomenon of SPR is credited to both Otto [67] and Kretschmann and Raether [68] in 1968, and detailed discussions of surface plasmon (SP) properties are widely available. [44, 45, 69] A brief discussion of theory is provided in this section. A surface plasmon is a collective oscillation of electrons at the interface of a plasmonic material, generally a metal (m) and dielectric sample (s), where $\epsilon'_m < -\epsilon'_s$ and ϵ is complex permittivity of the given material (Figure 1.2). Generally, this condition is fulfilled by a thin plasmonic metal film (relatively large $-\epsilon'_m$) and a dielectric sample ($+\epsilon'_s$). A surface plasmon is excited at the metal/sample interface by incident light when the in-plane component ($\mathrm{k_x}$) is resonant with the SP wavevector ($\mathrm{k_{sp}}$);

$$\mathrm{k_{sp}} = \mathrm{k_x} \tag{1.1}$$

k_x depends on the angle of incidence (θ_{inc}) and the refractive index of the incident medium through which light travels (η_{inc});

$$\mathrm{k_x} = (2\pi/\lambda)\eta_{\mathrm{inc}} \sin\theta_{\mathrm{inc}} \tag{1.2}$$

k_{sp} is represented by the following equation where λ is the wavelength of light and ϵ_m and ϵ_s are the complex permittivity of the metal and dielectric sample;

$$\mathrm{k_{sp}} = \frac{2\pi}{\lambda}\sqrt{\frac{\epsilon_s \epsilon_m}{\epsilon_s + \epsilon_m}} \tag{1.3}$$

As $\mathrm{k_{sp}}$ depends on ϵ_s, the coupling conditions change with a change in sample refractive index (η_s); $\epsilon_s = (\eta_s + ik_s)^2$ where k is the imaginary refractive index component. This is the basis for SPR sensing, as η_s changes a change in the coupling conditions is transduced.

SPs on thin films cannot be excited by directly incident light, because the wavevector cannot match the energy of the SP wavevector ($\mathrm{k_x} < \mathrm{k_{sp}}$). Instead, a

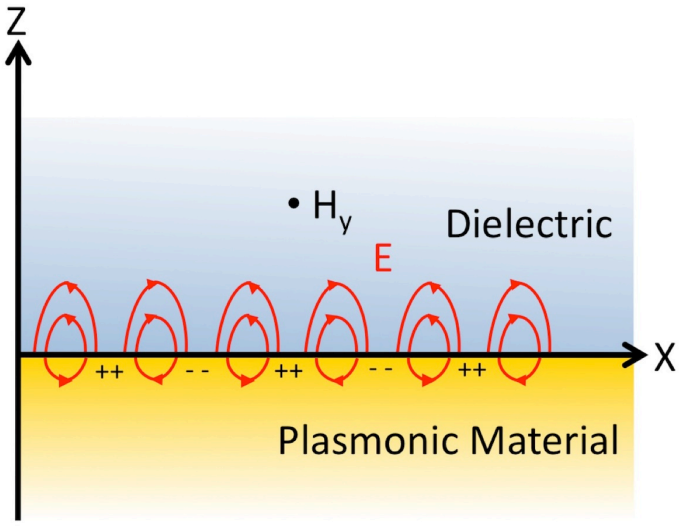

Figure 1.2: Surface plasmon diagram illustrating the collective oscillation of the electrons at the dielectric/plasmonic material interface. Relative to the direction of surface plasmon propagation, the magnetic field (H_y) is perpendicular and the electric field (E) is parallel.

grating or prism is used to increase the wavevector and shift the light line to intersect the SP wavevector, at which point $k_x = k_{sp}$. Most commonly, a prism is used to couple light into the backside of the SPR sensor by attenuated total reflection in the Kretschmann configuration. This type of setup is widely implemented in commercially available SPR instruments and is commonly built in research labs with custom optics. A comprehensive list of commercial bench top and portable SPR spectrometers is available in [70, 6].

When the incident light couples into and excites the SP, it is perceived as an absorption in the SPR spectrum (Figure 1.3). In a constant angle setup, an absorption peak at a specific wavelength (λ_{SPR}) is measured. The surface plasmon is excited by p-polarized (TM) light which has a perpendicular component of the electric field that may excite the surface plasmon. Correspondingly, s-polarized (TE) light cannot excite a SP and may be used as a reference for the SPR spectra. Thereby, SPR spectra are collected as a ratio of reflectivity of p-polarized light to s-polarized light.

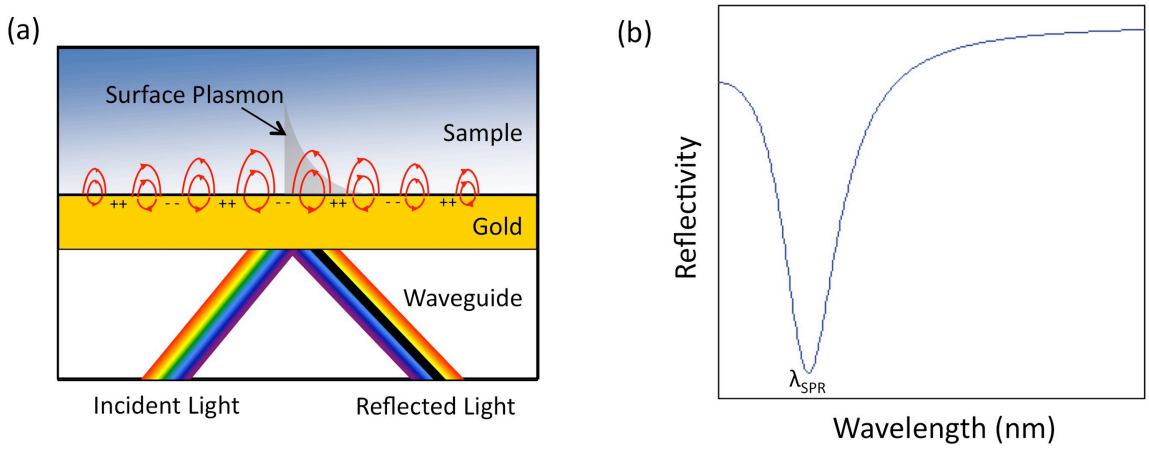

Figure 1.3: SPR spectroscopy (a) excitation diagram and (b) example spectrum.

The SP has a characteristic propagation length along the interface and penetration depth into the sample, which both depend on the material properties and dictate the sensing capability. Gold will be considered for the following discussion, because it is the foremost plasmonic material due to its sensitive plasmonic features (second to silver) and relatively inert and stable chemistry.[71] The imaginary component of its complex permittivity dampens the SP wave and affects its propagation length, as illustrated in figure 1.3(a). A SP propagates for 10s-100s of microns on thin gold films (approximately 50 nm thick).[72] The propagation length affects the area of interaction and the imaging capability of the system. Additionally, the SP is an evanescent wave that decays exponentially into the sample material (Figure 1.3(a)) and into the metal to a lesser extent (not shown). Thereby, the SP wave is more sensitive near the surface and the sensing depth is characterized by the penetration depth of the SP, i.e. the distance from the interface where the intensity of the plasmonic field decays to 1/e, Figure 1.4. The SP is most sensitive to adsorbates and sample RI within this region, and there is little shift observed for RI changes above this penetration depth.

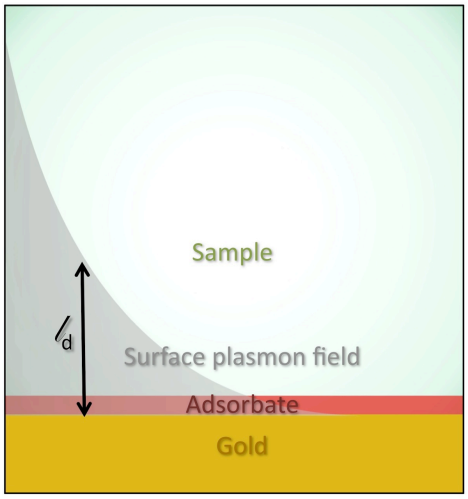

Figure 1.4: Evanescent surface plasmon field illustrating the SP penetration depth (l_d) into the dielectric.

1.3 SPR sensors

The specific excitation wavelength (λ_{SPR}) depends on sample RI, as detailed above. Accordingly, a $\Delta\lambda_{SPR}$ occurs with change in sample refractive index (RI) (Figure 1.5). This is used for biosensing by functionalizing the sensor surface with a specific biorecognition element (antibodies, aptamers, peptides, etc...) [7] which subsequently binds the corresponding particular analyte to the surface. In this way, the biorecognition elements render the sensor selective to the analyte of choice, an increase in refractive index is measured upon analyte binding to the biorecognition element, and the SPR response is related to concentration. By this principle, SPR spectroscopy is a universal detection method where potentially disruptive labeling of the analyte is unnecessary. Additionally, unlike other optical absorption/transmission based methods, measurements may be acquired in real time, and the sample can be opaque or scattering (i.e. biological fluids).

The response to a given adsorbed analyte, i.e. surface sensitivity, is affected by the sensitivity to bulk solution change, i.e. bulk sensitivity, and the depth of the plasmonic field region, designated by the SP penetration depth.[7] A change in refractive index ($\Delta\eta = \eta_1 - \eta_2$) within the SP penetration depth will effectively cause a $\Delta\lambda_{SPR}$,

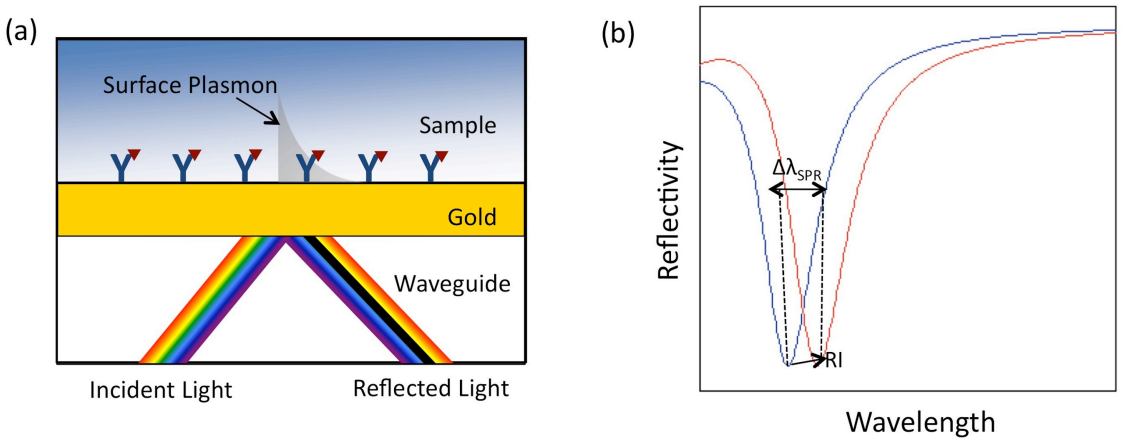

Figure 1.5: SPR sensing principle illustrated as (a) the analyte (antigen depicted as red triangle) binding to the receptor (antibody depicted as blue Y) and (b) the corresponding shift in SPR excitation wavelength.

however the magnitude of the response depends on the proportion of the plasmonic field where sample change occurs.[7] Binding of an analyte which extends through only a fraction of the SP penetration depth causes a smaller response than if it would occupy the entire SP penetration depth. The entire plasmonic field experiences a change when a bulk sample RI change occurs (Figure 1.6(a)), and the $\Delta\lambda_{\mathrm{SPR}}$/RIU for this bulk change is the bulk sensitivity (m). When a thin adsorbate layer, such as a protein-protein pair, adsorbs to the surface, only a fraction of the plasmonic field is occupied (Figure 1.6(b)). The sensitivity to an adsorbate is known as surface sensitivity and the $\Delta\lambda_{\mathrm{SPR}}$ depends on the penetration depth (l_{d}) and thickness of analyte (d):[73]

$$\Delta\lambda_{\mathrm{SPR}} = \mathrm{m}\Delta\eta[1 - \exp(-2\mathrm{d}/l_d)] \tag{1.4}$$

Surface sensitivity is the primary figure of merit for a sensing substrate, as the ultimate detection limit of the system depends on the surface sensitivity to a given analyte (particular to the sensing platform) and the noise of the system (particular to the instrumental setup). Optimal surface sensitivity arises from high bulk sensitivity and SP penetration depth well matched to analyte thickness. The typical penetration depth

of a SP on a thin gold film is approximately 300 nm,[44] thereby SPR sensors are suited to analytes within this size domain.

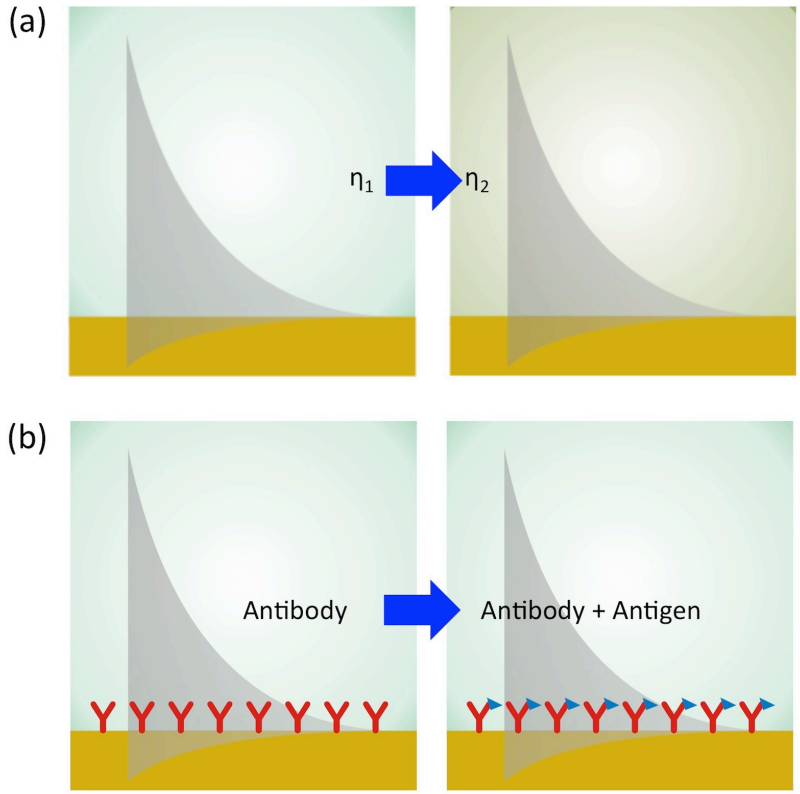

Figure 1.6: Diagram of (a) change in bulk solution refractive index (η) throughout the entire SP penetration depth and (b) analyte adsorption near the surface which occupies a fraction of the SP penetration depth. The $\Delta\lambda_{\mathrm{SPR}}$ for given RI changes represent (a) bulk sensitivity and (b) surface sensitivity.

Current SPR measurements are highly sensitive and can measure diagnostic protein levels in interfering matrix. SPR spectroscopy can detect changes in sample refractive index (RI) as small as 10^{-6} to 10^{-7} refractive index units (RIU), the equivalent to an RI shift from a 0.01°C to 0.001°C temperature change of water.[7, 74, 75] This corresponds to diagnostic protein levels where pg/mL to ng/mL concentrations are easily measured [76, 7, 43, 6] and ng/mL detection in mg/mL interfering protein has been established [77, 26]. Diagnostic analyte concentrations for numerous diseases

have been detected by SPR including myocardial infarction [26], cancer[27, 28], hepatitis [29], and diabetes [30, 31]. Also, the analysis of protein binding mechanisms is widely investigated by SPR spectroscopy, as protein kinetic studies require nM range detection in real-time.[43, 44, 78, 5] SPR sensing facilitates the study of protein binding constants [44, 4] and possible binding pairs for medicine, bacteriology, virology, cell biology, proteomics, and molecular engineering.[79, 2, 3] with the added advantages of measurements free of labels that may disrupt the native protein interactions of interest, fast analysis time (¡ 5 min), low cost, and small instrument footprint.

In addition to the direct receptor-analyte scheme, other bioreceptor framework may be implemented to amplify signal and enable detection of small molecules ($<$ 1000 kDa) or generally increase sensitivity.[43, 7] The larger the analyte, generally, the larger the response, so many assays implement an alternative scheme which uses a larger adduct in conjunction with the analyte to amplify the signal. Competitive assays are performed in a solution with both the analyte and an added larger, conjugated version of the analyte (e.g. analyte attached to a nanoparticle). In this case, the response to the conjugated analyte is greater than the free analyte, so the signal is inversely proportional to the analyte concentration. Inhibition assays are performed in solutions with the analyte and antibody mixed. The sensor surface has pre-attached analyte molecules, so antibodies which have not previously bound to analyte in solution will bind to the surface, creating an inverse response to analyte concentration. Sandwich assays implement the direct assay of analyte binding to a pre-bound antibody, then a secondary antibody is added which binds to the analyte and creates a larger response. Further response amplification for sandwich assays may be achieved by tagging the secondary antibody with a gold nanoparticle [80, 81] or latex particle.[82] Enzyme amplification may be used in which an enzyme reacts with the analyte and the binding element to destroy the binding element and release the analyte back into solution to continue the cycle. This technique allows for highly sensitive measurement of an inverse response as the binding element is removed from the surface.[33, 34, 83] Another method implements the attachment of selective polymers which bind the analyte, such

as molecularly imprinted polymers for detection of glucose[37] or polyaniline for detection of ammonia[39]. These methods improve detection limits and allow for detection of small analytes, however, analysis time is increased (not real-time) and more reagents are required (more expensive).

1.4 Plasmonic nanostructures

Plasmons cannot freely propagate in plasmonic materials with structures smaller than the wavelength of light; rather, a localized surface plasmon is excited by resonant incident light which has unique SPR sensing potential and application in other areas, including photothermal cancer treatment [1], surface enhanced spectroscopies [11, 12], optics [13, 14, 15, 16, 15, 17, 18, 19], data storage [20, 21, 22], etc... A localized surface plasmon (LSP) is an oscillation of electron density with respect to the ion lattice induced by an applied electric field and a restoring force to equilibrate the resulting charge imbalance within the nanoparticle (Figure 1.7(a)).[66, 52, 84] The conduction electrons within the nanostructure shift upon plane-wave excitation and the resulting polarization within the nanostructure causes a temporal oscillation of the electrons. An optical frequency exists that is resonant with this electron oscillation. The resonance enhances the field within the nanoparticle and causes an energy absorption and scattering maximum. The Mie theory [85] describes the extinction (combined scattering and absorption) of a spherical nanoparticle by the following solution of Maxwell's equations; [86]

$$E(\lambda) \propto \frac{\epsilon_{m,i}}{(\epsilon_{m,r} + \chi\epsilon_{\mathrm{s}}) + \epsilon_{m,i}^2} \tag{1.5}$$

where $\epsilon_{m,r}$ and $\epsilon_{m,i}$ are the real and imaginary components of the metal complex permittivity, ϵ_s is the complex permittivity of the surrounding sample, and χ is a geometry factor for considering nanoparticle aspect ratio. An extinction maximum $E(\lambda)$ occurs at a resonant frequency, λ_{LSPR}, when $\epsilon_{m,r}(\omega)+2\epsilon_s = 0$, assuming $|\epsilon_{m,r}| >> \epsilon_{m,i}$ (Figure 1.7(b)). This model for the extinction maximum of simple nanostructures is well established.

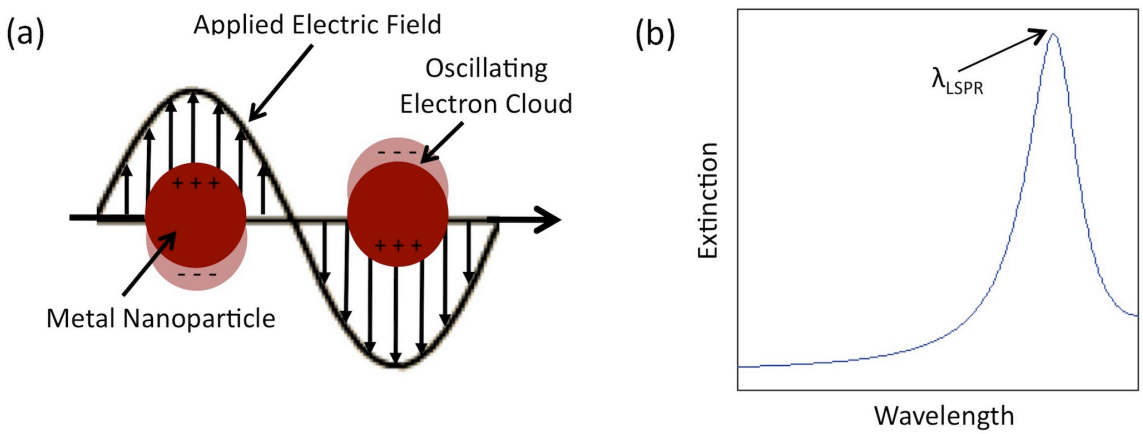

Figure 1.7: LSPR spectroscopy (a) excitation diagram and (b) example spectrum.

Larger and more complex nanoparticles do not adhere to this simple model. The LSPR excitation principle remains similar; however, there may be several LSPs excited within more complicated structures. For nanoparticles larger than the Rayleigh approximation ($d > 30$ nm), depolarization effects occur which cause multipolar LSPR in various orders, red-shifting of the resonant frequency, and dampening of the LSPR. Particulars of numerous nanostructure geometries have been investigated for their unique LSPR properties, including nano- rods, spheres, triangles, rings, shells, cubes, crescents etc... [66, 52, 87, 84, 88, 89] In these cases, LSPR properties may be modeled by discrete dipole approximation [90, 91], finite difference time domain [92, 93], or rigorous coupled wave analysis [94].

1.5 Nanostructured SPR sensors

LSPs are sensitive to sample refractive index as observed in equation (1.5), so they may be used for sensing near-surface binding events similar to propagating SPs. Contrastingly, LSPs are non-propagating, radiative surface plasmons that localize and enhance the electric field around the nanostructure, and they do not require additional momentum increase from the directly incident light line. They may be excited directly,

which offers alternative excitation modes and lends to miniaturization and simplification of optical setups. Additionally, the penetration depth of SPs supported on nanostructures is smaller than the penetration depth of propagating SPs, which may lead to increased surface sensitivity and reduced sensitivity to temperature fluctuations, as discussed in section 1.3.[84] In the visible wavelength region, penetration depth (l_{d}) of nanostructure SPs is 12nm $< l_{\mathrm{d}} <$ 300nm [95, 54, 96] compared to $l_{\mathrm{d}} = 270 - 320$ nm for thin gold films.[97] As such, biosensors based on plasmonic nanostructures have been widely investigated, with numerous reviews on the subject.[52, 53, 84, 98, 99] Comparisons of surface sensitivity of LSPR sensors based on nanostructured thin films of nanohole arrays [55] have demonstrated a marked improvement in surface sensitivity compared to continuous gold films in the visible wavelength region. However, nanotriangles [56], nanodisks[57], and nanorods [58] have shown little difference from conventional SPR biosensors. Thereby, this dissertation is particularly interested in nanohole array SPR substrates.

The increased sensitivity of nanohole arrays arises from complex SP characteristics, and the understanding of these SPs allows for their manipulation and application. Briefly, SPR sensors based on both 2D periodic (hole arrays) and 1D periodic (single slit) nanostructured thin films support various SPR modes, including localized, short range, and propagating SPs, and their interaction may increase sensitivity.[55, 100, 101] The various SPs may be excited in different optical modes, including transmission, Kretschmann configuration, and reflection, because the periodic nanostructures act as a built-in grating to diffract light and fulfill momentum matching requirements for SP excitation. Of particular interest, transmission mode has exhibited similar sensitivity to continuous thin film SPR spectroscopy[102, 103], and Kretschmann configuration interrogation has exhibited up to 1.6× greater sensitivity than continuous thin film SPR spectroscopy [55, 54]. (Details of the SP and excitation modes are discussed in chapter 2.) Other nanostructured thin films that may have similar traits include corrugated films and groove gratings, but SPR studies on these substrates has been limited. SPR spectroscopy of corrugated gold films in Kretschmann configuration has

been simulated and demonstrated a theoretical $6-7\times$ improvement over conventional continuous gold films.[104] Additionally, a study on groove gratings exhibited LSPR bulk sensitivity $> 10\times$ lower than continuous gold [105], and similar sensitivity when excited indirectly.[106, 107]

In addition to increased sensitivity, the unique SP characteristics of nanostructured SPR sensors offer other practical advantages. The highly confined plasmonic field increases the absolute detection limit due to reduced binding area, and it offers better spatial resolution for multiplexing purposes. [52, 60, 61] Nanostructures also enable a novel multiplexing technique in which, rather than spatially separated measurements, nanostructures of various physical parameters with different SPR signatures are utilized within one sensing region. In this case, different analytes on different plasmonic nanostructures have been simultaneously measured at different wavelengths. [108, 109, 110] This is easily implemented because nanostructure SP characteristics (penetration depth, excitation wavelength, field strength, penetration depth, etc...) are highly tunable by physical parameters. This tunability also allows for controlled enhancement and tuning of SP sensitivity. Furthermore, isolated plasmonic nanostructures excited in transmission mode may be implemented in instances where thin films cannot, such as in vivo measurements in cells or tissues. [52, 60, 61] Sensing capabilities can be further improved by more elaborate sensing schemes that involve the coupling of surface plasmons.

1.6 Surface plasmon coupling and gap mode SPR spectroscopy

The interaction of surface plasmons can increase the intensity and localization of the plasmonic field, and ultimately SPR sensing capability. When the plasmonic fields of two nearby structures interact, gap mode enhancement occurs and the field intensity within the gap between the structures is increased by up to five orders of magnitude.[62] The field enhancement occurs due to an increase in composite dipole moment and depends on the polarization direction of incoming light, gap distance, and plasmonic structure dimensions (Figure 1.8). Gap mode interaction is greatest

for light polarized parallel to the inter-particle axis, along the direction of gap and k_z.[62] Additionally, the modification of the SP mode depends on the distance between the structures (d) and nanostructure diameter (D). As the gap distance decreases, the field becomes more localized and enhanced within the gap, and a spectral shift occurs. The relative intensity within the gap drastically increases, until the system's resonant distance (d_{res}) is reached, and the greatest gap mode enhancement occurs. Then, as $d < d_{res}$, intensity begins to decrease again.[111, 112] Generally, d_{res} correlates to distances below 0.2 to 0.5× D.[112, 62] In addition to increased intensity, an increase in the confinement of the plasmonic field also occurs. Konopsky et. al. [111] derived the width of the LSP in gap mode, L, for a nanosphere and continuous thin film as follows:

$$L \approx \sqrt{dD} \tag{1.6}$$

Thus, the SP field is further confined when $d < D$. This translates to lower detection limits in SPR sensing and greater multiplexing capabilities.[66, 52, 60]

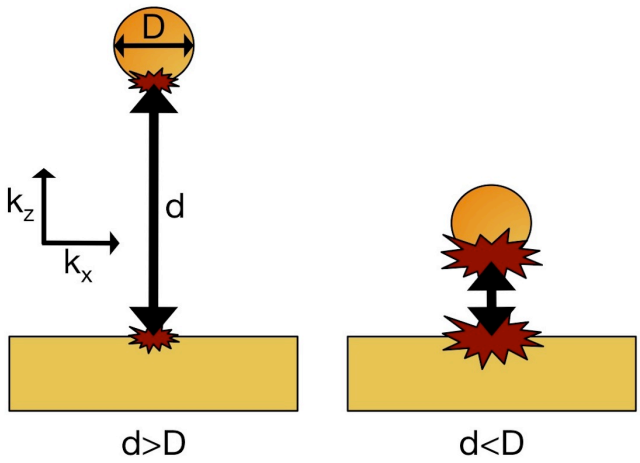

Figure 1.8: Illustration of gap mode SPR enhancement between two nearby plasmonic structures, pictured as a metal nanosphere and thin continuous film. The enhancement increases as the distance between the nanosphere and thin film decreases to $d < D$. k_x and k_z represent the x and z components of the incident wavevector.

Gap mode SPR spectroscopy has been a topic of current research for increasing

SPR sensing capability and enhancing Raman signal between nanostructures. SP coupling of plasmonic nanostructures to other plasmonic nanostructures or thin films can greatly increase SPR sensitivity [1, 113, 114], and tuning the SPs to a highly resonant window (both λ_{SPR} within ≈ 100 nm) provides additional enhancement.[100, 115, 116] For example, response to binding of bovine serum albumin was increased by up to 6× for metal nanoparticle dimers as compared to parallel isolated metal nanoparticles.[117] SP coupling is also utilized in LSPR sensors based on the aggregation of nanoparticles. The LSP greatly redshifts or diminishes as isolated nanoparticles aggregate into a larger compound structure. [118, 119] Another type of gap mode SPR sensors, called plasmonic rulers, detect small distance changes between two nanoparticles. Distance between nanoparticles joined by an analyte (e.g. DNA) changes with conformational change and length of the analyte, and is thereby transduced into a large SPR shift.[120, 121]

Gap mode enhancement applies to tip or surface enhanced Raman spectroscopy (TERS and SERS) as well. Briefly, the working principle for SERS and TERS is enhancement of both the laser light and the Raman scatter by the plasmonic field of either a nanostructured substrate (SERS) or a metal nanoparticle attached to the tip of an atomic force microscopy probe (TERS). The Raman signal from within the enhanced field can be resolved from far-field background signal, thereby isolating the enhanced, localized chemical information. Gap mode enhancement can improve the limit of detection for both SERS and TERS [122, 101, 123, 124] and may improve the resolution for chemical mapping by TERS. Generally, TERS resolution reaches sub-diffraction limits dependent on the nanoparticle diameter, but localization of the plasmonic field within the gap can produce sub-tip diameter resolution. By equation (1.6), the plasmon field may be confined to smaller dimensions than the tip diameter, D. Thus, when the distance between the structures is less than the particle diameter, sub-tip resolution is achievable.[111]

1.7 Overview of dissertation

As discussed in the preceding material, a main focus of SPR sensor research is improving surface sensitivity. This dissertation explores sensitivity optimization through tuning SP characteristics to particular analytes and conditions. Particularly, the SPR excitation wavelength and SP penetration depth are investigated due to their influence on surface sensitivity (Figure 1.9). For a given analyte of relative size as pictured in figure 1.9, a smaller penetration depth will induce a greater response due to the closer match between analyte volume (V_a) and SP sensing volume (V_s). Comparatively, the analyte occupies less of the SP field for a larger V_s and produces a smaller $\Delta\lambda_{SPR}$ for the given analyte. Furthermore, the penetration depth dictates the distance above the surface where the field enhancement occurs and the analyte should be positioned for SP enhanced spectroscopies. Both the bulk sensitivity[45, 125] and penetration depth[44] increase with SPR excitation wavelength, λ_{SPR}, and may be optimized to particular analytes.

The development of highly stable NIR-SPR instrumentation is investigated in chapter 3 to access higher SPR excitation wavelengths past the conventionally used visible wavelength region. Higher wavelength regions offer increased bulk sensitivity and facilitate study of novel nanostructured materials with features in this region. The developed accessory is more accessible than previously developed accessories, because it utilizes the source and detector of a commercial FTIR spectrometer and requires less initial investment and alignment (Refer to section 3 for more information). Enabling excitation wavelength range from the visible to NIR regions also facilitates tunability of SP penetration depth. However, with increased λ_{SPR} there is also an increase in SP penetration depth; $l_d = 270 - 1630$ nm for $\lambda_{SPR} = 693 - 1560$ nm is theoretically determined from Maxwell's equations. The use of nanostructures may reduce the penetration depth by estimates of up to 10×, as evidenced by data collected in the visible range (Figure 1.10). [95, 54, 96]

The accuracy of calculating penetration depth values is important to assessing

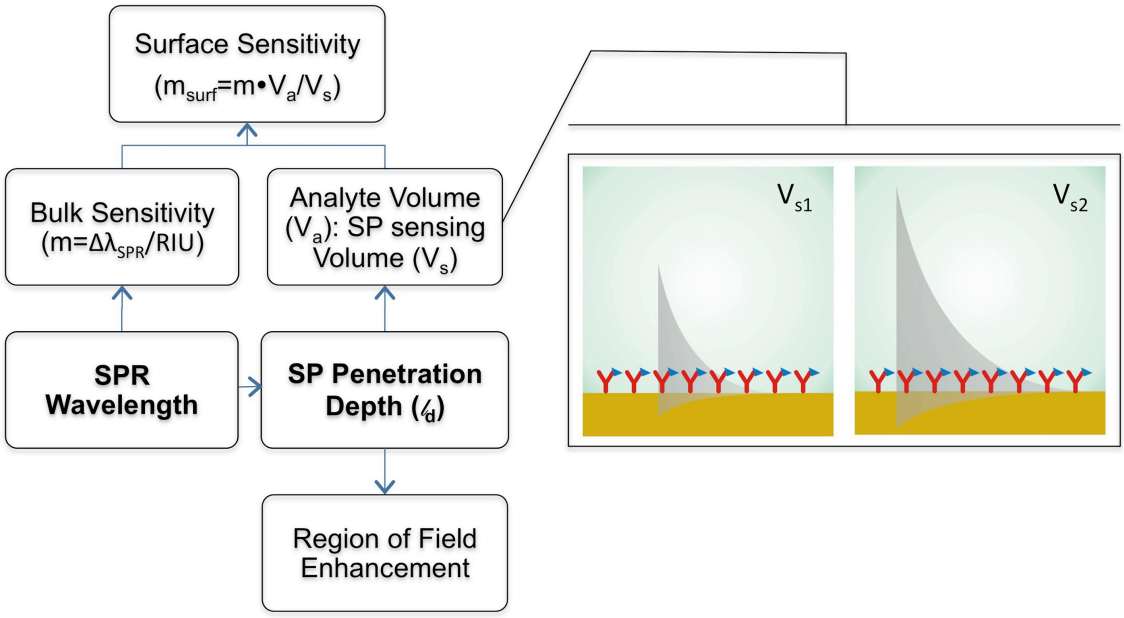

Figure 1.9: Factors affecting SPR spectroscopy surface sensitivity (m_{surf}). The SP field diagrams depict different l_d, and thereby V_s, with the same V_a; $V_a/V_{s1} > V_a/V_{s2} \rightarrow m_{surf1} > m_{surf2}$

.

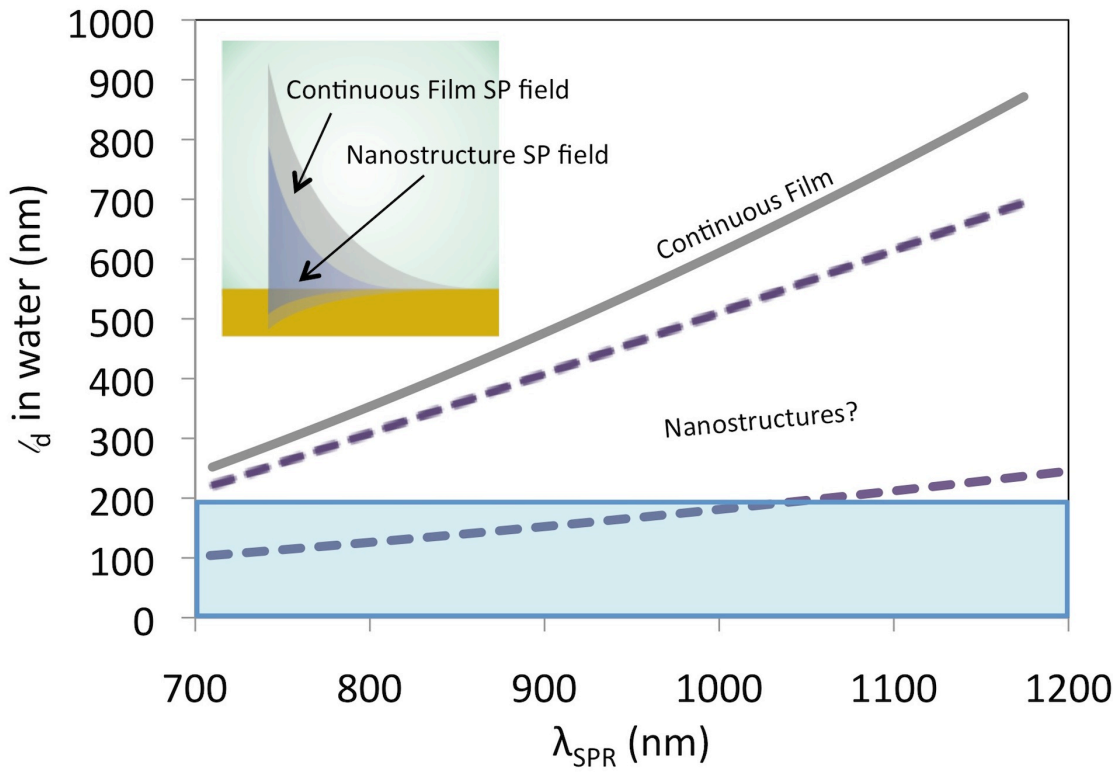

Figure 1.10: Comparison of theoretical penetration depth of continuous gold film (grey) and projected penetration depth of plasmonic nanostructures (purple). The blue box indicates the thickness of the general SPR spectroscopy analytes where, if penetration depth was reduced to these distances, optimal V_a/V_s would be attained.

these novel nanostructured substrates, therefore an improvement upon previous experimental methods is established by accounting for adsorbate-gold bonding effects and is presented in chapter 4. The technique incorporates an adsorbate-metal bonding effect which improves the consistency in the penetration depth value calculated at different adsorbate thicknesses. It also improves the experimental agreement with theory, increases the accuracy of assessing novel plasmonic materials and nanostructures, and increases the precision in adsorbate parameters calculated from the penetration depth value, such as thickness, binding affinity, and surface coverage.

The decreased penetration depth of nanostructures, and increased bulk sensitivity with increasing λ_{SPR} motivates the investigation of nanostructures in the near infrared (NIR). In particular, SP active nanohole arrays are investigated throughout the NIR. Utilizing the NIR-SPR instrument and improved technique for calculation of penetration depth, the sensitivity and various SP modes of the nanohole arrays throughout the NIR range are evaluated, and an improvement in sensitivity compared to conventional continuous gold is observed. Both the Bragg SPs arising from diffraction by the periodic holes and the traditional propagating SPs are characterized with emphasis on sensing capability of the propagating SPs. There are numerous studies on the transmission spectroscopy of nanohole arrays; however this dissertation presents one of the few studies in Kretschmann mode, and the first in the near infrared, where greater surface sensitivity is observed. The sensitivity profile of various nanohole array parameters (periodicity, diameter, excitation wavelength) and SP modes is also presented.

Potential for further field enhancement and increased SPR sensitivity by SP coupling between nanohole arrays and a plasmonic nanosphere is also explored. As previously discussed, gap mode enhancement occurs under specific conditions, which amplifies and localizes the SP field and may be exploited for sensing purposes and surface enhanced techniques, including tip enhanced Raman spectroscopy (TERS) or surface enhanced Raman spectroscopy (SERS). A technique for observing nanohole array-nanoparticle distance dependent SP interaction is developed and utilized to

demonstrate SP interaction. Scanning probe microscopy controls the position of a single nanoparticle (SNP) affixed to an atomic force microscope probe, and the location (axial and lateral) specific interaction of the SNP-nanohole array surface plasmons may be measured by darkfield surface plasmon resonance spectroscopy. This dissertation presents the first empirical observations of SPM controlled gap mode enhancement of more complex nanostructures and allows for optimization of positioning prior to use in sensing.

An outline of the dissertation is as follows. Chapter 2 discusses the various SP types and excitation modes of plasmonic nanohole arrays. The facile fabrication method is presented with emphasis on the ease of structural parameter control, which affects the SP properties and may be used for tuning accordingly. Chapter 3 describes the development and characterization of an SPR instrument enabling measurements in the NIR range with improved robustness and temporal stability compared to a previous NIR-SPR instrument. Chapter 4 presents an improvement to the current empirical method for calculation of SP penetration depth. Consideration of bonding effects on the gold permittivity, and subsequently the SPR conditions, increases the accuracy and consistency of the calculation. This method and the instrumentation from chapter 4 are implemented in chapter 5 to evaluate surface sensitivity and SPR characteristics of various nanohole arrays. The interaction of surface plasmons supported on a nanohole array and a single nanoparticle affixed to an atomic force microscopy (AFM) probe is studied in chapter 6 for application in optimizing gap mode enhancement of the plasmonic field. Lastly, the overarching conclusions, brief summary, and future directions are presented in chapter 7.

Chapter 2

NANOHOLE ARRAY SP FEATURES IN VARIOUS OPTICAL CONFIGURATIONS

2.1 Introduction

The plasmonic properties of nanohole arrays are exploited in many fields and applications with continued growth in research activity and number of publications since the discovery of their surface plasmon activity by Ebbesen in 1998 [126] (Figure 2.1). Applications have widely expanded from Ebbesen's original proposed use of nanohole arrays for near-field scanning optical microscopy and sub-wavelength photolithography[126]. The vast areas of research include surface-enhanced spectroscopy (Raman, fluorescence, infrared)[127, 128][129, 130, 131][132], optics (polarization control, filtering, switching, nonlinear optics, waveguiding) [13, 14][15][16][15][17, 18], optoelectronics[133, 134], and surface plasmon resonance sensing[135, 136, 133]. In particular, this dissertation explores the SPR sensing capability of nanohole arrays, but the fundamental characterization of the SP features may provide insight to other applications as well.

SPR sensing with plasmonic nanohole arrays has demonstrated increased biosensing capability over conventional continuous gold[55, 54] and has been investigated for numerous analytes and optical configurations[133, 70, 6]. The majority of the studies utilize transmission mode spectroscopy to measure the SPR signal and have attained similar sensitivity as thin film SPR.[102, 103] However, measurements of nanohole arrays in Kretschmann configuration exhibit comparatively greater sensitivity. A 20-fold increase in sensitivity to Immunoglobulin G and 7-fold increase for bulk refractive index change was observed by Couture et. al.[55] for measurements in Kretschmann configuration compared to transmission mode. This chapter presents the various SP modes

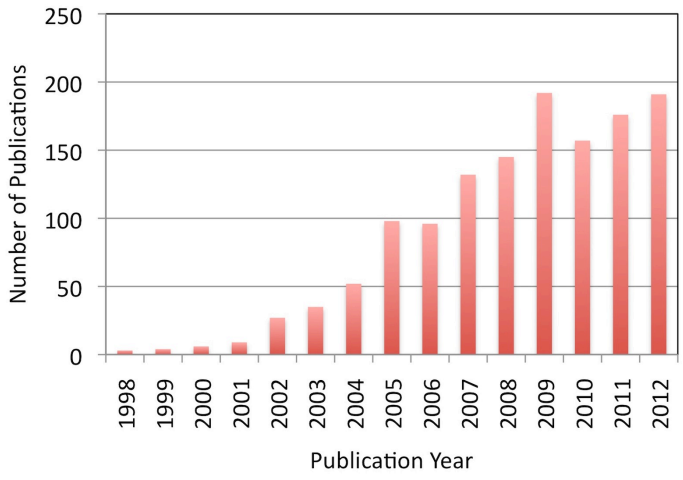

Figure 2.1: Number of publications on plasmonic hole arrays listed by year. Data retrieved from Web of Knowledge[137]

.

supported on nanohole arrays that are excited in different optical configurations. Understanding the plasmonic modes allows for manipulation and selection of parameters for a given application.

In addition to the excitation mode, the SPR wavelength and structural parameters of the nanohole arrays affect the sensitivity as well. Extending SPR wavelength into the near infrared (NIR) in Kretschmann configuration offers potential for greater sensitivity than in the visible wavelength region [45, 125], and investigation in a novel wavelength region (the NIR) for exciting Bragg SPs in Kretschmann configuration. SPR on nanohole array substrates in Kretschmann configuration has been researched in the visible wavelength region (refer to [138, 139, 55]), but has not been measured in the NIR to our knowledge. Furthermore, the Bragg SPR wavelength depends on the diameter and periodicity of the nanohole arrays [140, 141]. The physical parameters of the nanohole arrays are easily controlled by the nanosphere lithography fabrication technique (discussed below). This technique is easily implemented, requires little resources, and produces highly reproducible features. Contrastingly, the colloidal

techniques used for fabrication of most other free standing nanostructures lacks reproducibility, and fabrication by focused ion beam or electron beam lithography requires advanced instrumentation and long fabrication times.

2.2 Nanohole array surface plasmon resonance modes

Nanohole arrays support various SP modes (Figure 2.2). Localized surface plasmons arising from Mie type scattering may be excited within the nanohole [142] and propagating plasmons similar to continuous gold (equation (1.3)) may be excited in the strips of gold between the rows [139]. Additionally, shorter range plasmons in the regions between neighboring holes are excited by incident light that is diffracted into the sample plane according to the Bragg resonance order of the reciprocal space lattic, thereby they are called Bragg SPs. In this case, the momentum matching model includes additional terms to equation (1.1) for the reciprocal lattice vectors (G_x and G_y); [69, 140]

$$k_{sp} = k_x + iG_x + jG_y \tag{2.1}$$

where (i,j) represents the Bragg resonance order. For a hexagonal array, the lattice vectors may be represented in terms of the nanohole array periodicity (P), $G_x = G_y = 4\pi/(\sqrt{3}P)$ [6], so that by equations (2.1) and (1.3) the SPR wavelength ($\lambda_{SPR}(i,j)$) is determined by;[140]

$$\lambda_{SPR}(i,j) = \frac{P}{\sqrt{\frac{4}{3}(i^2+ij+j^2)}}\left[\sqrt{\frac{\epsilon_s\epsilon_m}{\epsilon_s+\epsilon_m}} - \eta_{inc}\sin\theta_{inc}\right] \tag{2.2}$$

LSPs arise from scattering within the individual nanoholes, however they are affected by other SP modes and LSP of surrounding holes when separation distances are on the order of the wavelength of light. Comparatively, a single isolated nanohole does not exhibit the grating type dispersion, but does support a LSP and may be treated as a magnetic dipole. Traditional Bethe-Bouwkamp theory predicts almost no zero order transmission through a single subwavelength hole; however, there is

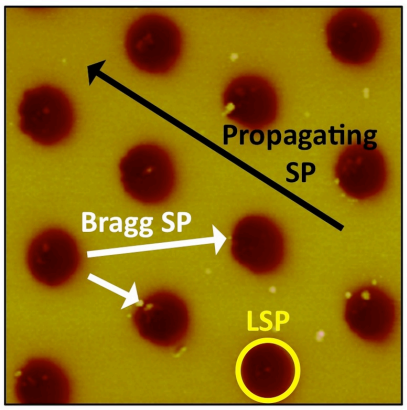

Figure 2.2: Diagram of nanohole array SP modes.

apparent extinction arising from LSPs at the edges of and along the depth of the hole.[15, 143, 144] Detection of the near field intensity of a single nanohole demonstrates the hole acting as a SPP point source with interference fringes arising from interference of SPs with transmitted light.[145] The LSP of a single hole[146] or a nanohole chain [142] may be used for sensing, similar to other LSPR sensors, though the Bragg SPs and propagating plasmons cause enhanced transmission effects at specific wavelengths (discussed in section2.5) and are better suited to sensing applications.

SP modes may be coexcited within the same nanohole array structure, which further increases the electromagnetic field intensity and SPR response. Similar wavelength excitation of various SP modes, within a 100 nm window, may facilitate coupling between the SPs and an increase in field intensity. An increase in SPR spectroscopy sensitivity has been observed for nanohole arrays [100] when the propagating λ_{SPR} was 100 nm redshifted from the Bragg λ_{SPR}.[100] This effect has also been observed for ordered arrays of buried nanovoids where coupling between localized and propagating modes was tuned by structure parameters and angle of incidence.[115, 147] Studies of surface enhanced Raman spectroscopy (SERS) has further supported this notion by demonstrating an increase in field and SERS intensity when Bragg SPs and LSPs or different order Bragg SPs occur at similar wavelengths.[122] The interplay of SP modes also creates "hotspots" or regions of greatest field intensity across the nanohole

array surface. Hotspots are a well known phenomenon exploited in SERS for targeted analyte placement and maximal response. The hotspots on nanohole arrays has been imaged by SERS[128] and may also be considered to maximize signal by directing analyte binding to these hotspots and in effect reduce detection limits.[148, 149] Nanohole arrays with D/P= 0.63-0.54 exhibit greatest field intensity at the rim of hole, whereas for D/P<0.5, the greatest intensity occurs within the hole.

It should be noted that, in addition to SPR, other optical phenomena of the nanohole arrays are evident in different spectroscopic configurations. In particular, Wood's anomalies may occur, which overlap and interact with the other optical features.[150, 144, 66] Wood's anomalies arise from light which is diffracted into the nanohole array plane and is redistributed into allowed orders. The diffraction wavevector, $k_{diffraction}$, may be represented by;

$$k_{diffraction} = 2\pi\sqrt{\epsilon_d}/\lambda \tag{2.3}$$

where ϵ_d is the complex permittivity of the dielectric through which the light passes (air, prism, etc...). By equations (2.1) and (2.3) the wavelength position for Wood's anomalies (λ_{WA}) may be determined by;

$$\lambda_{WA}(i,j) = \frac{P\sqrt{\epsilon_d}}{\sqrt{\frac{4}{3}(i^2+ij+j^2)}} \tag{2.4}$$

Different optical configurations may access and utilize different plasmonic modes (Figure 2.3). Long- and short- range propagating plasmons cannot be excited by directly incident light, rather momentum matching must be achieved by coupling via prism or grating. A prism may be used to excite propagating plasmons, and diffraction from the nanoholes themselves may excite Bragg SPs. Thereby, Bragg SPs may be excited in all configurations, however additional optical components, such as the prism used in Kretschmann configuration, are necessary to reach the momentum to excite propagating plasmons similar to continuous gold. Contrastingly, localized surface plasmons are radiative modes which may be excited directly. Traditionally they are excited

in transmission mode and perceived as an overlying feature in the spectra.[144] Spectrally, the lower order Bragg SPs and propagating plasmons may be sensitive to sample refractive index (RI) and used for sensing purposes. All of the SP modes increase field intensity and may be utilized for field enhanced techniques.[66, 151, 44]

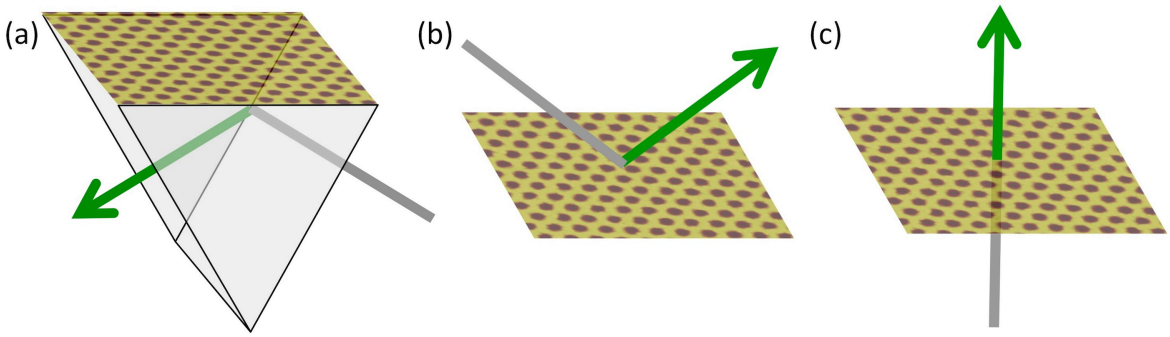

Figure 2.3: Different SPR optical configurations including (a) Kretschmann configuration (b) reflection and (c) transmission modes.

Accordingly, different SPR spectroscopy configuration may be selected for different applications. Selective considerations for a given sensing application include propagation length, sensitivity to changes in the particular sample, physical limitations of optical setups, and SPR wavelength tunability. LSPs and Bragg SPs are confined to within the holes and within the regions between the holes, respectively, whereas the propagating plasmons freely propagate for distances similar to that on continuous gold (tens of microns, depending on excitation wavelength).[138] This affects SPR imaging capability as well as sample interaction area. Regarding SPR sensitivity, measurements in Kretschmann configuration have shown a 20-fold increase as compared to transmission mode.[55] Additionally Kretschmann configuration allows for real-time measurement in biological fluids which are highly scattering. Yet, despite reduced sensitivity, several immunosensors have been developed based on transmission through nanohole or nanotriangle arrays [152, 149, 153, 136], but few have investigated Kretschmann configuration.[54, 55] This may be due to simplicity of optical setup; however, the

addition of a prism is straightforward, requires little space, and may transition to commercial use easily as there are many commercially available bench top and portable SPR systems[6]. However, transmission mode has application in flow through analysis where analyte binding efficiency is increased and sensitivity may be increased by 6× compared to flow over techniques.[149]

2.3 Nanohole array fabrication by nanosphere lithography

Nanohole arrays of different nanohole diameter, periodicity, and height are fabricated by a nanosphere lithography technique [154, 155, 156] in which a mask of hexagonally close packed polystyrene nanospheres is sputter coated and removed, leaving behind a nanohole array patterned gold film. The nanohole arrays are formed on glass cover slips that are cleaned by immersion in boiling piranha solution (3:1 (v/v) concentrated H_2SO_4: 30% H_2O_2 (Fisher Scientific, Fair Lawn, NJ) *Caution: Piranha solution is strongly oxidizing and should be handled with great care*) for at least one hour, then triple rinsed and sonicated with deionized water and actively dried with nitrogen gas stream (Keen Compressed Gas Co., Wilmington, DE). Nanosphere templates are formed by allowing entropy driven packing to occur within a monolayer of spheres (Figure 2.4(a)). This is achieved by one of two methods; scoop or dropcast. For the smaller nanospheres, the scoop method was implemented, in which an aliquot of nanosphere solution is dispensed onto a dry slide and the slide is floated atop a water meniscus formed within a petri dish. A drop of 2% w/w sodium dodecyl sulfate (85%, Acros Organics, New Jersey) solution is dispensed onto the water to perturb the nanospheres and initiate ordered packing. A wet, clean slide is used to scoop a layer of the nanospheres with a minimal underlying water layer. The slide is allowed to slowly air dry on a level microscope slide, covered with a petri dish that is propped up slightly with another microscope slide. The dropcast method involves direct dropcasting of solution onto a dry slide and slow drying on this surface. As the solution evaporates, the nanospheres pack within the confined, diminishing water meniscus, until they reach close packing. Table 2.1 outlines the amount of solution dropcast onto the dry slide

and the amount of ethanol and water added to the provided nanosphere solution (10% w/w, 490 nm and 600 nm spheres from ThermoScientific, Fremont, CA and 450, 820, 1500, and 3000 nm spheres from Duke Scientific, Palo Alto, CA).

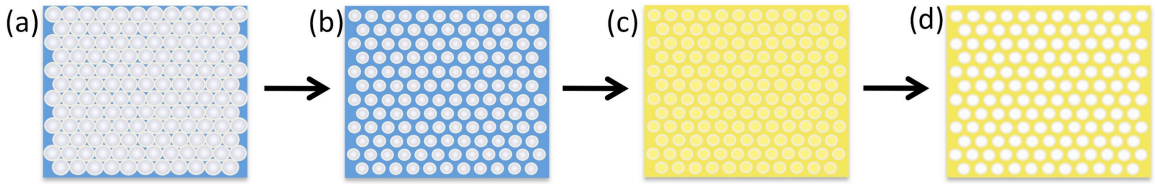

Figure 2.4: Schematic of nanohole array fabrication by nanosphere lithography; (a) nanosphere mask formation (b) reactive ion etching of nanospheres to reduce diameter (c) sputter coating nanosphere mask with gold and (d) removal of nanosphere mask.

The nanospheres are then reactive ion etched by oxygen plasma (Figure 2.4(b)) in a plasma etcher (Harrick Plasma, Ithaca, NY). The nanospheres maintain their order, but the diameter size reduces, thus the periodicity is fixed by the initial nanosphere diameter. After etching, the slide is coated in a DC magnetron sputterer (Cressington Scientific Instruments Ltd., model 308R, Watford, UK) with 3 nm chromium (99.95^{+}%, Kurt J. Lesker Co., Clairton, PA) and variable thickness gold (99.99%, ESPI Metals, Ashland, OR) layer (Figure 2.4(c)). Generally, 60-80 nm was chosen for gold thickness and controlled within 2 nm variation. The masks are placed on a raised stage close to the specific metal target in order to increase sputtering efficiency and directionality of sputtered material plasma. This accounts for the inherent divergence in the plasma plume with distance from the target and minimizes creep under the nanosphere. The sputtering time changes as a function of the nanosphere template. Larger diameter:periodicity ratio minimizes the space between spheres and minimizes efficiency of sputtered material depositing within the confined space, so the sputtering time required for a given thickness is calibrated by AFM for particular templates. After sputtering, the nanospheres are removed by sonication in ethanol or chloroform for 10 min (Figure 2.4(d)), leaving a thin gold film with nanohole array perforations. The sample is washed with ethanol and dried with dry nitrogen.

Table 2.1: Procedural details for nanosphere lithography template formation.

Periodicity (nm)	Method	Water:Ethanol:Nanosphere Solution	Volume Solution (μL)
450	Scoop	0:1:1	13
490	Scoop	0:1:1	13
600	Scoop	0:1:1	13
820	Dropcast	10:3:3	25
1500	Dropcast	4:3:2	25
3000	Dropcast	4:3:2	25

The method choice (scoop or dropcast) and solution ratios were optimized to achieve the largest continuous nanohole array area and the resulting procedure is presented in table 2.1. The oxygen etch pressure and time were investigated as well. An oxygen pressure of 20-40 mTorr within the etching chamber effectively etched the nanospheres, whereas higher pressures extinguished the plasma, and lower pressures were inefficient. Additionally, the extent of etching depends on the time and position within the etcher. For example, for nanospheres with diameters of 490-3000 nm, the necessary etching time ranged from 8-75 min for etching to a <0.3 diameter:periodicity. The appropriate etching time and final analysis of particular diameters was validated by atomic force microscopy (AFM) of nanohole arrays fabricated at ranging etching time. The etching time relationship to diameter reduction is nonlinear and varies somewhat with ambient pressure, so AFM was necessary to confirm the dimensions of each nanohole array set. Furthermore, a long initial etching phase occurs where the portions of the nanosphere in free space are etched more rapidly than the portions touching adjacent nanospheres. In this case, a bridge of material is formed between adjacent nanospheres as demonstrated in figure 2.5. After the bridge is broken, material is rapidly removed, and the diameter quickly reduces. The protrusions from bridging round so that the resulting nanospheres are spherical, as evidenced by AFM images (e.g. Figure 2.2 and Figure 5.2). Therefore, sets of particular periodicity and diameter were etched in batches where samples were positioned within the same 2 in^2 area within

the plasma etcher and etched for the same amount of time.

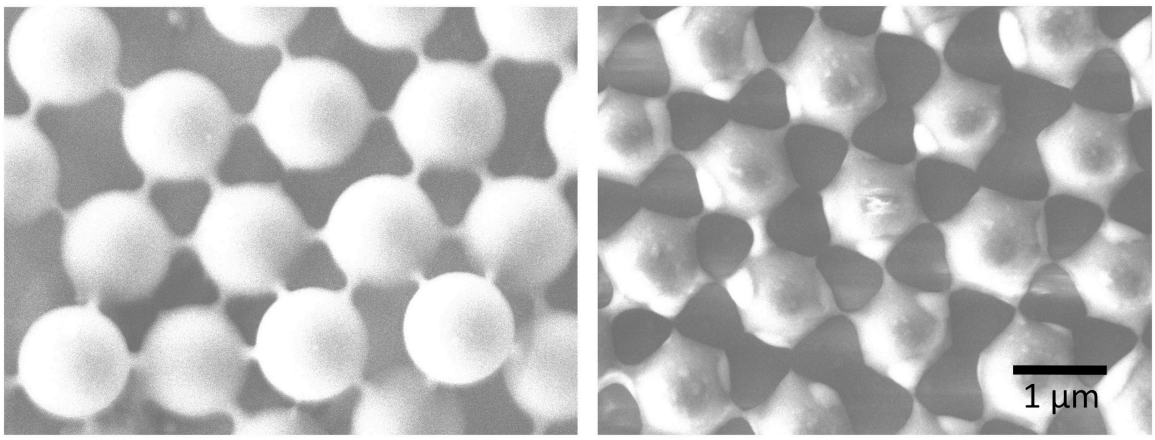

Figure 2.5: SEM images of polystyrene bridges formed between nanospheres due to anisotropic reactive ion etching.

This batch method produces highly reproducible nanohole structures. An average variation in diameter of 9% was achieved ($n > 8$). The periodicity was fixed by the nanosphere diameter, which falls within a distribution as reported by the supplier in terms of relative standard deviation (RSD); 490 nm ± <3%, 600 nm ± 1.7%, 820 nm ± <3%, 1500 nm ± 4%, 3000 nm ± <5%. This affects the periodicity variation, and efficient packing could be disrupted if the RSD were too large. The presented procedure culminated in ordered arrays over large areas on the scale of millimeters. Within the ordered area there are defects such as grain boundaries/dislocations and missing holes. The dislocation free area for given nanohole arrays is presented in table 2.2.

2.4 Kretschmann configuration SPR

SPR by Kretschmann configuration is achieved by coupling light through a prism to the backside of the nanohole array (Figures 2.3(a) and 2.6). The nanohole array is coupled to the prism by refractive index matching liquid. SPR at the nanohole array-sample interface is measured as an absorption in the reflected spectrum. In

Table 2.2: Size of single orientation area of different periodicity nanohole arrays and number of nanoholes in continuous line. The area provided refers to average area within grain boundaries.

Periodicity (nm)	Area (μm^2)	No. Holes in Line
490	5-10	10-20
600	20-40	33-63
820	20-40	24-49
1500	20-40	13-27
3000	10-30	3-10

the following instances, the incident angle is held constant, so that the excitation wavelength (λ_{SPR}) is measured.

Different λ_{SPR} regimes may be accessed depending on the angle of incidence, broadband source, detector, and optical materials used. The common wavelength interrogation range is within the visible region and excites the propagating SPs between 600-700 nm. This involves incident angles above 70° for excitation of the propagating plasmon through a BK-7 prism. An optical setup was built to investigate nanohole arrays in the visible wavelength regime (Figure 2.6). The use of a dove prism simplifies the setup by facilitating a collinear optical train.[157] As such, the collection optics were in line with the source optics, and the angle of incidence was set by the prism geometry (72.8°). A W-halogen light source (Oriel Instruments, Stratford, CT) was pseudo-collimated by an SMA collimator attachment. The light passed through a linear polarizer (25 mm ϕ, Edmund Optics, Barrington, NJ) and the angle spread and spot size were constricted by a 1 mm aperture. The light was incident on a sample coupled to a BK7 dove prism. The light was collected through an SMA collimator lens and passed to an Andor SR303i spectrometer with 150 l/mm grating (South Windsor, CT) for detection. Periodicities of 450 nm and 820 nm were investigated with this setup. Representative spectra in various refractive index media are presented in figure 2.7. The propagating plasmon is not observed in air, but is excited at $\approx$ 620 nm in water and $\approx$ 680 nm in ethanol. The feature at $\approx$ 820 nm is fairly insensitive to

sample refractive index, appearing at a consistent wavelength regardless of dielectric medium. This feature arises from a combination of Bragg SPs and may be removed by subtracting the air spectrum from the other spectra in order to analyze the propagating SP sensitivity.[139]

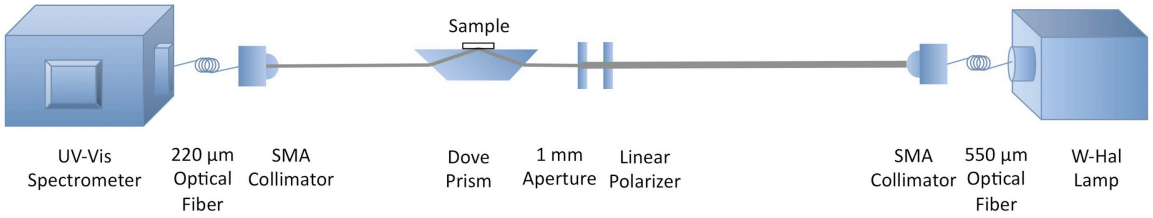

Figure 2.6: Optical setup for Kretschmann configuration SPR in the visible region.

SPR spectroscopy in the near infrared (NIR) is enabled by an accessory which fits into a commercial FTIR spectrometer. The accessory directs a constricted portion of the light from the FTIR spectrometer source to a prism coupled to the SPR substrate and back into the FTIR spectrometer for detection. The first generation accessory is a modification to a variable angle reflectance accessory, the Autoseagull (Harrick Scientific, Pleasantville, NY) which is explained in detail in the publication entitled "Characterization of a Variable Angle Reflection Fourier Transform Infrared Accessory Modified for Surface Plasmon Resonance Spectroscopy"[48] and pictured in figure 2.13(b). The modified Autoseagull accessory has automatic angle change capabilities, however the stability and platform flexibility could be improved. Therefore, a second generation NIR-SPR accessory, the "v2 accessory", was developed from the ground up. Chapter 3 details the development and characterization of the v2 accessory. The NIR-SPR spectra of various nanohole arrays was collected on the v2 accessory and is presented in great detail in chapter 5. Briefly, in addition to the propagating plasmon, there are numerous Bragg SPs excited which depend on the periodicity. The Bragg SPs exhibit poor sensitivity, whereas the propagating plasmon is highly sensitive and may be used for sensing.

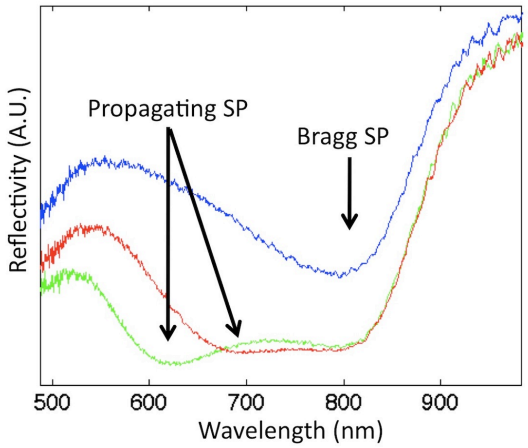

Figure 2.7: Representative SPR spectra in visible Kretschmann configuration for air (—), water (—), and ethanol (—).

The NIR-SPR setup may be used for mid-infrared SPR spectroscopy by exchanging the lenses and prism material to components with optical transparency in the infrared. ZnSe lenses (Thorlabs, Newton, NJ) and CaF_2 prism (Thorlabs, Newton, NJ) can be used for interrogation of $0.8 - 8\mu$m. In this case, the prism geometry was an equilateral triangle, rather than a dovetail trapezoid, so that a wider range of applicable angles may be accessed. Nanohole arrays of ranging periodicity (490, 820, 1500 and 3200 nm) were fabricated on CaF_2 slides (Crystaltechno, Ltd., Moscow) and their MIR-SPR spectra were acquired. The MIR-SPR spectra from 7000-3500 cm^{-1} (1.4-2.9 μm) did not exhibit apparent Bragg SPs and there was significant noise interference around 4000 cm^{-1}.

2.5 Transmission mode SPR

Nanohole array Bragg SPs and LSPs may be excited in transmission mode (Figure 2.3(c)) and extraordinary optical transmission (EOT) due to SPR has been widely studied since its discovery by Ebbesen et. al.[126] EOT is a phenomenon where a greater amount of light is transmitted through the nanohole array than is geometrically

passable through the open hole area. EOT arises from coupling of Bragg SPs and LSPs launched from the holes on the front and back-sides of the nanohole array and subsequent reradiation.[126, 158, 15]

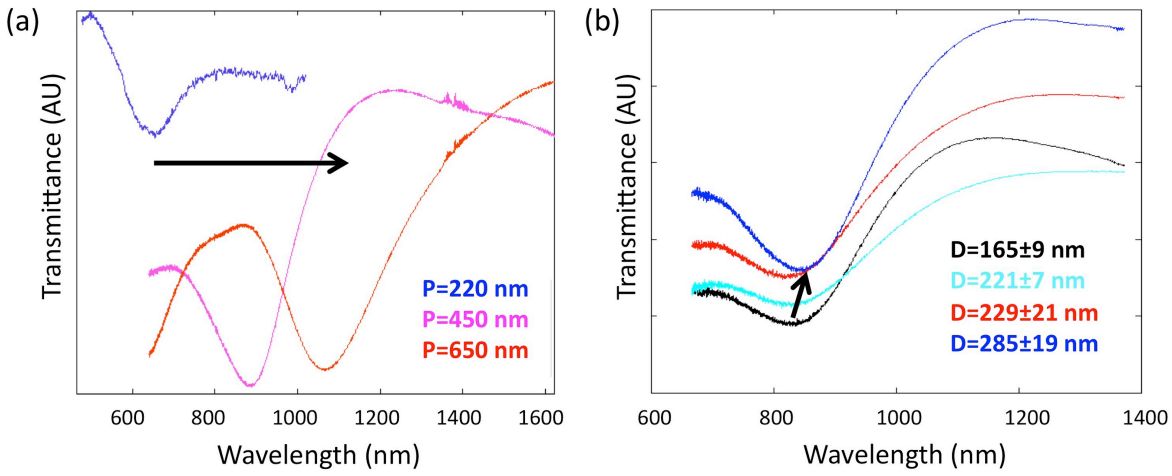

Figure 2.8: Transmission spectra for various (a) periodicity (constant D/P = 0.6±0.07) and (b) diameter (constant P=450 nm) nanohole arrays.

The transmission spectra are a complex combination of LSPR, Bragg SPs, and Wood's anomalies. Bragg SPs (equation (2.2)) arise from different resonance orders (e.g. (1,0), (1,1)) and both sides of the nanohole array (glass or air).[159, 133] The light which couples to Bragg SPs may be coupled to the other side and reradiated such that it is measured as a peak in transmission (EOT). LSPR within the holes manifests as a broad peak that overlays the spectrum.[66, 150] The feature may overlap with the Bragg SPs and cause broadening or double peaks, however it is only apparent when the wavelength of LSP and Bragg SP excitation are similar.[160] A band of light centered at approximately 490 nm is transmitted through optically thin to near optically thick gold layers and is apparent in spectra in this wavelength region.[150] Wood's anomalies transfer light into certain wavelengths governed by equation (2.4), which may interfere with the Bragg SPs and form Fano type resonances in transmission intensity.[150, 161, 162] In effect, the spectra are complex with various maxima and minima (Fano-like

resonances). For sensing purposes, an RI sensitive spectral feature should be selected. Generally, the minima between the (1,0) peaks arising from the sample and glass interface is selected[138, 133, 159], and its λ_{SPR} and sensitivity depends on diameter and periodicity of the nanohole arrays.[140, 139]

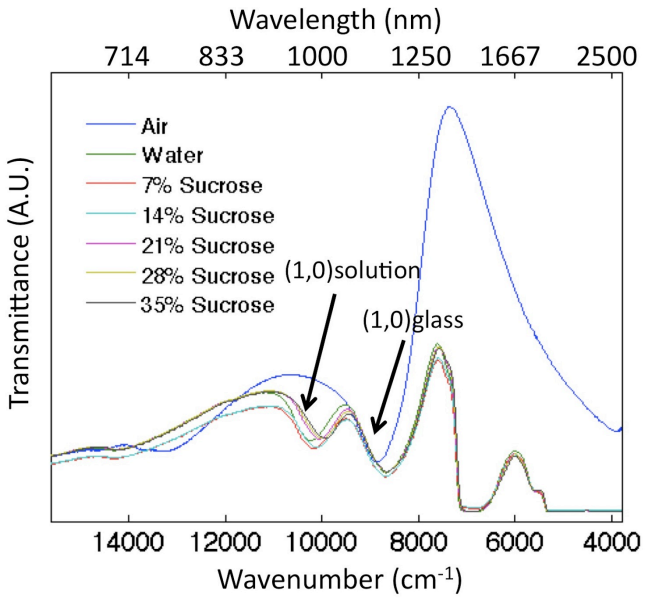

Figure 2.9: Transmission spectra of nanohole array (P=820 nm, D=224±13 nm) in air and sucrose solutions. Water absorption features apparent at $< 6800\mathrm{cm}^{-1}$

.

An optical setup was configured to collect and analyze transmission spectra of various nanohole arrays. The setup for transmission spectroscopy in the visible range is parallel to figure 2.6 with the prism removed and the sample positioned perpendicular to the optical axis ($\theta_{inc} = 90°$). A Bruker Optics (Billerica, MA) Hyperion FTIR microscope was used for transmission spectroscopy in the infrared. The condenser in the bottom of the microscope was removed, so the light was collimated and transmitted perpendicularly through the sample. The transmission spectra of nanohole arrays in air was investigated as a function of diameter size (constant P=450 nm) and periodicity (constant $\mathrm{D/P} = 0.6 \pm 0.07$). The SPR features likely correspond to the $(1,0)_{\mathrm{glass}}$ Bragg SP with the $(1,0)_{\mathrm{air}}$ Bragg SP below the measured range. A red shift in λ_{SPR}

(minimum of the transmission dip) with increasing periodicity and D/P is apparent in figure 2.8. Thereby, the λ_{SPR} is easily tuned by nanohole array parameters.

The sensitivity of a nanohole array with P=820 nm, D=224±13 nm was assessed by measurement in air and a set of sucrose solutions with ranging refractive index, $1.333 - 1.390$ RIU (Figure 2.9). The spectra exhibit a SP feature at 1000 nm when in solution. This can likely be identified as a dip between the $(1,0)_{sample}$ and $(1,0)_{glass}$ Bragg SPs according to modeling performed by [138, 133, 159] and its sensitivity to sample RI. A calibration curve for $\Delta\lambda_{SPR}$ of the $(1,0)_{sample}$ peak vs. RI determines the transmission mode sensitivity for this nanohole array; 490±18 nm/RIU (-4900±180 cm^{-1}/RIU). This is in agreement with similar studies in literature.[55, 138, 136]

2.6 Reflection mode SPR

SPR spectroscopy in reflection mode (Figure 2.3(b)) is performed with the Autoseagull NIR-SPR setup [48] with the prism removed (refer to figure 2.13(b)). In this manner, the light is directly incident on the nanohole array, and the reflected light is detected by the FTIR spectrometer. Bragg SPs may be excited in this setup and are offset from Kretschmann configuration by the wavevector differences due to prism coupling (approximately 300 nm blue shifted from Kretschmann configuration at $\theta_{inc} = 65°$). The RI environment is similar to that in Kretschmann configuration (glass-gold-sample) as the nanohole array is fabricated atop a cover slip and air interfaces the opposing side; however, the light is directly reflected from the nanohole array-sample interface. Thereby, η_{inc} corresponds to air rather than glass and the λ_{SPR} is offset from λ_{SPR} observed in Kretschmann configuration accordingly (equations 1.2 and 2.2). Reflectance spectra for 820 nm periodicity nanohole arrays at $\theta_{SPR} = 65°$ exhibit peaks at 9500-9200, 7100, and 5600 cm^{-1} (1050-1090, 1410, and 1790nm), refer to figure 2.10. The potential for artifacts from possible residual polystyrene remaining within the nanoholes is nullified, because polystyrene exhibits broad NIR absorption peaks at 8500 and 6300 cm^{-1}.

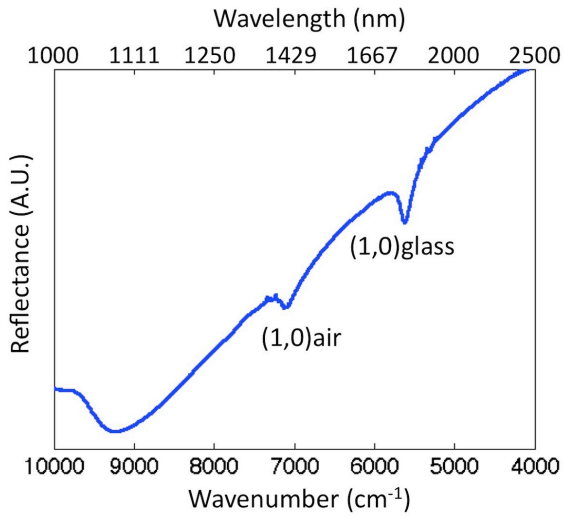

Figure 2.10: Representative reflectance spectra of nanohole array with P=820 nm.

2.7 Short range plasmons with azimuthal angle

The Bragg SPs depend on the polarization of the incident light vector relative to the nanohole array lattice axis.[163, 147] The relative orientation is characterized by the azimuthal angle (ϕ) between the linearly polarized incident light vector and x-axis of the nanohole array reciprocal lattice, as pictured in figure 2.11. By controlling the azimuthal angle, the short range plasmon wavelength may be tuned.[163, 147] Recently, a model for Bragg SPs has been developed by Masson et. al. [164] which considers azimuthal rotation. The model involves an additional factor for azimuthal rotation, R, in equation (2.2);

$$\lambda_{\mathrm{SPR}}(i,j) = \frac{\mathrm{P}}{\sqrt{\frac{4}{3}(i^2+ij+j^2)}}\left[\sqrt{\frac{\epsilon_s\epsilon_m}{\epsilon_s+\epsilon_m}} - \eta_{\mathrm{inc}}\sin\theta_{\mathrm{inc}}R\right] \tag{2.5}$$

Where,

$$R = i\cos\phi + j\cos(\phi+60) + i\sin\phi + j\sin(\phi+60) \tag{2.6}$$

The theoretical Bragg SP λ_{SPR} changes with nanohole array periodicity and ϕ (Figure 2.12). For a given periodicity nanohole array, there is a repetition of the

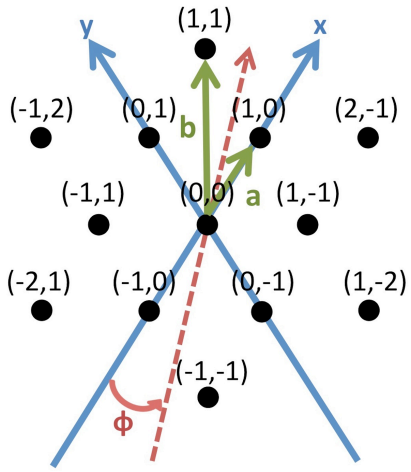

Figure 2.11: Azimuthal angle (ϕ) and different Bragg resonance orders (x,y) displayed with respect to nanohole array reciprocal lattice. a and b represent the two different vector lengths from (0,0) included in the diagram.

Bragg SPs λ_{SPR} every $\Delta\phi = 60°$ arising from radially symmetric Bragg lattice orders correlating to (a) the (1,0) distance from the origin or (b) the (1,1) distance from the origin. Furthermore, the Bragg SP λ_{SPR} are reflected every $\phi = 30°$, so analysis of the features within the first 30° represents the possible Bragg SP λ_{SPR}'s for the low Bragg resonance orders illustrated in figure 2.11. At any given ϕ within this 30° range, the specific Bragg SPs may be assessed. The Bragg SP λ_{SPR}'s may overlap in some instances, and degeneracy of Bragg SP λ_{SPR} is observed. Changing periodicity causes a red shifting of Bragg SP λ_{SPR} and larger $\Delta\lambda_{SPR}$ with ϕ; therefore, Bragg SP λ_{SPR} may be tuned with periodicity and ϕ. (More detailed discussion and Bragg resonance order designation in experimental spectra is presented in section 5.4.)

The Bragg SPs may be controlled in a highly ordered sample with consistent azimuthal angle throughout the interrogated region. Modeling by equation (2.5) for variable azimuthal angle ($\phi = 0 - 30°$) demonstrates a tunable $\Delta\lambda_{SPR}$ range of 129 nm for the Bragg SP arising from (-1,0) resonance order at both the glass ($\lambda_{SPR} = 1909 - 2038$ nm) and air ($\lambda_{SPR} = 1549 - 1678$ nm) interfaces ($\theta_{inc} = 65°$ and $P = 820$ nm in Kretschmann configuration). Similarly, when P=490 nm, a tunable range of $\Delta\lambda_{SPR} =$ 77 nm for the Bragg SP arising from the (-1,0) resonance order at both glass ($\lambda_{SPR} =$

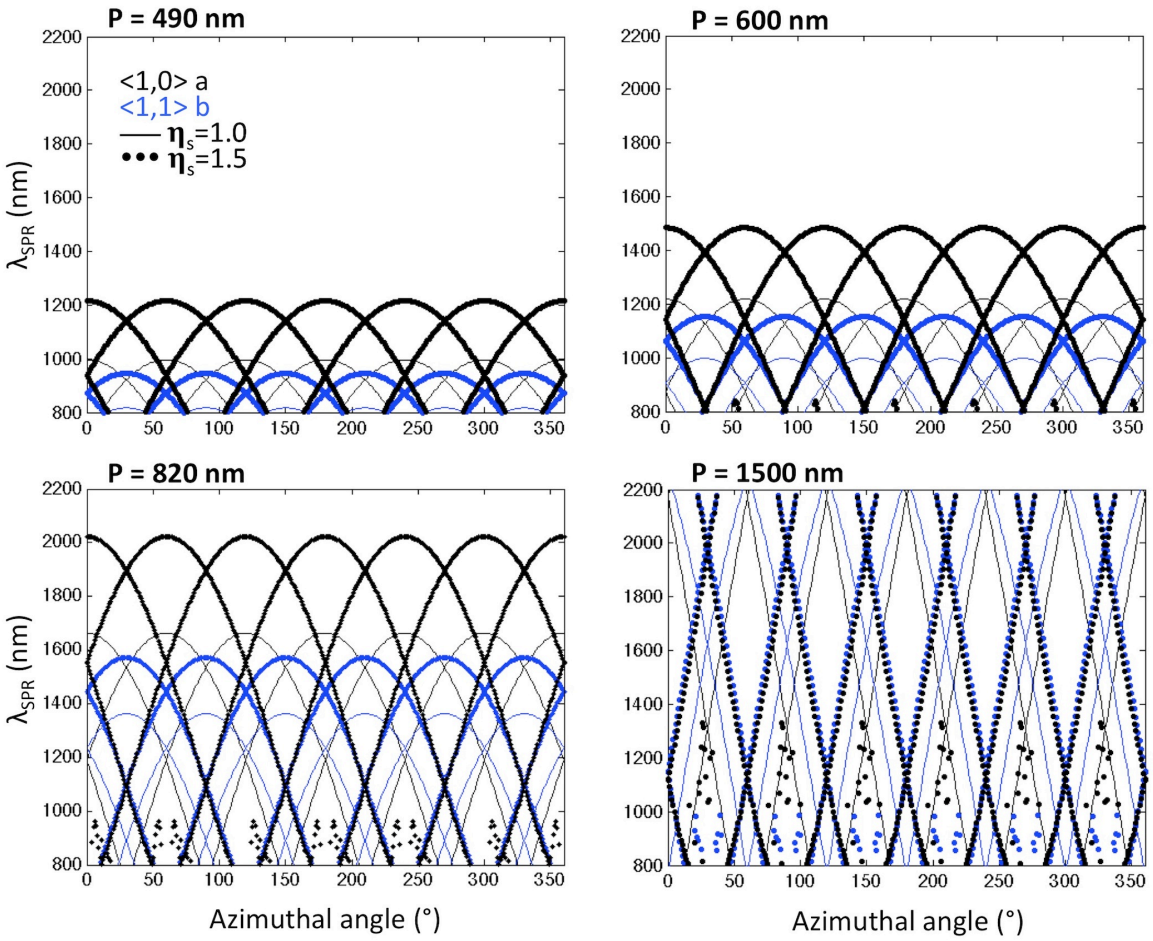

Figure 2.12: Theoretical Bragg SP λ_{SPR} as a function of azimuthal angle, ϕ, for various periodicity nanohole arrays. The Bragg SPs supported on both the glass ($\eta_g = 1.5$) and the sample side ($\eta_s = 1.0$ for air) were modeled with $\theta_{\mathrm{inc}} = 65°$. There are some points which do not follow the curve and may be disregarded. They result from instances where the wavelength drops below the range of the model (700-2300 nm) and erroneous λ_{SPR} are calculated in return.

1148 − 1225 nm) and air (λ_{SPR} = 929 − 1006 nm) interfaces is predicted. Change in ϕ inducing a shift in SPR wavelength for nanostructure arrays has been observed previously.[147, 165] The range in SPR wavelength with changing azimuthal angle could be utilized for applications in coupling to specific nanostructures or switching on and off high coupling or SPR active regimes.

In order to adjust the azimuthal angle in practice, a rotational prism-SPR substrate holder was developed which also has XY positioning (Figure 2.13). There is a flow cell interfacing to the bottom of the prism, so that solution exchange is facilitated at the SPR substrate interface. Rotation is controlled within 2° and the sample position may be adjusted with the XY positioning screws.

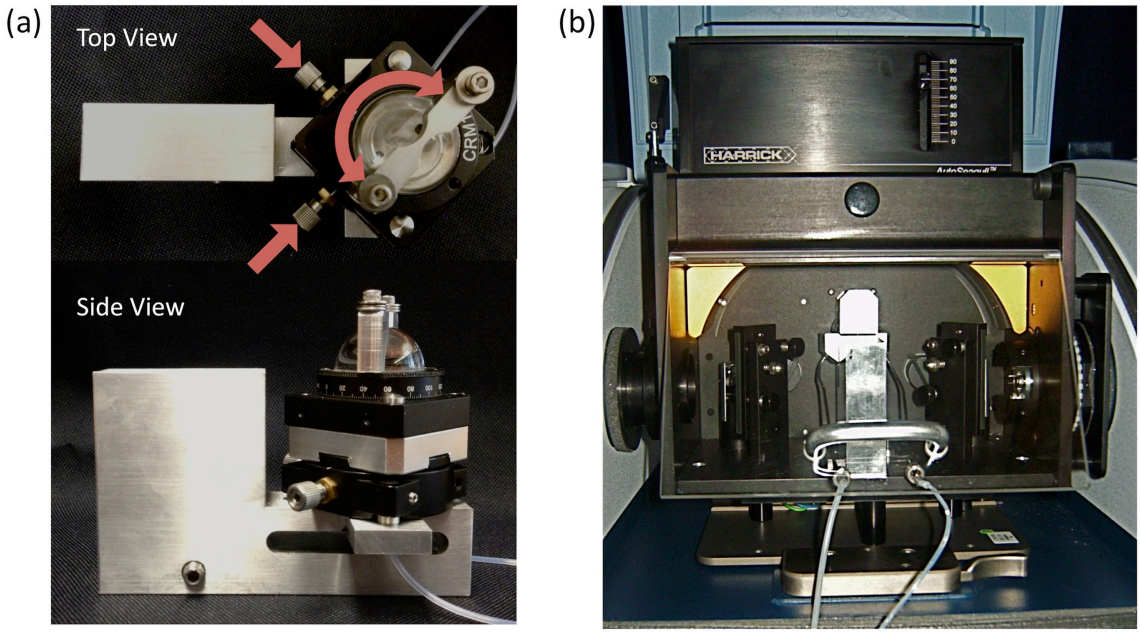

Figure 2.13: (a) Rotational prism-SPR substrate holder for changing azimuthal angle within the Autoseagull NIR-SPR accessory. (b) Photograph of Autoseagull NIR-SPR accessory in FTIR spectrometer sample compartment.

This setup was implemented with the prism removed to collect reflection spectra at various azimuthal angle ($\phi = 0-30°$, in increments of 5°). Measurements of nanohole arrays with P = 820 nm were acquired at $\theta_{inc} = 65°$ (Figure 2.14). A change in λ_{SPR}

of 14 ± 3 nm and 11 ± 5 nm was measured for the (-1,0) Bragg SP at the glass and air interfaces, respectively. Theoretically, $\Delta\lambda_{SPR} = 86$ nm for the Bragg SP arising from the (-1,0) resonance order at both the glass ($\lambda_{SPR} = 1626 - 1719$ nm) and air ($\lambda_{SPR} = 1260 - 1360$ nm) interfaces is predicted. The difference between predicted and measured $\Delta\lambda_{SPR}$ is most likely due to inhomogeneous orientation in fabricated nanohole arrays (no dislocations for 20-40 μm) over the interrogated area (approximately 1 mm) and broadening of the peaks.

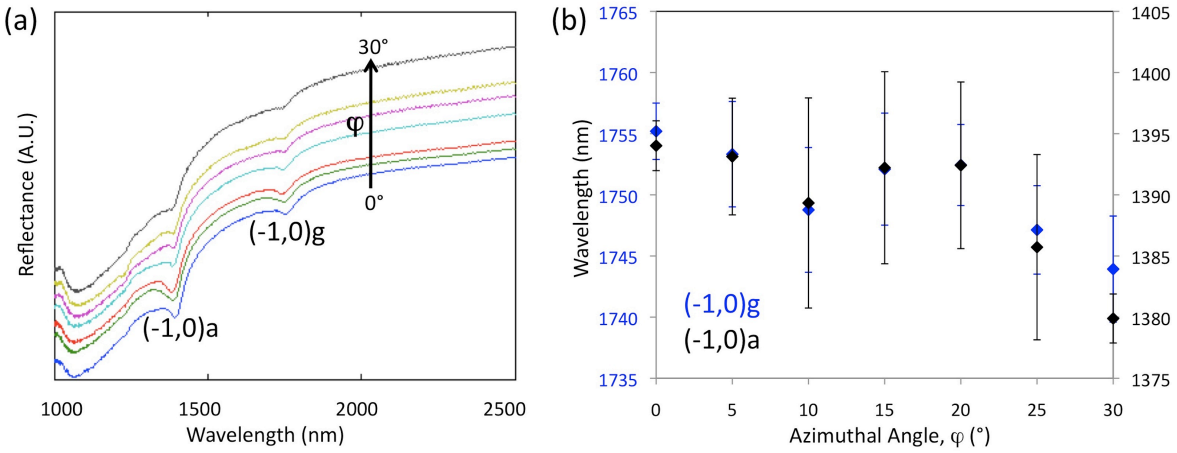

Figure 2.14: Experimental (a) reflection spectra of nanohole array (P=820 nm) and (b) respective λ_{SPR} at azimuthal angle=0-30°at glass (g) and air (a) interfaces.

2.8 Conclusion

The SPs on nanohole array substrates are excited in several optical modes and should be selected according to application. The Bragg SPs are excited in each spectroscopic mode investigated, including transmission, reflection, and Kretschmann configuration. The Bragg SPs are sensitive to sample change, but the propagating plasmon excited in Kretschmann configuration demonstrates greater sensitivity and can operate in highly scattering samples, such as biological fluids. Therefore, Kretschmann configuration is best suited for biosensing, whereas other modes may be desirable for situations requiring a free optical axis, simplified optical scheme (no prism), or flow through analysis. SP excitation by darkfield or transmission modes is desirable for coupling with

a scanning probe microscope (as discussed in chapter 6). Transmission spectroscopy also facilitates flow through, rather than flow over, analysis, which has demonstrated an increase in sensitivity of 6×[149] due to increased analyte binding efficiency and binding to regions of greatest field intensity within the hole. However, Kretschmann configuration remains more sensitive for biosensing and has not been previously investigated in the NIR, which may further increase sensitivity. Furthermore, situations of increased binding efficiency within the holes may be developed and the SPs may be tailored by structural parameters and azimuthal angle of incident wavevector.

Chapter 3

DEVELOPMENT AND CHARACTERIZATION OF NIR-SPR INSTRUMENTATION

3.1 Introduction

SPR spectroscopy is commonly performed in the visible range of the electromagnetic spectrum resulting in a plasmonic wave penetrating approximately 250 nm into the dielectric material with lateral propagation length of 15-20 μm and sensitivity to bulk RI changes approaching 3000 nm/RIU for configurations utilizing 50 nm continuous gold films in aqueous media ($\eta = 1.333$).[45] The sensitivity to RI change is connected to the excitation wavelength and has been shown to increase accordingly.[45, 125] Transitioning to longer excitation wavelengths simultaneously increases the penetration depth into the dielectric, providing a response to RI changes that more closely resembles the bulk sample rather than its surface [45], as well as an increased lateral propagation length.[166] Longer excitation wavelengths may be used to investigate novel materials that have displayed plasmonic properties in the infrared (IR) range. In particular, conducting metal oxides (e.g. indium-tin oxide),[167] nanostructured arrays (refer to chapter 5),[168, 96] and, more recently, graphene,[169] have all shown great promise as new materials for sensing applications. Additionally, the penetration depth may be tailored throughout this region to suit different analyte architectures and types as illustrated in figure 3.1 and discussed in section 1.7.

Most optical configurations used for IR-SPR spectroscopy measurements have relied on custom optics and bread-board configurations guiding the IR beam from the source, or spectrometer, to the plasmonic surface by either optical fibers[170] or open paths.[171, 172] GWC Technologies commercializes the SPR 100 accessory,[173] a pre-packaged NIR-SPR solution utilizing the beam coupled out of a conventional

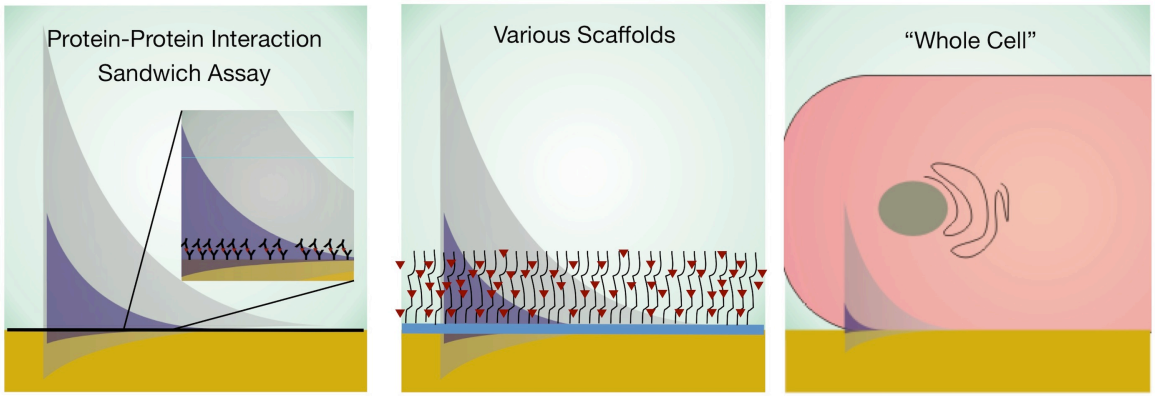

Figure 3.1: SP penetration depth fitting to different analytes. Nanostructured SPR substrates exhibit smaller penetration depths (purple) than continuous gold films (grey), both of which are variable with SPR wavelength.

bench-top FTIR spectrometer, while employing custom optics and an external detector to generate and detect the SPR response. Although comparatively straightforward to implement, the SPR 100 displays the inherent financial drawback associated with dedicated optics and detector in addition to requiring the use of a Thermo Scientific FTIR spectrometer, limiting universal access of the technique.

Recently, Menegazzo et al. described a variable angle accessory originally designed for reflectance-absorption IR spectroscopy and subsequently modified for SPR analysis.[48] This approach displayed the advantage of interchangeability between different brands of IR spectrometers in addition to lowering the initial cost to begin SPR measurements by utilizing the FTIR spectrometer's native detector and optical train. Overall, the modified IR-SPR platform displayed an 8x improvement in sensitivity compared to vis-SPR analysis while providing the ability to tune the excitation wavelength over a wide range (≈700 - 1550 nm). While this approach was successfully implemented for static measurements, low optical throughput due to the use of apertures resulted in low signal-to-noise ratios translating into time-consuming spectral averaging. Furthermore, creeping mechanical drift in the system, inconsequential to IR reflectance spectroscopy and the accessory's originally intended purpose, rendered

temporal SPR spectroscopic analysis of dynamic systems impractical. Therefore, a second generation IR-SPR accessory, described here, was designed and constructed to overcome the limitations presented by the modified approach.

This chapter describes in detail the optical and mechanical components utilized in the second-generation platform, along with all analytical figures of merit required for a complete analytical characterization. Particular effort was devoted to minimize mechanical drift, resulting in a stable signal well-suited for dynamic reactions. The SPR response of gold in the NIR range is highlighted herein to facilitate comparison with previous reports, however, the accessory was designed with sufficient flexibility of input parameters and optical components to accommodate a range of novel materials.

3.2 Experimental methods

3.2.1 Instrumentation

Spectra were collected on a Bruker Optics (Billerica, MA) Vertex 70 FTIR spectrometer equipped with a halogen broadband NIR source, room-temperature indium-gallium-arsenide detector, and a calcium fluoride beamsplitter. IR-SPR spectra were recorded using two variable angle IR-SPR accessories: an Autoseagull (Harrick Scientific, Pleasantville, NY) variable angle reflectance accessory custom-modified for SPR measurements and a second generation accessory engineered specifically for IR-SPR spectroscopy, which will be the focus of this contribution. A detailed description and characterization of the modified Autoseagull was previously presented by Menegazzo et. al.[48] and pictured in 2.13. To simplify the following discussion, the two accessories will be simply referred to as "Autoseagull" or "v2", respectively, throughout the following text. Measurements with the v2 accessory were acquired with 100 co-additions, 0.5 mm source aperture, 3 mm accessory iris, 100× electronic signal amplification, and 8 cm^{-1} resolution at ≈22°C (unless otherwise noted). Measurements with the Autoseagull accessory were acquired with similar parameters with the exception of slight adjustments for throughput to a 1 mm source aperture and 10× electronic signal amplification (unless otherwise noted). Spectra were acquired with p- and s- polarized light,

then ratioed (I_p/I_s) to produce the final SPR spectrum. Gold-coated SPR substrates were optically coupled to BK-7 prisms with RI matching fluid (RI=1.5100) (Cargille Laboratories, Cedar Grove, NJ).

3.2.2 Gold surface preparation

Circular (Fisher Scientific, Fair Lawn, NJ, ϕ = 25 mm) and rectangular glass coverslips (Electron Microscopy Sciences, Ft. Washington, PA, 10.5 x 35 mm) were used for the Autoseagull and v2 accessory, respectively. The glass coverslips were cleaned by immersion in boiling piranha solution (3:1 (v/v) concentrated H_2SO_4: 30% H_2O_2 (Fisher Scientific, Fair Lawn, NJ) *Caution: Piranha solution is strongly oxidizing and should be handled with great care*) for at least one hour, then copiously rinsed with deionized water and actively dried with nitrogen gas stream (Keen Compressed Gas Co., Wilmington, DE). The clean and dry coverslips were immediately coated in a DC magnetron sputterer (Cressington Scientific Instruments Ltd., model 308R, Watford, UK) with 5 nm chromium (99.95$^+$%, Kurt J. Lesker Co., Clairton, PA) functioning as an adhesion layer and 50 nm gold (99.99%, ESPI Metals, Ashland, OR) layer. Gold-coated coverslips were used without delay following sputter deposition.

3.2.3 Beam path and optical alignment

A simplified ray-tracing diagram of the v2 accessory is shown in Figure 3.2a along with a front-view photograph of the accessory (Figure 1B). Converging light from the spectrometer entering the sample compartment is collimated by using an uncoated BK-7 biconcave lens (f = -100.0 mm, Thorlabs, Newton, NJ), through an adjustable iris restricting the diameter of the infrared beam and minimizing stray light. The beam is re-directed 90° upwards by the mirror labeled M1 towards a rotating mirror (M2) responsible for guiding the beam towards the internal reflection element, a BK-7 dove prism (10 mm H x 10 mm W x 42.40 mm L, Thorlabs, Newton, NJ), at the desired incident angle. The internally reflected beam is returned to the spectrometer after being steered through two additional mirrors (M3 and M4) and subsequently through

a second biconcave lens and a zinc selenide polarizer (Edmund Optics, Barrington, NJ). The divergent, polarized beam is finally re-focused onto the detector element by an ellipsoidal mirror (part of the spectrometer's optical train).

By adjusting the two rotating mirrors (M2 and M3) and the prism's vertical position, the incident angle can be changed as desired. The two adjustable mirrors in Figure 3.2(a) are connected to a gear system, which simultaneously, and equally, rotates both M2 and M3 by means of a knurled wheel handle located on top of the accessory. A detailed front-view illustration and a photograph of the gear system is shown in Figures 3.2(c) and 3.2(d). The gear system consists of a 1:10 gear ratio mechanism, which in turn is connected to a right-hand worm gear. On opposite sides of this worm gear, two bronze worm gears equipped with anti-backlash springs are fixed onto a carbon steel shaft. The anti-backlash springs provide constant tension in the mechanism, ultimately preventing free movement of the rotating mirrors. A timing pulley is fixed on the same steel shaft, meaning that movement of the worm gear produces identical motion of the timing pulley. Finally, a timing belt transfers motion to a second timing pulley, which is directly connected to the rotating mirror mount on the front of the accessory. A US Digital (Vancouver, WA) X3M MEMS inclinometer fixed onto M3 provides readout of the angle of the reflected beam incident onto the in-coupling facet of the internal reflection element. The angle at the internal reflection point can then be calculated from the inclinometer readout. The optical path configuration employed requires that a change in incident angle must be accompanied by a change in the vertical position of the prism to ensure that the internal reflection point remains at the center of the prism. An Igus (East Providence, RI) Drylin SHT leadscrew table equipped with an anti-backlash mechanism allowed for precise vertical positioning of the prism. The table was further modified to provide a 48 mm travel within the constrained dimensions of the accessory (290 mm H x 190 mm W x 150 mm D). To further minimize possible residual backlash, incident angles were consistently approached from 7° above and 20° below the incident angle for the v2 and Autoseagull accessory, respectively.

Optical alignment of the v2 accessory was achieved by centering a helium neon

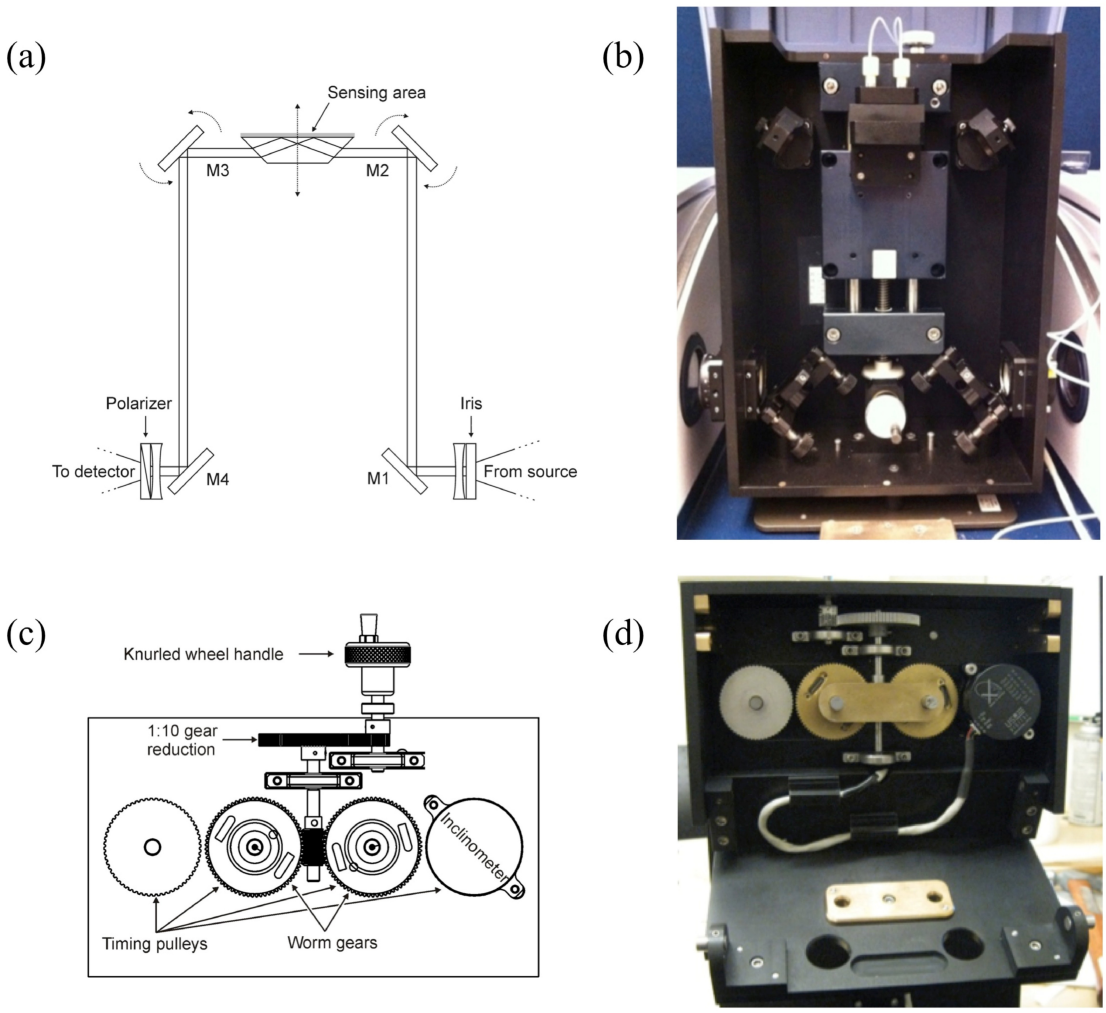

Figure 3.2: (a) Simplified ray-tracing illustrating the beam-path as it passes through the different optical components of the IR-SPR accessory. (b) Photograph showing the fully assembled accessory within the sample compartment of the FTIR spectrometer. (c) Schematic (with timing belts removed for clarity) and (d) photograph of the gear system responsible for rotating the in- and out-coupling mirrors (M2 and M3).

laser (632.8 nm, Research Electro-Optics, Boulder, CO) through the accessory. The accessory and laser were both carefully leveled on breadboard platforms. Mirrors M2 and M3 were immobilized at 45° with a custom fixture, while mirrors M1 and M4 were fixed on kinematics mounts (Thorlabs, Newton, NJ), also at 45°, enabling fine-tuning. Finally, mirrors M1 and M4 were slowly adjusted until the laser beam illuminated center markings fixed on each mirror. However, despite a meticulous alignment procedure a small discrepancy was inevitably observed between the incident angles measured by the inclinometer and those determined by Fresnel modeling of the SPR spectra. Additional details are presented in later sections of this contribution.

Finally, the accessory was mounted on a standard base-plate designed by the instrument manufacturer to facilitate integration of different components into the spectrometers sample compartment. A flow cell with an internal volume of 0.6 mL was fitted to the topside of the prism to facilitate solution exchange.

3.2.4 Bulk Sensitivity

Bulk sensitivity ($\Delta\lambda_{SPR}/\Delta\eta$) was calculated from the shift induced by RI calibration standards of varying sucrose ($\geq$99.5%, Sigma-Aldrich, St. Louis, MO) concentrations prepared in deionized water at room temperature ($\approx$ 22°C). While wavelength-dependent values for RI of the sucrose solutions are not readily available, η of glucose solutions determined by effective medium approximation may be used since sucrose and glucose exhibit negligible (<0.0001 RIU) RI differences at a similar concentration.[171, 174]

3.2.5 Angular calibration and SPR wavelength determination

The angle of incidence in the IR-SPR v2 accessory was determined by matching theoretical SPR spectra of specific incidence angle to experimental SPR spectra in deionized water. Theoretical SPR spectra were calculated using custom MATLAB code based on Fresnel's equations[170] with wavelength specific RI values for water obtained

from Segelstein[175], gold from Johnson and Christy[176] while BK-7 values were calculated using dispersion coefficients available in Schott Glass product catalog.[177] The chromium adhesion layer was omitted from calculations due to the lack of reliable RI values for λ >1.24 μm, however the practically insignificant difference of modeled λ_{SPR} with and without chromium (for λ >1.24 μm) substantiates omission. The location of SPR dip minimum was determined by calculating the zero of the derivative of a second order polynomial fit of the parabolic SPR dip. The angle of incidence used for modeling is considered a match to the experimental angle when the difference between experimental and theoretical minima is <1 nm.

3.3 Incident angle and bulk sensitivity calibration

The abscissa in IR spectra is commonly reported in terms of wavenumber (cm^{-1}) while SPR data is presented in terms of λ_{SPR} (nm). When possible, figures of merit for the accessory will be presented as $\tilde{\nu}_{SPR}$ (cm^{-1}) and λ_{SPR} (nm) in order to facilitate interpretation of the results by representatives of both fields. With the current optical components, the IR-SPR v2 accessory enables acquisition of SPR spectra in the 14,300 - 4,200 cm^{-1} (700 - 2,400 nm) range with tunable SPR excitation wavelength and sensitivity by incident angle adjustment. The angle on the incident mirror (M2) may be adjusted with precision of 0.001° and standard deviation in the readout of 0.005° observed over a duration of at least 12 hrs, allowing for exquisite control of the desired $\tilde{\nu}_{SPR}$ (λ_{SPR}). Comparison between exemplary experimental and theoretical spectra for various incident angles is shown in Figure 3.3.

The theoretically matched incident angle was compared to the angle calculated from the inclinometer readout of the mirror position and beam path geometry. The difference between the geometrically calculated (by ray-tracing) (θ_{geo}) and theoretically matched (θ_{theor}) angle of incidence ranges from 1.10° to 1.35° for $\tilde{\nu}_{SPR}$ = 14,620 - 7,270 cm^{-1} (λ_{SPR} = 684 - 1375 nm), with a linear relationship described by θ_{theor} = 1.0353 $\times\theta_{geo}$ − 1.0429 (R^2 = 0.9999). Fresnel modeling fails to match experimental spectra only for angles near the critical angle of BK-7/water (61.8° in Figure 3.3), however

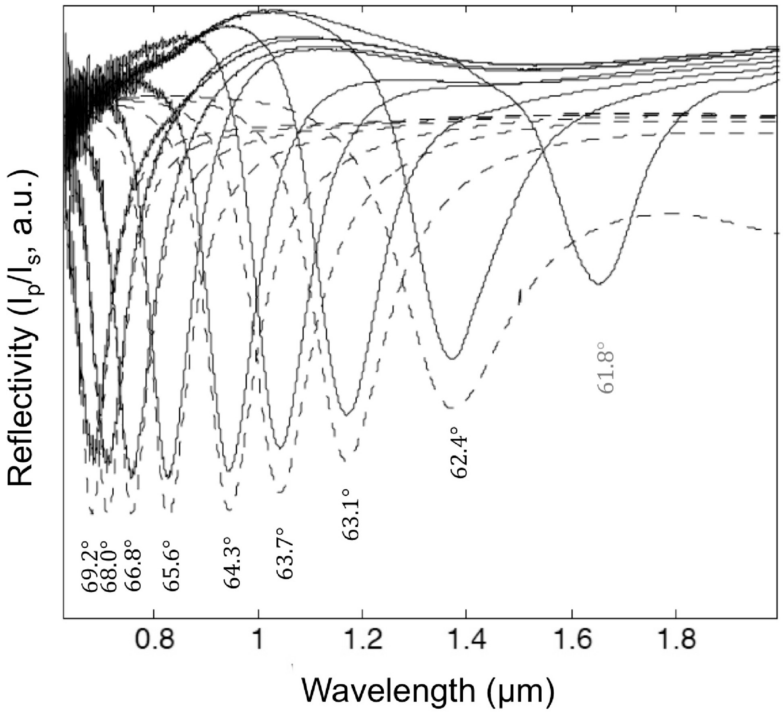

Figure 3.3: Experimental (—) and theoretical (- - -) SPR spectra at different incident angles. Listed incident angle calculated by Fresnel modeling.

the linear fit may be extrapolated to this region to adjust the angle by inclinometer readout to the theoretically matched angle. For example, the spectrum collected at a geometric angle of 60.73° (λ_{SPR} = 1650 nm) corresponds to a theoretical angle of 61.8° presented in grey in Figure 3.3. The differences observed between θ_{geo} and θ_{theor} are most likely due to a combination of effects from minor misalignment of the accessory with respect to the incoming beam and the possible error in the inclinometer readout (up to ± 0.4° according to manufacturer specifications). The angular mismatch is not detrimental to measurements collected with the accessory since it may be mathematically compensated for and there is high reproducibility in adjusting the incident angle, as will be discussed a later section. The angle by inclinometer readout may be converted to the theoretically matched angle by the linear fit. For instance, the theoretical angle for the SPR spectrum collected at an inclinometer angle of 61.93° ($\tilde{\nu}_{SPR}$=8532 cm^{-1}) translates to a "true" incident angle of 63.05°.

As the incident angle is decreased (and wavelength is increased), bulk sensitivity over a linear response range shows an increase by approximately 8-fold, from -97,242 cm^{-1} RIU^{-1} (4,983 nm RIU^{-1}) to -250,946 cm^{-1} RIU^{-1} (38,534 nm RIU^{-1}), for plasmonic excitation ranging from 14,144 cm^{-1} (707 nm) to 8475 cm^{-1} (1180 nm). Calibration of the v2 accessory with sucrose solutions is presented in Figure 3.4. The bulk sensitivity (∼nm/RIU) for λ_{SPR} (nm) between those measured may be interpolated from the second order polynomial fit to m vs. λ_{SPR}; $m = 0.0976(\lambda_{SPR})^2 + 113.0(\lambda_{SPR}) - 36251, R^2 = 0.994$.

3.4 Parameter selection for high throughput and SPR dip quality

The quality of the SPR spectra may be affected by native components of the spectrometer and accessory and should be evaluated for greatest SPR dip quality based on optical throughput and sharpness of the peak. Factors influencing the SPR spectral profile include the spectrometer's aperture size and the size of the iris located at the entrance port on the accessory. The assessment of the aperture is specific to the Bruker Optics Vertex 70 FTIR spectrometer used in this study, and should be similarly

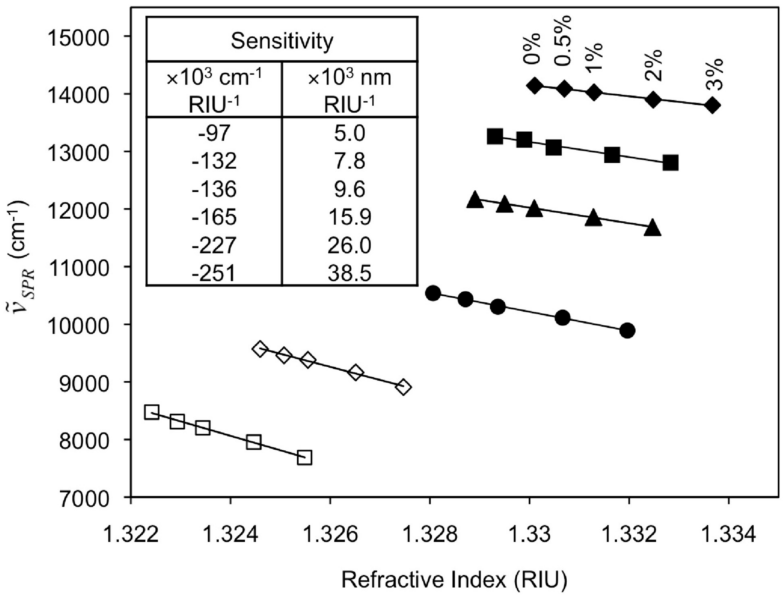

Figure 3.4: Bulk sensitivity to sucrose solutions ranging in concentration from 0% (pure water) to 3% w/w spanning incident angles from 68.6° to 64.06°.

assessed for different spectrometers. The optimal balance was achieved by employing a 0.5 mm aperture in the spectrometer and a 3 mm iris within the accessory (refer to Figure 3.5). The choice in parameters resulted from a compromise between high optical throughput and sharp SPR dip features. The ratio of the full width at half attenuation to the attenuation (FWHA/A) of the plasmonic feature is used to define the sharpness of the SPR dip as a measure of the SPR resolution.[44, 54] Low values for the FWHA/A are associated with more desirable, "sharper", dips. At $\tilde{\nu}_{\mathrm{SPR}}$ of 6700 cm^{-1}, the FWHA/A significantly increases from 3680±60 cm^{-1} to 7370±30 cm^{-1} as the aperture diameter is increased from 0.5 mm to 5 mm, making 0.5 mm the preferable choice. Furthermore, at angles of incidence above approximately 65°, back reflections at different optical interfaces for aperture diameters above 1 mm result in multiple, potentially convoluting SPR dips, rendering larger diameters additionally undesirable. Iris diameters of 3 mm and 2 mm produce similarly low FWHA/A, so the optimal iris diameter of 3 mm is selected based on higher optical throughput. At 3 mm iris diameter, the FWHA/A is 4860±270 cm^{-1} at 6100 cm^{-1} and 1740±220 cm^{-1} at 13,450

cm^{-1}. Also to be noted, $\tilde{\nu}_{SPR}$ changes with iris size, again, due to minor misalignment of the incident beam with respect to the accessory as indicated in the difference between geometric and theoretical incident angle.

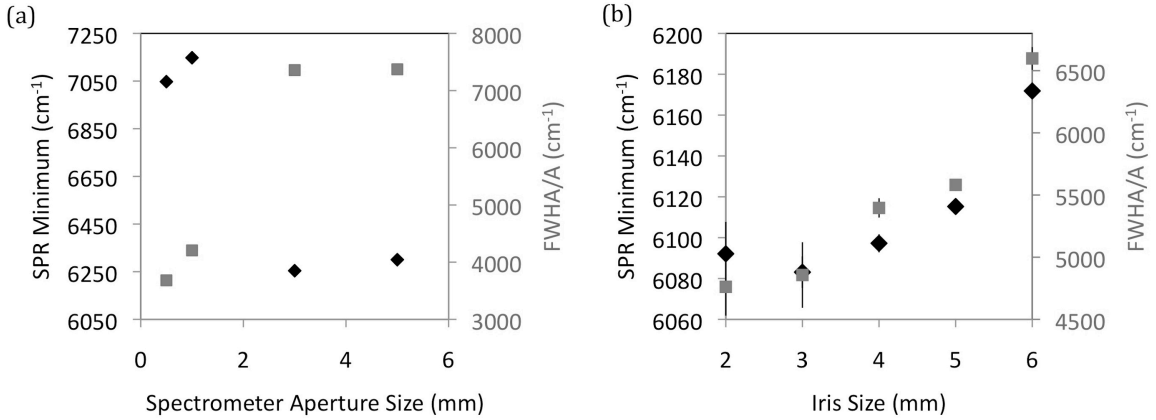

Figure 3.5: SPR minimum (λ_{SPR}) (♦) and peak FWHA/A (■) for various aperture and iris size. The analysis of the aperture size is specific to the Bruker Optics Vertex 70 FTIR spectrometer.

3.5 Evaluation of stability metrics for two NIR-SPR accessories

The v2 accessory also offers improved temporal stability and reproducibility over the modified counterpart, evaluated by deviation in SPR response for bare gold layers in deionized water with respect to time, angle change, and sample change for N number of replicate measurements per K number of trials (Table 3.1). All measurements were acquired at longer wavelengths ($\tilde{\nu}_{SPR}$ ≈7600 cm^{-1}, unless otherwise noted), where bulk sensitivity is highest, specifically to illustrate stability under worst-case scenarios. The v2 accessory shows high stability and reproducibility with angle change demonstrated by converting the observed λ_{SPR} deviation with angle change into angle deviation by matching experimental λ_{SPR} to theoretical SPR spectra evaluated for specific angles. The angles used in modeling to achieve <1 nm difference between theoretical and experimental λ_{SPR} encompass a small range in incident angles of 62.64 ± 0.006°, resulting in a low angle change variability of 0.01% relative standard

deviation. The v2 accessory also exhibits superior overall stability over a period of eight hours (sampled at two-minute intervals with ambient temperature fluctuations of 1.1 ± 0.6° C) and equilibration within ≈1 h, determined by the difference in the highest and lowest $\tilde{\nu}_{\mathrm{SPR}}$; $\Delta\tilde{\nu}_{\mathrm{SPR}}$ <10 cm^{-1}. Of the six representative trials shown in figure 3.6, the largest deviation observed resulted in a drift of ≈80 cm^{-1}, though more frequently lower values (≈20 cm^{-1}) were recorded. In contrast, stabilization of the modified Autoseagull resulted in an unpredictable drift in from 450 cm^{-1} to 50 cm^{-1}, sometimes with no clear indication that stable readings could be achieved. We would like to reiterate that the angular drift observed is not damaging to conventional IR reflectance spectroscopy, but renders kinetic measurements with IR-SPR spectroscopy unreliable. Overall, the v2 accessory shows low temporal drift and short mechanical stabilization periods.

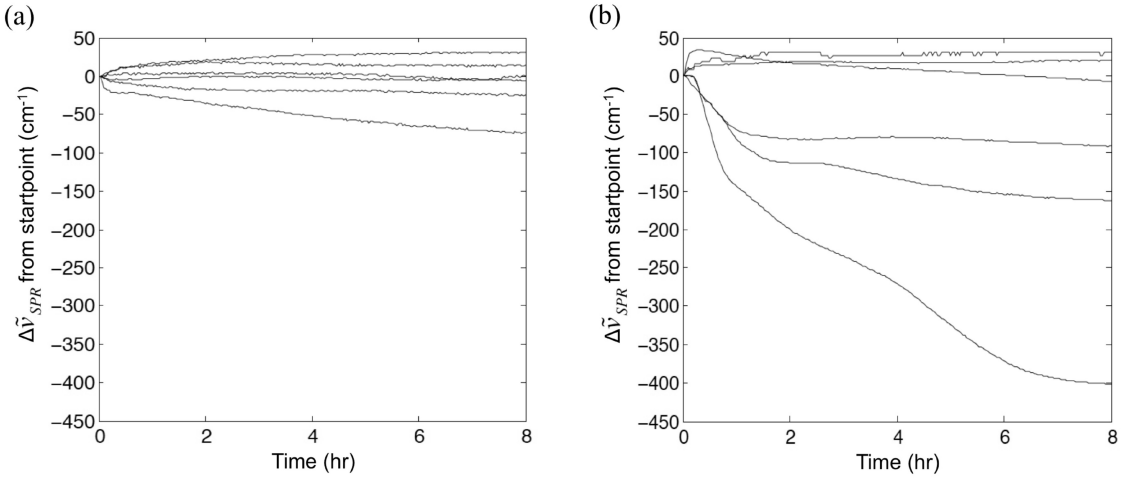

Figure 3.6: Temporal stability of the (a) v2 and (b) modified Autoseagull IR-SPR accessories in water at room temperature with bare gold SPR substrates.

The mechanical robustness of the v2 accessory was further evaluated by recording the deviation in SPR response upon moving several components within the system. The results are included in Table 3.1 for $\tilde{\nu}_{\mathrm{SPR}}$ ≈7600 cm^{-1}, unless otherwise noted.

The sample-to-sample metric quantifies the ability to obtain similar upon disassembling the flow-cell and replacing the gold-coated substrate while maintaining other parameters constant and is, perhaps, one of the most important metrics presented in Table 3.1. SPR spectroscopic measurements often require different substrates for replicate measurements, for example, during biosensing, denaturation of immobilized antibodies imposes a practical limit on the repeated use of the modified surface.[45] Since sensitivity is related to the optical parameters employed, the ability of an instrument to return similar experimental output upon sample change is of clear benefit. A second metric demonstrating the resilience of the designed accessory to mechanical perturbation is reflected by the small change in obtained following replacement of the entire accessory assembly in-and-out of the spectrometer's sampling compartment; on average a deviation of only $\approx$5 cm^{-1} over a total of six measurements using two different gold-coated substrates was recorded. Replace flow-cell involves measurement of following removal and re-attachment of the flow cell without disassembly, while stage re-adjustment encompassed moving the flow-cell 5.3 mm below the ideal stage position and subsequently re-positioning; the ideal position was interpreted as the location on the optical patch yielding the highest throughput. Hence, the v2 accessory offers highly reproducible measurements between replicate samples and various instrument parameter changes over a long time scale, facilitating acquisition of temporal data or high volume, requiring measurements of multiple substrates under similar conditions.

3.6 Capability for kinetic measurements

Spectral averaging is commonly used in both SPR and IR spectroscopies to improve the signal-to-noise ratio at the expense of temporal resolution. The spectroscopic capability for rapid measurements is key to kinetic analysis of protein-protein interactions, a popular application of SPR spectroscopy.[7] To assess the compatibility of the accessory with kinetic measurements, spectral and temporal resolution was calculated from baseline fluctuation of IR-SPR measurements and compared to the resolution typically adopted. The deviation in (λ_{SPR}) over 50 measurements acquired

Table 3.1: Comparison of the stability metrics for the IR-SPR v2 and Autoseagull accessories.

	v2				Modified Autoseagull			
Metric	$\tilde{\nu}_{SPR}$ (cm^{-1})	λ_{SPR} (nm)	N	K	$\tilde{\nu}_{SPR}$ (cm^{-1})	λ_{SPR} (nm)	N	K
Angle change	21	4	3	2	75	13	3	2
Sample-to-sample ($\tilde{\nu}_{SPR} \sim 13\,700\ cm^{-1}$)	68	4	3	2	77	4	3	2
Sample-to-sample ($\tilde{\nu}_{SPR} \sim 8200\ cm^{-1}$)	57	9	3	2	294	42	3	2
Stage re-adjustment	11	2	3	2	...	...	...	...
Replace flow-cell	3	1	3	2	...	...	...	...
Replace accessory into spectrometer	5	1	3	2	...	...	...	...
Aperture change at ($\tilde{\nu}_{SPR} \sim 12\,100\ cm^{-1}$)	4	0	3	1	...	...	...	...
Aperture change at ($\tilde{\nu}_{SPR} \sim 7000\ cm^{-1}$)	0	0	3	1	...	...	...	...
Iris change at ($\tilde{\nu}_{SPR} \sim 13\,500\ cm^{-1}$)	12	1	3	1	...	...	...	...
Iris change at ($\tilde{\nu}_{SPR} \sim 6100\ cm^{-1}$)	8	2	3	1	...	...	...	...

Values reported as variation in SPR response for N number of replicate measurements per K number of trials at $\tilde{\nu}_{SPR} \approx 7600\ cm^{-1}$, unless otherwise noted.

at one minute intervals was calculated for 10 and 100 co-additions following a period of 8 hours ensuring that the measured variation in is not of thermal or mechanical origin. Measurements with 10 co-additions require a collection time of 5 s per spectrum and show a standard deviation of 15 cm^{-1} (or 0.8 nm) at 13,213 cm^{-1} and 0.2 cm^{-1} (or 0.03 nm) at 7,419 cm^{-1}. Comparable deviation was obtained with 100 co-additions which require 48 s per measurement; 3.6 cm^{-1} (or 0.2 nm) at 13,203 cm^{-1} and 0.1 cm^{-1} (or 0.03 nm) at 7,419 cm^{-1}. Note that the deviation is reduced at lower wavenumber due to higher optical throughput, despite increased sensitivity resulting from excitation of surface plasmon polaritons at longer wavelengths. Consistent with the analysis presented by Jung et al.,[73] the limits of detection (LOD) for 10 co-additions at 13,213 and 7,419 cm^{-1} were calculated. The bulk LOD was evaluated from baseline fluctuation and bulk sensitivity as 3.8×10^{-4} RIU at 13,213 cm-1 and 1.7×10^{-6} RIU at 7,419 cm^{-1}. These LODs correspond to a minimum detectable protein ($\eta_a = 1.57$) thickness of 0.12 nm and 0.004 nm in buffered solution (η_s =1.33). Subsequently, this translates to a LOD range of binding protein in solution of 1.2×10^{-6} M to 1.2×10^{-9} M at 13,213

cm^{-1} and 2.0x10^{-8} M to 2.0x10^{-11} M at 7,419 cm^{-1} for a typical binding affinity range of 10^5 L/M to 10^8 L/M[44, 78, 178] and 1.9 nm effective thickness of close packed protein layer.[73] Generally, association and dissociation constants are determined from fitting to binding curves for several concentrations in the nM to mM range measured with resolution on the scale of seconds in visible-SPR spectroscopy.[44, 78, 178, 179, 26] Therefore, the temporal and spectral resolution obtained with 10 co-additions meets the standard requirements for real-time monitoring of protein binding over the NIR wavelength range. Additionally, the resolution at 100 co-additions corresponding to minimum detectable layer thickness of 0.05 nm and 0.002 nm at 13,213 cm^{-1} and 7,419 cm^{-1} is compatible with self-assembly of alkanethiolate monolayers.[180, 97]

3.7 Conclusion

A second generation accessory for IR-SPR spectroscopy was designed to address the limitations associated with a previously developed method based on a modified variable angle reflectance accessory. High temporal stability of the new accessory, resulting from incorporation of elements with anti-backlash mechanisms, rendered the described platform compatible with optical and mechanical requirements for kinetic measurements of, for example, biomolecular interactions. Furthermore, by utilizing the spectrometer's native baseplate, assembly of the accessory into the sample compartment is straightforward, requiring no user input. The accessory was also designed to be highly flexible, displaying the potential to accommodate investigations of different optical materials across different wavelength ranges, with demonstrations of the v2 accessory for sensing and material characterization applications presented in following contributions.

Chapter 4

ADSORBATE-METAL BOND EFFECT ON EMPIRICAL DETERMINATION OF SURFACE PLASMON PENETRATION DEPTH

4.1 Introduction

SPR spectroscopy has become a popular analytical tool for studying surface-based events, particularly as a biosensing platform for investigating protein interactions.[44] A SP decays exponentially with distance perpendicular to the surface and the conditions for matching and exciting the surface plasmon are described by its wavevector, k_{sp}, which depends on the complex permittivity of the solution (ϵ_s) and plasmon supporting material (ϵ_m), equation (1.3). Because complex permittivity relates to the real (η) and imaginary (k) components of refractive index ($\epsilon = (\eta + ik)^2$) this translates to local RI change affecting the k_{sp} and, consequently, the wavelength of incident light creating a SP that couples with the surrounding media. The SPR coupling conditions are sensitive to near surface RI.

There is, of course, a practical difference between 'bulk sensitivity' and 'surface sensitivity'. In many bioanalytical applications of SPR, selectivity is derived from a thin layer of bioreceptors, often antibodies or peptides, attached to the sensor surface. High surface sensitivity, i.e. SPR response to adsorbate loading, is achieved when a greater proportion of the evanescent plasmonic field is occupied by the adsorbate layer rather than the bulk solution [73], a scenario which also reduces contributions from bulk environmental RI fluctuations. Consequently, sensitivity to RI changes within the thin region of analyte binding sites (surface sensitivity) is more informative of sensor performance than is the sensitivity to RI changes throughout the entire penetration depth of the SP (bulk sensitivity).

Matching the analytical volume with the thickness of the analyte layer, so that the analyte layer lies entirely within the sensing volume or occupies the majority of the sensing volume, results in maximal surface sensitivity and selectivity against bulk effects. The analytical volume sensed by the plasmonic field may be estimated from its characteristic penetration depth (l_d), which is defined as the distance from the plasmon supporting surface at which the intensity of the field decays to $1/e$, as illustrated in figure 4.1. [44, 73] The effective refractive index (η_{eff}) observed by the SP is thus the average of the bulk solution RI (η_s) and the adsorbate monolayer RI (η_a) weighted by the portion of the analytical volume resident in each layer:

$$\eta_{\text{eff}} = \eta_s \exp(-2\text{d}/l_d) + \eta_a[1 - \exp(-2\text{d}/l_d)] \tag{4.1}$$

where d is the thickness of the adsorbate monolayer.5 The observed shift in the SPR wavelength, R, following adherence of a monolayer can then be expressed as a function of the bulk sensitivity (m):

$$\text{R} = \text{m}(\eta_{\text{eff}} - \eta_s) \tag{4.2}$$

If the penetration depth is too shallow, a portion of the analyte layer lies above the sensing volume and leads to longer response times for detection schemes limited by molecular diffusion into a sensing layer. Furthermore, if a base organic linker layer or scaffold is used, the adsorbed analyte may only fill a small upper portion of the sensing volume, leading to decreased analytical sensitivity.[181] Likewise, an overly large penetration depth results in an oversized sensing volume that is only partially occupied by the analyte; this reduces sensitivity and leaves the analysis susceptible to interference from bulk RI changes.[182, 183] In this way, characterization of penetration depth would enable selection of sensor conditions that are more optimal for specific analytes.

The key to differentiating between bulk sensitivity and surface sensitivity − and optimizing a sensor for maximum surface sensitivity − lies in determining the penetration depth of the SP. Equation (4.1) and equation (4.2) can be combined to express

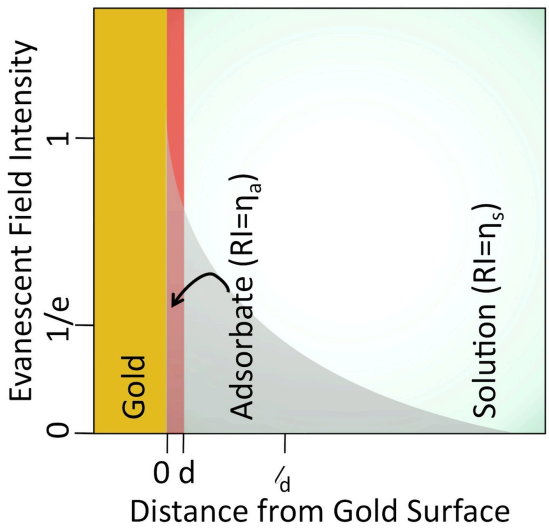

Figure 4.1: Evanescent surface plasmon with intensity decaying exponentially through bilayer of adsorbate with thickness=d and bulk solution. The penetration depth, l_d, is the distance at which the relative field intensity decays to $1/e$.

the penetration depth as a function of instrument response following attachment of a well characterized organic monolayer to the sensing surface:[73]

$$l_d = \frac{-2\mathrm{d}}{\ln(1 - \frac{\mathrm{R}}{\mathrm{m}(\eta_\mathrm{a} - \eta_\mathrm{s})})} \tag{4.3}$$

Here accurate knowledge of the bulk sensitivity (m), bulk solution RI (η_s) and adsorbed monolayer RI (η_a) and thickness (d) are needed to estimate the SP penetration depth.

A flaw in determining SP penetration depth by equation (4.3) occurs with the assumption that R is derived solely from changes in bulk solution or adsorbate monolayer refractive index. Equation (1.3) states that SPR is equally sensitive to changes in the complex permittivity of the solution (ϵ_s) and to changes in the complex permittivity of the SP supporting metal (ϵ_m). Electrochemists are well acquainted with changes in the work function of electrodes (which relates to complex permittivity) following covalent functionalization of the surface. For example, a 4% increase in the surface

resistivity of 40 nm gold films has been observed upon adsorption of various alkanethiolate monolayers that was not observed for physisorbed species.[184] Similarly, Alloway et al.[185] demonstrated a shift in the Fermi level of gold foil samples due to dipole change at the interface upon functionalization. These effects manifest in SPR spectra as anomalously large dampening of the plasmon band upon thiol adsorption[186] and a negative y-intercept for SPR response vs. alkanethiolate layer thickness on silver nanotetrahedrons.[95]

The response following attachment of an adlayer (R) is the sum of two effects, the contribution from changes to ϵ_m derived from attachment of the adlayer ($R_{\epsilon m}$) and the contribution from changes to ϵ_s derived from changes in η_{eff} following attachment of the adlayer ($R_{\epsilon s}$). For equation (4.3) to become accurate, the ensemble response must be replaced by just the response attributable to RI changes in the adlayer: $R_{\epsilon s}$ where $R_{\epsilon s}$ = R - $R_{\epsilon m}$. Equation (4.3) then becomes:

$$l_d = \frac{-2\text{d}}{\ln(1 - \frac{\text{R}-\text{R}_{\epsilon m}}{\text{m}(\eta_a - \eta_s)})} \tag{4.4}$$

Fortunately, as will be discussed below, $R_{\epsilon m}$ can be experimentally determined by extrapolating the observed SPR shift from a homologous series of adlayers to zero length, leaving only the contribution of $R_{\epsilon s}$.

In this chapter, the consequences of employing equation (4.3) versus employing equation (4.4) to determining the SP penetration depth are explored. The reliability in l_d subsequently dictates the reliability of adsorbate parameters derived from it, including the common translation of effective adsorbate thickness into surface coverage and analyte-surface binding affinity constant.[73, 77, 170] Additionally, accurate l_d calculation is valuable for assessing novel nanostructured substrates; for they have shown promise for variably shallower l_d more closely matched to thin adsorbate films as evidenced by improved surface sensitivity compared to conventional planar gold.[54, 187, 188, 189, 96] Penetration depths displayed by nanostructures may reach an order of magnitude below planar gold [188], denoting greater sensitivity to nanometer scale

adsorbate layers of target analytes. Proper characterization of these substrates would lead to a large set of highly sensitive sensor substrates available for finely tuned, analyte specific sensor surfaces. Previous studies have obtained l_d estimates without $R_{\epsilon m}$ for nanostructures and observed greater sensitivity to adsorbate binding over planar gold substrates.[54, 187, 188, 189, 96] These studies provide a working estimate for particular nanostructure l_d's in the visible range but may be expanded and improved by the proposed method.

Further adjustment of l_d and bulk sensitivity may be achieved by varying λ_{SPR} through visible and near-infrared regions as both properties increase with the excitation wavelength used.[69, 48] Preliminary l_d measurements were completed in the NIR to demonstrate adjustability with wavelength, exploit increased precision arising from larger bonding effect response ($R_{\epsilon m}$) and stability of NIR instrumentation, and advance into wavelength regions of novel plasmonic materials. Two adsorbate systems for l_d determination, the commonly used alkanethiolates of varying carbon chain length and a more experimentally practical and time efficient procedure utilizing polyelectrolyte multilayer (PEM) buildup atop an alkanethiolate monolayer, are presented with emphasis on the increased accuracy and precision of l_d calculations by including $R_{\epsilon m}$.

4.2 Experimental methods

4.2.1 SPR spectroscopy measurements

Spectroscopic measurements were acquired on a Bruker Optics (Billerica, MA) Vertex 70 FTIR spectrometer with an improved IR-SPR accessory based on a modified Autoseagull NIR-SPR accessory as previously described.[48] A constant angle setup was used in which the response was measured as a shift in wavelength ($R = \Delta\lambda_{SPR}$) at a fixed angle (Refer to the *Handbook of Surface Plasmon Resonance* [44] for more information). Hereafter, the response is termed $\Delta\lambda_{SPR}$. Measurements were obtained with 100 co-additions, 0.5 mm source aperture, 3 mm accessory iris, 100× electronic signal amplification, and 8 cm^{-1} resolution at ≈22°C. Spectra were measured with p- and s- polarized light, then ratioed (I_p/I_s) to produce the final SPR spectrum.

The Kretschmann configuration NIR-SPR accessory is illustrated in figure 3.2 and a brief description is provided below. The accessory employs uncoated BK-7 biconcave lenses (f = -100.0 mm, Thorlabs, Newton, NJ) to collimate the light within the Vertex sample compartment. An adjustable iris controls spot size and minimizes stray light. Two movable mirrors are positioned to set the angle of light through the prism and incident on the sample substrate. Gold SPR substrates were coupled to the BK-7 prism with RI matching fluid (RI=1.51) (Cargille Laboratories, Cedar Grove, NJ). A zinc selenide polarizer (Edmund Optics, Barrington, NJ) is used to polarize the collected light. A flow cell with 0.6 mL volume was fitted to the topside of the prism for ease of solution exchange in contact with the SPR substrate. Six mL of solution was sufficient to fully replace solution in the flow cell as evidenced by restoration of SPR minima for subsequent water measurements separated by solution exchange with ethanol in this manner. More details regarding the description and characterization of the instrument have been previously presented in chapter 3 and the publication [49].

4.2.2 Gold sensor surface preparation

Details of cleaning slides and fabricating continuous gold films may be found in section 3.2.2. To pattern substrates with nanohole arrays, the procedure in section 2.3 was followed. Gold-coated coverslips were used immediately after sputter deposition.

4.2.3 Bulk sensitivity calibration

Bulk sensitivity ($m = \Delta\lambda_{SPR}/\Delta\eta$) was calculated from response to RI calibration standards of varying sucrose ($\geq$ 99.5%, Sigma-Aldrich, St. Louis, MO) concentrations prepared in deionized water at room temperature ($\approx$22°C). Wavelength dependent values for RI of the sucrose solutions are not readily available in literature. Alternatively, η of the glucose solutions determined by effective medium approximation may be used since sucrose and glucose exhibit negligible ($<$ 0.0001 RIU) RI differences.[171, 174] The sensitivity term used for l_d calculations was measured over a concentration range that covered a SPR wavelength shift similar to the adsorption

process investigated. Solutions containing 0.5-3% (w/w) sucrose were selected for alkanethiolate adsorption ($\Delta\lambda_{\mathrm{SPR}} \approx 20$ nm), while 0.5-12% (w/w) were selected for PEM formation ($\Delta\lambda_{\mathrm{SPR}} \approx 120$ nm).

4.2.4 Monolayer formation

Self-assembled alkanethiolate monolayers ($\mathrm{HS(CH_2)_xCOOH}$, $x = 2, 5, 7, 11, 15$) were formed on freshly sputtered gold slides by immersion in 10 mM solution of 3-mercaptopropionic (99^{+}%, Acros Organics, Fair Lawn, NJ), 6-mercaptohexanoic (90^{+}%, Santa Cruz Technologies, Santa Cruz, CA), 8-mercaptooctanoic (95%, Sigma-Aldrich, St. Louis, MO), 12-mercaptododecanoic (96%, Sigma-Aldrich, St. Louis, MO) or 16-mercaptohexadecanoic (90%, Sigma-Aldrich, St. Louis, MO) acid in absolute ethanol (99.5^{+}%, Sigma-Aldrich, St. Louis, MO). The chemicals were used as received with the exception of the 16-mercaptohexadecanoic acid, which was recrystallized from absolute ethanol. Just before use, the samples were rinsed with copious amounts of ethanol and dried with a nitrogen gas stream. One set of three samples of each chain length and bare gold were prepared and SPR spectra were acquired at an angle of incidence (θ_{inc}) of 66.5° in deionized water. A second set of triplicate samples were prepared and measured in deionized water at six incident angles: 68.3°, 67.0°, 65.7°, 64.4°, 63.8°and 63.1°. For the second series, each sample was loaded and measured at each angle before exchanging with the next sample.

4.2.5 Polyelectrolyte multilayer formation

In situ SPR spectroscopy measurements at θ_{inc} =67.3°were acquired during formation of polyelectrolyte multilayers (PEM). PEMs of polyallylamine hydrochloride (PAH) (15,000 MW, Sigma-Aldrich, St. Louis, MO) and polystyrene sulfonate (PSS) (70,000 MW, Acros Organics, Fair Lawn, NJ) were formed by electrostatic self-assembly within the flow cell (refer to Figure 4.2). An initial bare gold SPR wavelength baseline in 0.75 M NaCl (Fisher Scientific, Fair Lawn, NJ) was established before sequentially injecting water, ethanol, and 10 mM mercaptopropionic acid (MPA) in absolute

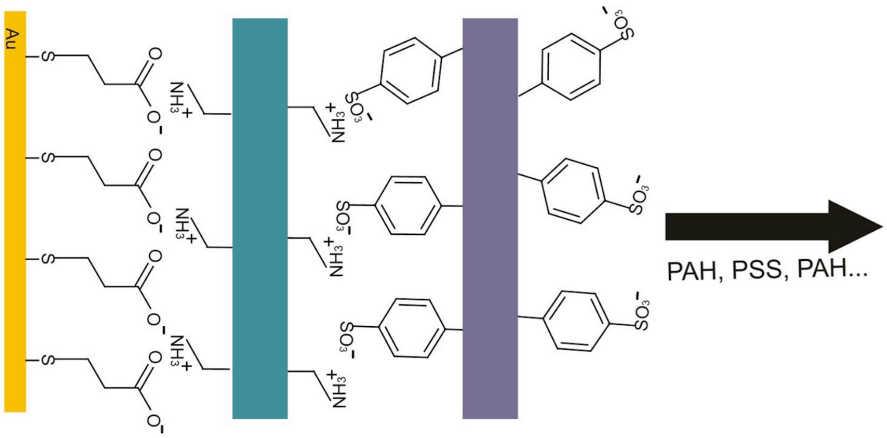

Figure 4.2: Polyelectrolyte multilayer formation atop mercaptopropionic acid monolayer on gold surface with alternating layers of polyallylamine hydrochloride (PAH) and polystyrene sulfonate (PSS).

ethanol. The MPA was allowed to self-assemble overnight, forming a negatively charged monolayer precursor layer. The monolayer was exhaustively rinsed with over 90 mL of ethanol to ensure removal of physisorbed molecules and the SPR wavelength was measured. Steps of alternating 5 mg/mL PAH and 5 mg/mL PSS in 0.75 M NaCl solutions were exchanged in 6 mL aliquots at a flow rate of 1.6 mL/min and left undisturbed for self-assembly for an additional 30 min. Between each PEM solution, the layers were rinsed with 0.75 M NaCl. A Dynamax (Rainin, Columbus, OH) peristaltic pump and series of solenoid valves (The Lee Co., Essex, CT) operated by custom Labview (National Instruments Corporation, Austin, TX) virtual instruments were used to exchange solution between PAH, NaCl, and PSS for the desired number of PEM layers.

4.2.6 Atomic force microscopy

The thickness of the polyelectrolyte multilayers was determined by atomic force microscopy. Samples from SPR analysis were used in measurements of thickness of thirteen PEM layers. Samples with 1, 3, 5, 7, 9 and 11 PEM layers were formed as previously described after self-assembly of the monolayer precursor in a petri dish.

After PEM formation, samples were stored in a petri dish in 0.75 M NaCl solution until immediately prior to analysis. The underside of the sample was dried and secured to a 15 mm AFM specimen disc. The sample was maintained in hydrated form with 0.75 M NaCl at all times. The PEM and gold layers were carefully scratched with a razor blade and the step height was measured with a Nanoscope IV AFM (Bruker AXS, Santa Barbara, CA) equipped with a liquid cell accessory and silicon nitride DNP-10 probe (Bruker AXS, Camarillo, CA). A silicon o-ring was used to enclose the liquid cell and preclude solution evaporation. Cantilevers with 0.06 N/m force constant were used in tapping mode. Rectangular images were acquired at a scan rate of 1 Hz and image size of 15-20 μm length $\times$ 3-5 μm width. The Nanoscope software was used to calculate height and average roughness for three spots on each sample. A silicon TAP-300-G probe (Innovative Solutions Bulgaria Ltd., Sofia, Bulgaria) was used in tapping mode in air to measure the gold thickness of a bare gold sample sputtered simultaneously with each PEM sample substrate. The total PEM layer thickness was calculated by subtracting the gold thickness from the PEM-gold thickness in liquid.

4.3 Determination of penetration depth by alkanethiolate monolayer formation

The importance of incorporating the bonding effect on the metal permittivity, ϵ_m, during empirical l_d determination is highlighted by assessing l_d calculations from a series of alkanethiolate self-assembled monolayers. SPR response to the formation of alkanethiolate monolayers of different lengths on gold demonstrates a change in ϵ_m of the metal upon thiol bonding that should be included in the calculations for an accurate l_d determination (equation (4.4)). The observed response (R=$\Delta\lambda_{\mathrm{SPR}}$ for constant angle setup) is a function of two effects; an increase in η_{eff} from displacing water with closely packed carbon chains near the sensing surface changes ϵ_s and covalent binding of the thiolate to the gold impedes the free flow of electrons at the gold surface and impacts ϵ_m. The SPR shift attributed to changes in ϵ_m ($\Delta\lambda_{\mathrm{SPR},\epsilon m}$) were determined by extrapolating the linear fit of measured $\Delta\lambda_{\mathrm{SPR}}$ vs. monolayer thickness to zero

monolayer thickness (Figure 4.3, grey). The $\Delta\lambda_{\mathrm{SPR}}$ for each functionalized sample was calculated as a difference in λ_{SPR} from pristine, bare gold surfaces, and is presented for a single incident angle of 66.54° where $\Delta\lambda_{\mathrm{SPR},\epsilon m}$ is -5.6 ± 0.2 nm for binding a thiol on 50 nm thick gold film with λ_{SPR} of 772.1 nm. Consequently, λ_{SPR} of the gold with altered permittivity due to thiol bonding ($\lambda_{\mathrm{SPR,Au-S}}$) reduces the SP resonant wavelength to 766.5 nm.

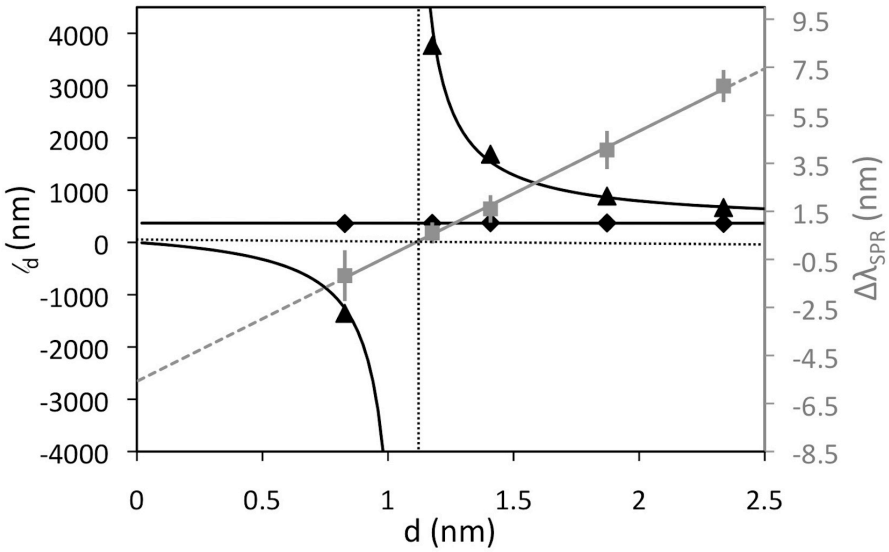

Figure 4.3: (right y-axis) $\Delta\lambda_{\mathrm{SPR}}$ from bare gold for adsorption of different monolayer thickness (■). Linear fit of $\Delta\lambda_{\mathrm{SPR}}$ vs. d; m = 5.2±0.1, b = $\Delta\lambda_{\mathrm{SPR},\epsilon m}$ = -5.6±0.2 and R^2 = 0.998. Error bars represent the standard error of the mean for N = 3,5,6,7,3 samples. (left y-axis) l_d determined at varying monolayer thickness calculated with (♦) and without (▲) $\Delta\lambda_{\mathrm{SPR},\epsilon m}$ compensation (by equation (4.3) with $\Delta\lambda_{\mathrm{SPR}}$ or equation (4.4) with $\Delta\lambda_{\mathrm{SPR}}$-$\Delta\lambda_{\mathrm{SPR},\epsilon m}$, respectively). Error bars on l_d with $\Delta\lambda_{\mathrm{SPR},\epsilon m}$ representing deviation due to error in $\Delta\lambda_{\mathrm{SPR},\epsilon m}$ are present but not visible due to scale. l_d lines are calculated across shift values from $\Delta\lambda_{\mathrm{SPR}}$ vs. d linear fit.

Potential problems with determining SP penetration depth via equation (4.3) are evident in figure 4.3. The black triangles represent penetration depth estimates from the five thiol-homologs employed to determine $\Delta\lambda_{\mathrm{SPR},\epsilon m}$. The l_d in water for thiolated gold was calculated with monolayer parameters, η_a and d, retrieved from Bain et al.[180] and bulk sensitivity measured at the specific incident angle (refer

to section 3.3). Additionally, bulk sensitivity remains practically constant across this small range of alkanethiolate functionalizations, hence values for bare gold can be used. Bulk sensitivity for bare and alkanethiolate functionalized gold are statistically similar with 95% confidence (t=1.52), Figure 4.4. The sensitivity for bare gold is 6267 ± 740 nm/RIU and sensitivity for $HS(CH_2)_xCOOH$ functionalized gold where x=2,7,11,15 is 5555 ± 215 nm/RIU. Similarly, Jung et al. established a 0.7% difference in bulk sensitivity for a bare and decanethiol modified gold substrate.[73]

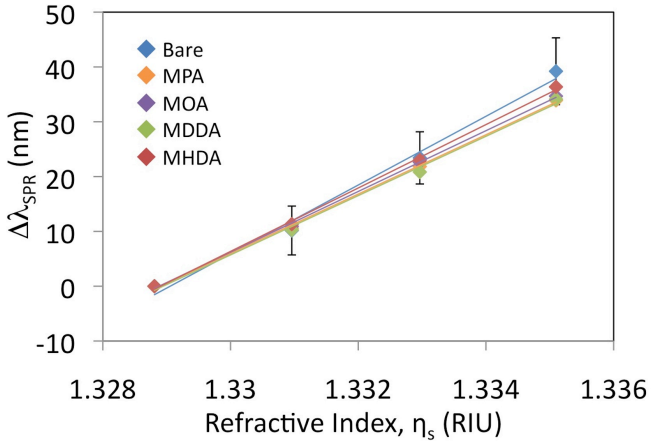

Figure 4.4: Bulk sensitivity of bare and alkanethiolate (MPA, MOA, MDDA, MHDA) functionalized gold at $\theta_{inc} = 66.98°$. Error bars on bare gold represent ±s for n=3.

Employing the thinnest adlayer, 3-mercaptopropionic acid, a negative penetration depth is estimated. Here $\Delta\lambda_{SPR,\epsilon s}$ is positive, but of lesser magnitude than the negative $\Delta\lambda_{SPR,\epsilon m}$; consequently a net blue shift in λ_{SPR} is measured and a negative l_d determined. For the next thickest observed adlayer, 6-mercaptohexanoic acid, a SP penetration depth of nearly 4 microns is calculated. Here the positive $\Delta\lambda_{SPR,\epsilon s}$ is of slightly greater magnitude than the negative $\Delta\lambda_{SPR,\epsilon m}$. The reasons that an unreasonably large penetration depth would be determined are evident in close inspection of equation (4.3). In the case where $\Delta\lambda_{SPR,\epsilon m}$ and $\Delta\lambda_{SPR,\epsilon s}$ are of equal magnitude and opposite sign, $\Delta\lambda_{SPR}$, and consequently the denominator of equation (4.3), is zero.

The calculated penetration depth thus is negative if $\Delta\lambda_{\mathrm{SPR},\epsilon s} < -\Delta\lambda_{\mathrm{SPR},\epsilon m}$ and approaches negative infinity as these two values converge in this direction. Similarly, the calculated penetration depth is positive when $\Delta\lambda_{\mathrm{SPR},\epsilon s} > \Delta\lambda_{\mathrm{SPR},\epsilon m}$ and approaches positive infinity as the two values converge from this direction.

When $\Delta\lambda_{\mathrm{SPR},\epsilon s} >> -\Delta\lambda_{\mathrm{SPR},\epsilon m}$ the impact of binding induced changes on ϵ_m become negligible. This is seen in figure 4.3 (▲) where the estimated penetration depth converges to a single value as the adlayer thickness increases. For this reason, Jung recommended using relatively thick adlayers, between 10% and 25% of l_d, to determine plasmonic penetration depth.[73] However, a bias in the estimated penetration depth remains as long as changes to the metal complex permittivity are not included in the calculations.

When the response to change in metal permittivity from the Au-S bond ($\Delta\lambda_{\mathrm{SPR},\epsilon m}$ or $\mathrm{R}_{\epsilon m}$) is included in the calculation of l_d (equation 5), the estimation of l_d does not vary with the thickness of the adlayer, d, used in the empirical calculations (Figure 4.3, ♦). As expected from the models, l_d, estimated from equation (4.3) converges to the l_d, estimated from equation (4.4) as the thickness of the adlayer increases and the relative contribution of $\Delta\lambda_{\mathrm{SPR},\epsilon m}$ to $\Delta\lambda_{\mathrm{SPR}}$ decreases (compare ▲ to ♦ in Figure 4.3).

Repeated determination of l_d on planar gold where the incident angle is changed to tune $\Delta\lambda_{\mathrm{SPR,Au-S}}$ over a wavelength range of 701-1152 nm verifies the importance of including $\Delta\lambda_{\mathrm{SPR},\epsilon m}$ throughout the accessible NIR wavelength region. As $\Delta\lambda_{\mathrm{SPR}}$ advances through the NIR, $\Delta\lambda_{\mathrm{SPR},\epsilon m}$ becomes larger, increasing from a -5.3 nm shift with $\Delta\lambda_{\mathrm{SPR}}$ around 700 nm to a -15.7 nm shift when $\Delta\lambda_{\mathrm{SPR}}$ is near 1150 nm (Table 4.1, columns 1 and 2). Over this range of $\Delta\lambda_{\mathrm{SPR}}$, the theoretical l_d, derived from solving Maxwell's equations, increases from ≈240 nm to ≈800 nm (Table 4.1, column 3). The calculated theoretical penetration depth depends on the source of optical constants for gold; complex permittivity values supplied by Johnson and Christy [176] gave estimates of greater penetration than did complex permittivity values included in the *Handbook of Optical Constants of Solids*[190]. Accounting for $\Delta\lambda_{\mathrm{SPR},\epsilon m}$ in the determination of l_d, yields a penetration depth estimate much closer to the theoretical values (Table 4.1,

columns 4 and 5) and an estimate that is much more consistent across the range of adlayer thickness studied (Table 4.1, column 6).

The small bias in comparison of theoretical l_d to empirically determined l_d (accounting for $\Delta\lambda_{\mathrm{SPR},\epsilon m}$) may occur from ϵ_m discrepancies in the literature and following thiol binding.[44, 69] Variation in ϵ_m present in literature [176, 190, 191] produces a deviation in l_d of 2-4% over the wavelength region investigated and there may be slight additional uncompensated ϵ_m variance, including the change due to thiol bonding. In comparison to surface plasmons on bare gold, surface plasmons supported on thiolated gold surfaces have an estimated 5% shallower theoretical l_d as calculated with a reduction in the imaginary component of ϵ_m proportional to the conductivity drop[192] observed by Zhang et. al.[184] Given these minimal inaccuracies in theoretical determination, it is argued that the empirical l_d is most reliably and accurately determined with the inclusion of $\Delta\lambda_{\mathrm{SPR},\epsilon m}$ relative to theory given that unreasonable values for l_d are obtained without inclusion of $\Delta\lambda_{\mathrm{SPR},\epsilon m}$ in the calculations.

Stability and accuracy in l_d calculations by equation (4.4) across multiple adlayer thicknesses remains superior even with consideration of worst-case error presented by the range of l_d determined when including the error in $\Delta\lambda_{\mathrm{SPR},\epsilon m}$ derived from linear regression statistics, $\pm s_{\Delta\lambda_{\mathrm{SPR},\epsilon m}}$ (Table 4.1, column 5). The intercept error introduces a 6% relative range in l_d calculated at $\Delta\lambda_{\mathrm{SPR},Au-S} = 767$ nm. Despite pessimistic error considerations, improved precision and accuracy are maintained for l_d estimates with $\Delta\lambda_{\mathrm{SPR},\epsilon m}$ as illustrated in comparing columns 5 and 6 in table 4.1.

If $\Delta\lambda_{\mathrm{SPR},\epsilon m}$ is not included in the calculations, l_d varies with 41-1089% RD across all thicknesses for $\Delta\lambda_{\mathrm{SPR},Au-S}$ values between 701 nm and 1152 nm. In contrast, by accounting for $\Delta\lambda_{\mathrm{SPR},\epsilon m}$, RD of l_d drastically decreases to 2% at $\Delta\lambda_{\mathrm{SPR},Au-S} = 767$ nm and 9-11% for all other wavelengths investigated. The greater deviation at $\Delta\lambda_{\mathrm{SPR},Au-S}$ values other than 767 nm is due to variance from changing the angle between samples. The data for $\Delta\lambda_{\mathrm{SPR},Au-S} = 767$ nm were collected without changing parameters on the NIR-SPR accessory between measurements. For the other measurements, $\Delta\lambda_{\mathrm{SPR}}$ was determined at multiple angles for each self-assembled monolayer in succession; thus

Table 4.1: Penetration depth calculated from experimental data with and without $\Delta\lambda_{\mathrm{SPR},\epsilon m}$ compared to theoretical determination

$\lambda_{\mathrm{SPR,Au\text{-}S}}$ (nm)	$\Delta\lambda_{\mathrm{SPR},\varepsilon m} \pm \sigma$ (nm)		With $\Delta\lambda_{\mathrm{SPR},\varepsilon m}$	With $\Delta\lambda_{\mathrm{SPR},\varepsilon m} \pm s_{\Delta\lambda\mathrm{SPR},\varepsilon m}$	Without $\Delta\lambda_{\mathrm{SPR},\varepsilon m}$
701.2	-5.3±1.8	$l_{d,\mathrm{exptl}}$	283±30	238 – 351	2967±4757
		Difference from $l_{d,\mathrm{theor}}$[a] =236 nm ...	20%	-49 – (-1)%	1160%
		Difference from $l_{d,\mathrm{theor}}$[b] =243 nm ...	16%	-45 – 2%	1123%
745.9	-5.5±1.6	$l_{d,\mathrm{exptl}}$	310±33	259 – 389	1001±662
		Difference from $l_{d,\mathrm{theor}}$[a] =292 nm ...	6%	-33 – 11%	243%
		Difference from $l_{d,\mathrm{theor}}$[b] =286 nm ...	8%	-36 – 9%	250%
766.8	-5.6±0.2	$l_{d,\mathrm{exptl}}$	368±6	357 – 378	1131±1852
		Difference from $l_{d,\mathrm{theor}}$[a] =317 nm ...	16%	-20 – (-13)%	257%
		Difference from $l_{d,\mathrm{theor}}$[b] =307 nm ...	20%	-23 – (-17)%	269%
813.4	-6.2±2.1	$l_{d,\mathrm{exptl}}$	383±35	326 – 468	985±513
		Difference from $l_{d,\mathrm{theor}}$[a] =373 nm ...	3%	-26 – 12%	164%
		Difference from $l_{d,\mathrm{theor}}$[b] =355 nm ...	8%	-32 – 8%	178%
930.6	-7.7±2.7	$l_{d,\mathrm{exptl}}$	537±60	451 – 668	1378±569
		Difference from $l_{d,\mathrm{theor}}$[a] =516 nm ...	4%	-29 – 13%	167%
		Difference from $l_{d,\mathrm{theor}}$[b] =489 nm ...	10%	-37 – 8%	182%
1019.0	-11.1±3.4	$l_{d,\mathrm{exptl}}$	682±66	576 – 845	8121±14430
		Difference from $l_{d,\mathrm{theor}}$[a] =632 nm ...	8%	-34 – 9%	1186%
		Difference from $l_{d,\mathrm{theor}}$[b] =599 nm ...	14%	-41 – 4%	1255%
1151.7	-15.7±2.7	$l_{d,\mathrm{exptl}}$	859±78	764 – 984	580±6311
		Difference from $l_{d,\mathrm{theor}}$[a] =839 nm ...	2%	-17 – 31%	31%
		Difference from $l_{d,\mathrm{theor}}$[b] =789 nm ...	9%	-25 – 27%	27%

Experimental values reported as $\bar{x} \pm \mathrm{s}$ determined from all thicknesses (Column 4 and 6) or a range of l_d calculated by including the error in $\Delta\lambda_{\mathrm{SPR},\epsilon m}$ ($s_{\Delta\lambda_{\mathrm{SPR},\epsilon m}}$) (Column 5) from all thicknesses. Theoretical values calculated with η_{Au} values from (a) *Handbook of Optical Constants of Solids*[190] and (b) Johnson and Christy[176].

random errors were introduced by slight irreproducibility in returning to the same angle between samples. Accordingly, the deviation may be further reduced by keeping the angle constant during measurement such as with $\Delta\lambda_{\mathrm{SPR},Au-S} = 767$ nm.

The ability to determine l_d from thin layers is important for characterization of l_d of surface plasmons in the near-IR, mid-IR and, potentially on other exotic materials or nanostructures. As the plasmonic resonance approaches the IR, both l_d and $\Delta\lambda_{\mathrm{SPR},\epsilon m}$ increase (Table 4.1), requiring thicker adlayers be applied to accurately employ the simplifying assumption that $\Delta\lambda_{\mathrm{SPR},\epsilon m} << \Delta\lambda_{\mathrm{SPR},\epsilon m}$. However, the adlayer must also be thin enough ($< 20\%$ l_d) to uphold the assumption of consistent l_d throughout the bilayer.[73] Additionally, surface functionalization of plasmonic conducting metal oxides, nanoparticles, and nanoparticle arrays will also result in a significant $\Delta\lambda_{\mathrm{SPR},\epsilon m}$. To our knowledge there has been no systematic study to determine the $\Delta\lambda_{\mathrm{SPR},\epsilon m}$ for these materials and provide recommendations for appropriate adlayers to accurately determine l_d. Hence, $\Delta\lambda_{\mathrm{SPR},\epsilon m}$ compensation may be used to provide a reliable representation of the l_d, regardless of adlayer thickness, due to proper isolation of the modeled response, $\Delta\lambda_{\mathrm{SPR},\epsilon s}$.

The superior performance of the empirical l_d determination method with $\Delta\lambda_{\mathrm{SPR},\epsilon s}$ compensation at small adsorbate thickness (relative to the l_d) is demonstrated in figure 4.5. The l_d calculated from the smallest thickness, MPA monolayer, by equations (4.3) and (4.4) are compared to values predicted from theory:[44]

$$l_d = \frac{\lambda}{2\pi}\frac{\sqrt{\epsilon'_m + \epsilon_s}}{\epsilon_s} \tag{4.5}$$

where ϵ'_m is the real component of ϵ_m and ϵ_{Au} values were obtained from *Handbook of Optical Constants of Solids*.[190] The λ_{SPR} is tuned by varying the incident angle of light from 63.1°to 68.3°. Generally, if $\Delta\lambda_{\mathrm{SPR},\epsilon m}$ is not accounted for in the calculations, unreasonable estimates of l_d are obtained (Figure 4.5, inset). For $\Delta\lambda_{\mathrm{SPR},Au-S} =$ 701-1152 nm, a difference from theory of 5-14% upon inclusion of $\Delta\lambda_{\mathrm{SPR},\epsilon m}$ (equation (4.4) represents a vast improvement over the 360-5557% difference for calculations not

including $\Delta\lambda_{\mathrm{SPR},\epsilon m}$ (equation (4.3). Calculation of l_d by equation (4.4) greatly outperforms equation (4.3) for small thicknesses necessary for nanostructure characterization.

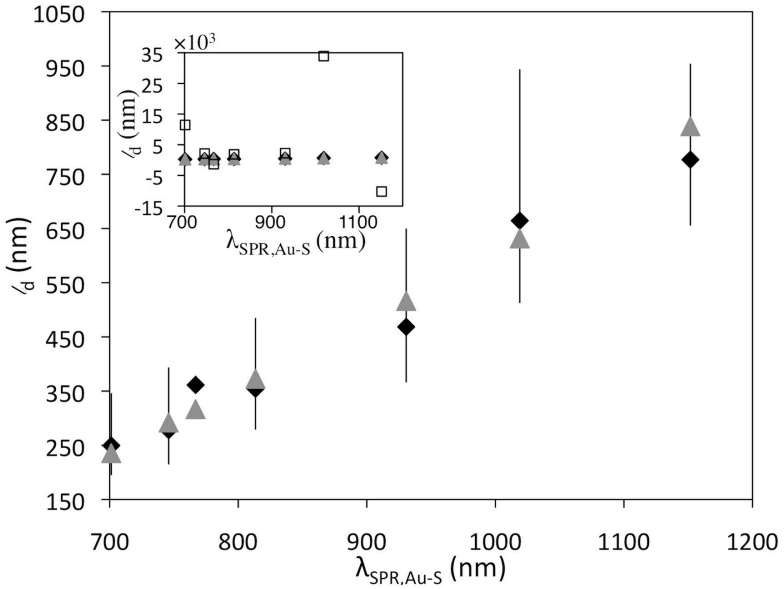

Figure 4.5: Experimental (♦) and theoretical (▲) l_d determined for d=0.828 nm at various wavelengths. Error bars represent experimental l_d range resulting from calculation with $\Delta\lambda_{\mathrm{SPR},\epsilon m}$ range of $(\Delta\lambda_{\mathrm{SPR},\epsilon m} - s_{\Delta\lambda_{\mathrm{SPR},\epsilon m}}, \Delta\lambda_{\mathrm{SPR},\epsilon m} + s_{\Delta\lambda_{\mathrm{SPR},\epsilon m}})$. Inset shows plot including the experimental l_d determined without the $\Delta\lambda_{\mathrm{SPR},\epsilon m}$ (□), which is out of range on the main plot.

Prediction of l_d for use under explicit experimental conditions should be performed with l_d calculation parameters chosen to parallel anticipated experimental parameters, particularly η_a, η_s, and excitation wavelength, given that each parameter affects the l_d. In addition to adjusting the wavelength for l_d measurements to the intended λ_{SPR} as shown above, RI and thickness of adsorbate should also be tailored to a range approximating the biorecognition element-sample of interest (e.g. linker-protein in PBS buffer). To demonstrate the method's capability, l_d was calculated from the shift obtained with various monolayers at 66.54° θ_{inc} in different bulk solutions of 0, 1.8, 3.5 and 5.3% w/w sucrose. Bulk sensitivity values used in the calculation are converted from λ_{SPR} of bare gold in each solution by a second order polynomial fit

to sensitivity (nm/RIU) as a function of λ_{SPR} (nm) (refer to section 3.3). The l_d in different solution RI was calculated; 368 ± 6 nm, 446 ± 6 nm, 458 ± 15 nm, and 429 ± 14 nm for η_s =1.333, 1.336, 1.338, and 1.341 solution, respectively, with a difference from theoretical predictions of 14%, 33%, 31% and 19%. As shown for variable η_s and λ_{SPR}, l_d may be effectively determined by this method for different experimental conditions.

4.4 Toward determination of penetration depth by PEM formation

SPR analysis of self-assembled PEM buildup may be used as a practical method for rapidly quantifying $\Delta\lambda_{\mathrm{SPR},\epsilon m}$ and l_d with high precision while requiring few sample substrates. These characteristics are particularly important for novel SPR surfaces that are costly or difficult to fabricate. Sequential buildup of PEMs, such as polyallylamine hydrochloride (PAH) / polystyrene sulfonate (PSS), offers linear thickness increase per layer on a single substrate. By contrast, changing layer thickness through controlling monolayer chain length requires several-hour SAM formation on many substrates, one per each monolayer. For example, the SPR shift for MPA and each PEM layer is measured as the difference following each rinsing step relative to the bare gold substrate, $\Delta\lambda_{\mathrm{SPR}} = 789.7$ nm, on a single substrate with 44 min elapsed per layer (Figure 4.6(a)). This time may be reduced to 1 minute per layer for adequate layer formation (refer to chapter 5). Thus, automated PEM buildup reduces sample numbers and time and enables a larger sample set of different thicknesses, improving the precision in $\Delta\lambda_{\mathrm{SPR},\epsilon m}$.

However, calculation of l_d requires precisely known adsorbate layer RI (η_a) and PEM layer RI values are not consistent in literature. The published range of PAH/PSS PEM η_a is unsuitably large to support accurate l_d determination. A change in wavelength through the near-infrared region[193] or variations in concentration of salt or polyelectrolyte in solution[194, 195] causes minimal change in PEM RI, yet the reported RIs of PAH/PSS layers vary between 1.34 and 2.0 RIU, with most values ranging between 1.4 and 1.5 RIU.[194, 196, 197, 198, 199] A more definitive RI, necessary for reliable l_d calculations based on PEM layers, may be determined by rearranging equation (4.6), where R=$\Delta\lambda_{\mathrm{SPR}}$, and utilizing the previously determined l_d values calculated

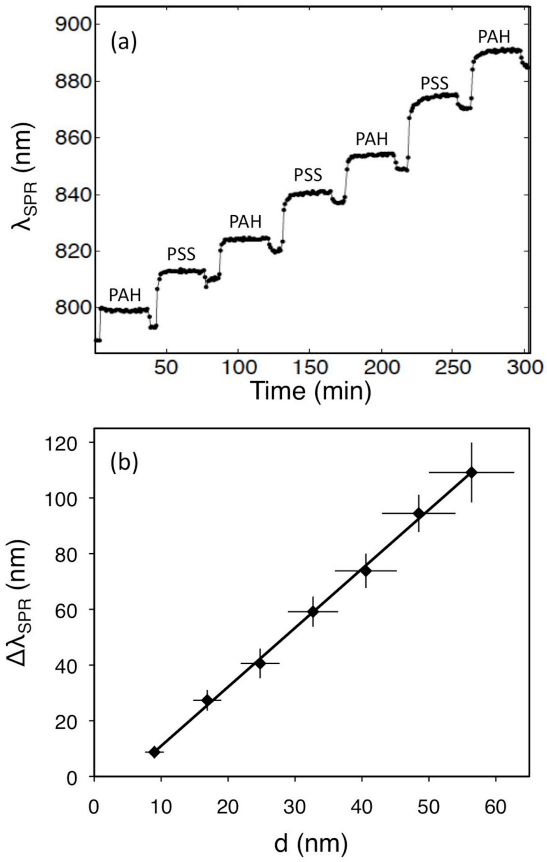

Figure 4.6: (a) Sensorgram for PEM buildup with NaCl rinse after each PEM layer. The straight line is provided as a visual aide. (b) $\Delta\lambda_{\mathrm{SPR}}$ with PEM thickness buildup. Vertical error bars correspond to the standard deviation in shift for N = 3. Horizontal error bars represent $\pm s_d$. Linear fit; m = 2.12±0.04, b = $\Delta\lambda_{\mathrm{SPR},\epsilon m}$ = -10.2±1.4, R^2 = 0.998.

from monolayer formation on the appropriate substrate:

$$\eta_a = \frac{\Delta\lambda_{\mathrm{SPR}} - \Delta\lambda_{\mathrm{SPR},\epsilon m}}{\mathrm{m}[1 - \exp(-2\mathrm{d}/\mathrm{l_d})]} + \eta_s \tag{4.6}$$

RI values calculated with $\Delta\lambda_{\mathrm{SPR},\epsilon m}$ are compared to RI values calculated without $\Delta\lambda_{\mathrm{SPR},\epsilon m}$ evaluated by a rearrangement of equation (4.3), where R = $\Delta\lambda_{\mathrm{SPR}}$:

$$\eta_a = \frac{\Delta\lambda_{\mathrm{SPR}}}{\mathrm{m}[1 - \exp(-2\mathrm{d}/\mathrm{l_d})]} + \eta_s \tag{4.7}$$

The MPA and PEM layers are treated as a homogeneous adsorbate layer due to similarity in RI 25 31, 33-36, hence $\eta_a = \eta_{\mathrm{PEM}}$ in equations (4.6) and (4.7).

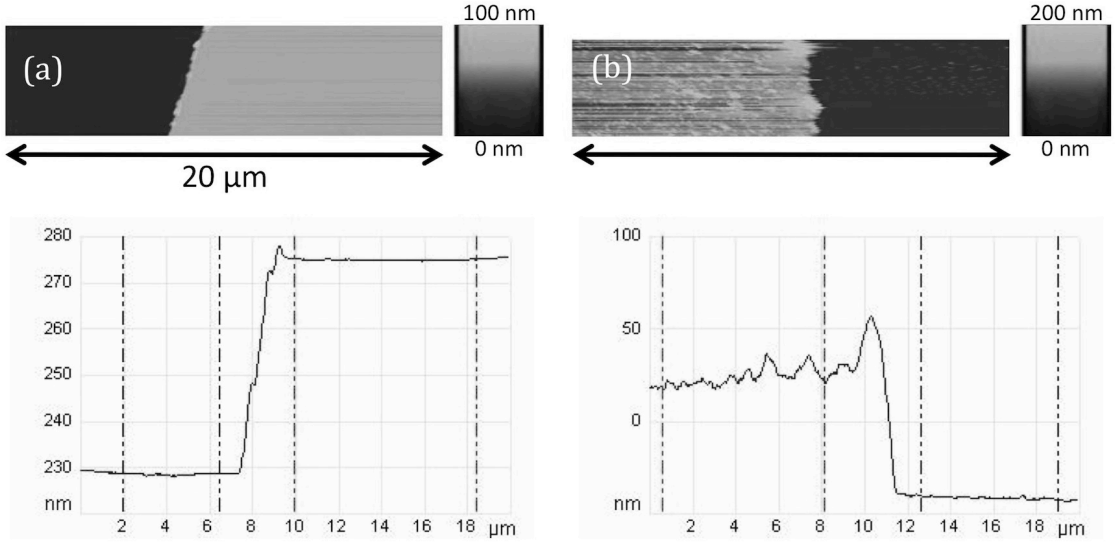

Figure 4.7: AFM images of (a) bare gold and (b) 3 PEM layers on gold. The profile images correspond to the average of the height across the y-axis of the image directly above them. Step height is determined by calculating the difference between the glass substrate (between black vertical lines) and sample (between red vertical lines).

The thickness of PEM layers used in estimation of η_{PEM} was measured by AFM and found to increase linearly with number of layers as demonstrated by the SPR spectroscopic data and supported by several sources in literature that indicate linear buildup. [196, 198, 200, 201] Although contrasting reports suggest PEM thickness may

initially increase exponentially with number of layers[202] or reach linear growth only after the fifth layer [194, 203], the measured SPR shift with layer number, η, exhibits linearity for layers 1-7 (Figure 4.8). Therefore, a linear fit of the thickness to layer numbers is a sound working foundation. The AFM thickness was measured for 1, 3, 5, and 7 layers to determine the trend and thickness with sequential layer buildup. Representative AFM images used to calculate step height of PEM layers are presented in figure 4.7. The gold thickness is subtracted from the PEM-gold height to determine PEM layer thickness. Weighted least squares regression was used to evaluate linear fit of thickness to layer thickness accounting for heteroscedascity (Figure 4.8).

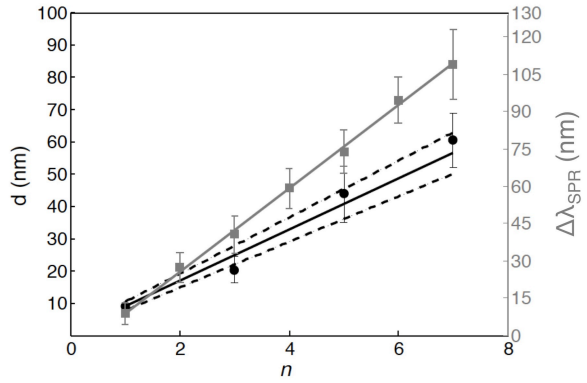

Figure 4.8: (left y-axis) AFM thickness, d, vs. number of PEM layers, n, (●) $\pm s_d$ intervals (- - -). Linear fit; $d = 7.9 \pm 0.9n + 1.1 \pm 1.1$, $R^2 = 0.979$. (right y-axis) $\Delta\lambda_{SPR}$ vs. number of PEM layers, n (■). Linear fit; $\Delta\lambda_{SPR} = 16.7 \pm 0.3n - 7.9 \pm 1.4$, $R^2 = 0.998$. Error bars represent standard error of the mean of N = 3 sample spots for thickness and N = 3 samples for $\Delta\lambda_{SPR}$.

Variation in PEM layer thickness based on average roughness of the PEM layers and spot-to-spot deviation calculated from AFM data is considered. Average roughness increases from 3.9 nm to 25 nm from layers 1 to 7; however, given that the roughness is substantially smaller than the l_d, field intensity changes within the scale of surface roughness are negligible. Accordingly, it may be treated as an average thickness perceived by the plasmonic field.[73] For structures where l_d approaches the same order

as the roughness, the height variation becomes significant, but may easily be circumvented by fabricating thinner PEM layers through varying salt concentration and pH to reach sub-nanometer layer thickness.[194, 204] For this analysis, 2-21% RSD variation calculated from three sections (15-20 μm width $\times$ 3-5 μm length) per sample is a more relevant assessment of uniform thickness than the roughness, and is incorporated within the error of the η_{PEM} calculation.

The η_{PEM} was determined from equations (4.6) and (4.7) utilizing $\Delta\lambda_{\mathrm{SPR},\epsilon m}$ calculated from the plot of $\Delta\lambda_{\mathrm{SPR}}$ vs. PEM thickness, $\Delta\lambda_{\mathrm{SPR},\epsilon m} = -10.2 \pm 1.4$ nm (Figure 4.6B). The η_{PEM} was then calculated by equations (4.6) and (4.7) with NaCl solution RI from Ladam et al.[194], bulk sensitivity of 8526 nm/RIU (refer to Figure 4.4 and section 3.3), and l_d from monolayer formation at $\Delta\lambda_{\mathrm{SPR,Au-S}} = 766.5$ nm (Figure 4.9). Despite the 13 nm difference in $\Delta\lambda_{\mathrm{SPR,Au-S}}$, the empirical l_d value at $\Delta\lambda_{\mathrm{SPR,Au-S}}$ = 766.5 nm is an acceptable value to use with PEM buildup at $\Delta\lambda_{\mathrm{SPR,Au-S}} = 779.5$ nm, because the l_d difference over this wavelength range is within experimental error. The theoretical l_d difference over $\Delta\lambda_{\mathrm{SPR,Au-S}}$ = 766.5-779.5 nm is 12 nm, whereas the error in empirical l_d is 21 nm (Table 4.1, column 5). In this manner, the η_{PEM} at $\Delta\lambda_{\mathrm{SPR,Au-S}}$ = 779.5 nm calculated at various PEM thicknesses with $\Delta\lambda_{\mathrm{SPR},\epsilon m}$ is 1.389 ± 0.002 RIU and without $\Delta\lambda_{\mathrm{SPR},\epsilon m}$ is 1.379 ± 0.009 RIU corresponding to RD of 0.2% and 0.7%, respectively.

The η_{PEM} computed with $\Delta\lambda_{\mathrm{SPR},\epsilon m}$ shows improved precision and better approximation of η_{PEM} determined with theoretical l_d as compared to η_{PEM} computed without $\Delta\lambda_{\mathrm{SPR},\epsilon m}$. The reproducibility of η_{PEM} calculated at different PEM thicknesses is not significantly worse for calculation without $\Delta\lambda_{\mathrm{SPR},\epsilon m}$, however, closer inspection of figure 4.9 reveals that the estimated η_{PEM} deviates with decreasing thicknesses. Parallel to figure 4.3, the error increases as $\Delta\lambda_{\mathrm{SPR},\epsilon s}$ approaches -$\Delta\lambda_{\mathrm{SPR},\epsilon m}$. Hence, the η_{PEM} by equation (4.6) exhibits much greater consistency across PEM layers translating to earlier convergence with η_{PEM} calculated from theoretical l_d. Both averaged values do exhibit a 0.37% difference from a η_{PEM} value of 1.384 RIU calculated with theoretically determined l_d from Maxwell's equations; however, these evaluations assume the proper

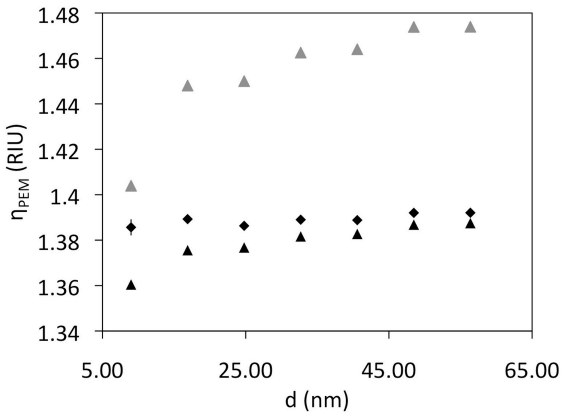

Figure 4.9: The η_{PEM} at varying PEM thickness calculated with (♦) and without (▲) $\Delta\lambda_{\mathrm{SPR},\epsilon m}$, by equations (4.6) and (4.7), respectively. A larger variation is established when η_{PEM} is calculated with l_d not corrected with $\Delta\lambda_{\mathrm{SPR},\epsilon m}$ (▲). Error bars on η_{PEM} calculated with $\Delta\lambda_{\mathrm{SPR},\epsilon m}$ represent range determined with $\Delta\lambda_{\mathrm{SPR},\epsilon m} \pm s_{\Delta\lambda_{\mathrm{SPR},\epsilon m}}$.

calculation of l_d including $\Delta\lambda_{\mathrm{SPR},\epsilon m}$. If η_{PEM} in equation (4.7) is calculated with l_d from monolayers with equation (4.3) rather than with equation (4.4), the difference from η_{PEM} with theoretical l_d increases to 5.0%. Thereby, the most reliable η_{PEM} value incorporates full consideration of $\Delta\lambda_{\mathrm{SPR},\epsilon m}$ and error including PEM thickness variation ($\mathrm{d} \pm \mathrm{s_d}$); 1.384-1.395 RIU. Together with this η_{PEM} value, SPR measurements of PEM buildup may be used to calculate a viable $\Delta\lambda_{\mathrm{SPR},\epsilon m}$ value, $\Delta\lambda_{\mathrm{SPR},\epsilon s}$ as a function of d, and consequently accurate plasmonic l_d on various surfaces.

4.5 Calculation of penetration depth of nanohole array surface plasmons

The presented method for including $\Delta\lambda_{\mathrm{SPR},\epsilon m}$ in l_d calculations has greater implications for nanostructured SPR substrates as compared to continuous gold due to their heightened bonding effects and reduced l_d (and consequently smaller d:l_d). To demonstrate the increased bonding effects and application of this method to nanostructured substrates, the penetration depth was calculated with and without $\Delta\lambda_{\mathrm{SPR},\epsilon m}$ for a nanohole array SPR substrate with diameter/periodicity= 0.29 and periodicity= 820 nm at λ_{SPR}= 883 nm (Figure 4.10). A 2750% improvement in RD for l_d calculated

with inclusion of $\Delta\lambda_{\mathrm{SPR},\epsilon m}$ was observed (8% RD for l_d calculated with $\Delta\lambda_{\mathrm{SPR},\epsilon m}$ compared to 220% RD for l_d calculated without $\Delta\lambda_{\mathrm{SPR},\epsilon m}$ across all thicknesses). The l_d for the nanohole array is 230 ± 31 nm considering $\Delta\lambda_{\mathrm{SPR},\epsilon m}$, which is a 37% decrease in l_d as compared to continuous gold under similar conditions. A greater d:l_d implies that smaller d is necessary in the analysis of nanostructures. Furthermore, the $\Delta\lambda_{\mathrm{SPR},\epsilon m} = -31.3 \pm 3.8$ nm for Au-S bond on the nanohole array is three times larger than the $\Delta\lambda_{\mathrm{SPR},\epsilon m}$ for Au-S bonding to continuous gold at $\lambda_{\mathrm{SPR}} = 883$ nm (-10.2 ± 1.4 nm), so the effects of not including $\Delta\lambda_{\mathrm{SPR},\epsilon m}$ is greater for nanostructures. It can be expected that $\Delta\lambda_{\mathrm{SPR},\epsilon m}$ will increase with wavelength similar to continuous gold. The increased $\Delta\lambda_{\mathrm{SPR},\epsilon m}$ and reduced l_d cause the consideration of $\Delta\lambda_{\mathrm{SPR},\epsilon m}$ to have even larger impact for nanohole array substrates than continuous gold.

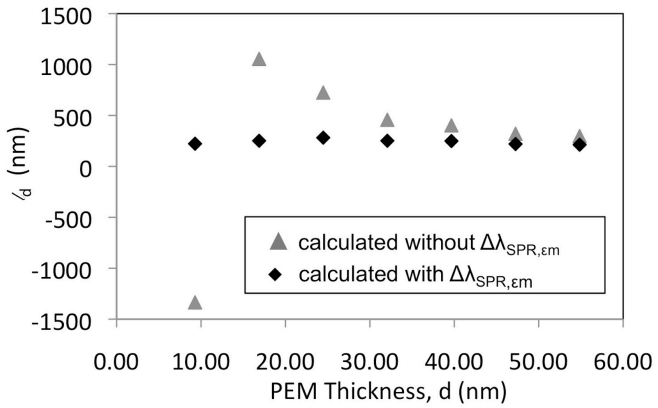

Figure 4.10: Nanohole array surface plasmon penetration depth calculated with and without $\Delta\lambda_{\mathrm{SPR},\epsilon m}$

4.6 Conclusion

The significance of including bonding effects on the permittivity of the supporting metal, $\Delta\lambda_{\mathrm{SPR},\epsilon m}$, in surface plasmon l_d determination was demonstrated over various wavelengths. Comparison of l_d values calculated with and without $\Delta\lambda_{\mathrm{SPR},\epsilon m}$ establishes increased accuracy and precision when $\Delta\lambda_{\mathrm{SPR},\epsilon m}$ is included and exhibits a particularly pronounced difference for smaller adsorbate thicknesses. This method

may be executed with a more empirically practical system of polyelectrolyte multilayers built on a single plasmonic sample and performed over ranging λ_{SPR}. Wavelength and condition specific l_d values can be used for determining the expected response to surface binding, structural parameters of adsorbate, and comparison of various sensor configurations and substrates. The precision and accuracy of these values is dictated by the statistical merit of the l_d value used in their calculation. Furthermore, the determination of l_d coupled with bulk sensitivity may facilitate selection of a more sensitive sensor construct where l_d matched to analyte size could maximize signal from adsorbate and minimize environmental noise.

Chapter 5

SENSITIVITY OF NANOHOLE ARRAY NEAR INFRARED-SURFACE PLASMON RESONANCE SPECTROSCOPY

5.1 Introduction

Surface plasmon resonance (SPR) spectroscopy can detect low concentrations of nanoscale analytes, such as proteins, for use in various biosensing applications. The advantage of this technique is high surface sensitivity arising from the evanescent nature of the surface plasmon extending from the sensor-sample interface. Current detection limits correspond to diagnostic protein concentration levels [76], but capabilities could improve from increased sensitivity with the ability to discriminate small changes in concentration, detection of proteins with poor binding affinity to biorecognition elements, and detection of even lower concentration biomarkers.[44, 45, 6, 7] Nanostructuring SPR substrates may increase SPR sensitivity, thus biosensors based on plasmonic nanostructures have been widely investigated.[52, 53, 43] The surface sensitivity of several nanostructured SPR biosensors has been compared to thin film SPR biosensors and nanohole arrays [55] have shown a marked improvement in surface sensitivity compared to continuous gold films. However, little difference from continuous gold thin films was observed for nanotriangles [56], nanodisks [57], and nanorods [58].

Surface plasmon resonance active nanohole arrays have demonstrated increased biosensing capability over conventional continuous gold films[55, 54], and have other applications in surface enhanced Raman spectroscopy [127, 128], optoelectronics [133], and waveguiding [17, 18]. This chapter intends to primarily investigate the sensing properties of SPR on nanohole arrays in the near infrared, yet the fundamental surface plasmon (SP) characterization may provide insight into other applications as well. The sensing capability of nanohole arrays arises from SP sensitivity to adsorbates adhering

to nanohole array substrates within the shallow penetration depth (l_d) region of the SP, i.e. the depth at which the SP electric field intensity decays to 1/e (Figure 5.1). These structures support several SP modes (refer to chapter 2). The various plasmon modes are excited within the holes (LSPR), between the neighboring holes (Bragg SPs), and within the semi-continuous regions between rows of holes (propagating SPs), and these modes exhibit variable sensitivity to adsorbate binding.[126, 138, 144, 205, 142] Furthermore, the SP modes can be excited in different optical modes, namely transmission and Kretschmann configuration (Figure 5.1); however, sensing with the propagating SP in Kretschmann mode has exhibited greater sensitivity than sensing with the Bragg SPs in transmission mode[55] and this configuration allows real-time measurements in highly scattering samples, such as biological fluids.

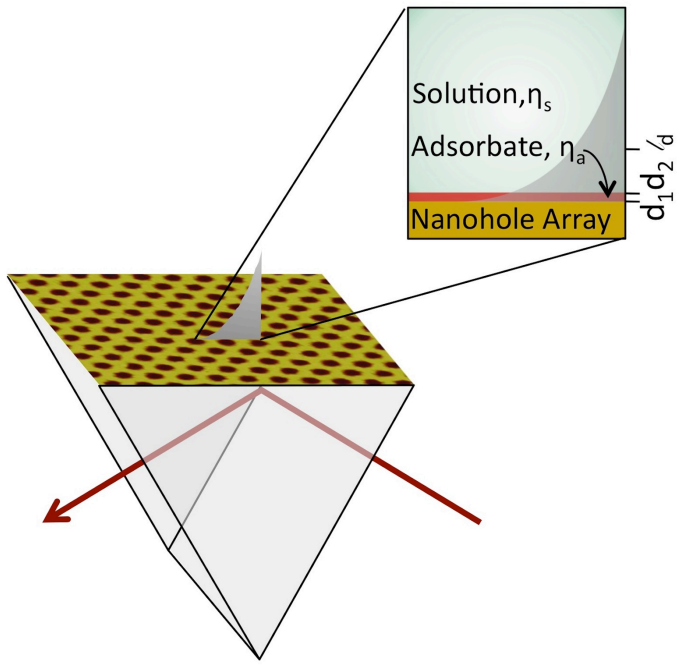

Figure 5.1: Diagram of nanohole array in Kretschmann configuration with adsorbate volume (d_1 to d_2) and sensing volume (gold interface to l_d) illustrated. The refractive index (RI) sensed by the plasmonic field is an effective RI composed of the adsorbate RI (η_a) and bulk RI (η_s).

Nanohole array SPs may be tailored to control field enhancement regions, sensitivity, and interaction between coexcited SPs, which may increase sensitivity.[100, 115] The SPR conditions depend on the physical parameters of the nanohole array, translating to tunability of the Bragg surface plasmons with nanohole array structure (refer to chapter 2).[140, 141] Additionally, SPR sensitivity changes with excitation wavelength (λ_{SPR}).[48, 45, 125] In this manner, measurements with λ_{SPR} in the near infrared (NIR) exhibit greater bulk sensitivity than the conventionally used visible region. [45, 48, 125, 49] However, sensitivity to bulk RI changes throughout the entire plasmonic field, i.e. bulk sensitivity, does not exactly translate to surface sensitivity. The working principle of SPR sensing is sensitivity to near surface interactions, so it is the surface sensitivity to bound analyte that is of particular interest. High surface sensitivity is achieved when a greater proportion of the sensing volume is occupied by the adsorbate layer rather than the bulk solution.[73] Furthermore, it is optimal to nearly fill the sensing volume with the analyte in order to preclude contributions from bulk environmental RI fluctuation. Consequently, sensitivity to RI changes within the thin analyte adsorption layer (surface sensitivity) is more informative of sensor performance than is the sensitivity to RI changes throughout the entire plasmonic field (bulk sensitivity).

Maximal surface sensitivity and selectivity against bulk effects is achieved when the analyte occupies the majority of the sensing volume. The surface sensitivity, $\mathrm{m_{surf}}$, to an analyte of specific volume, V_a, residing within the sensing volume, V_s, may be calculated by;

$$\mathrm{m_{surf}} = \mathrm{m}\frac{V_a}{V_s} = \mathrm{m}\frac{\exp\left(-2\mathrm{d}_2/l_d\right) - \exp\left(-2\mathrm{d}_1/l_d\right)}{\exp(-2) - 1} \tag{5.1}$$

where m is the bulk sensitivity. For full surface coverage, V_a/V_s may be calculated by integrating over the respective distances within the exponentially decaying plasmonic field (Figure 5.1). The sensing volume, V_s, extends from the gold surface (d=0 nm) to the penetration depth (d=l_d). The analyte volume spans from the binding distance

($d=d_1$) to the top of the th bound analyte ($d=d_2$). By evaluating the m_{surf} merit for a specific analyte thickness, sensing parameters may be optimized. Another figure of merit for sensor capability is resolution, which depends on system noise and SPR peak sharpness, represented by peak height/full width at half maximum (FWHM). Similar peak height/FWHM has been previously observed between nanohole arrays and continuous gold in the visible region.[55, 54], thereby this contribution focuses on analysis of surface sensitivity and contributing factors.

The surface sensitivity depends on V_a/V_s and bulk sensitivity, so factors which contribute to these terms affect the sensing capability and should be optimized. The SP penetration depth directly affects the sensing volume and may be tailored to specific analyte sizes [182, 183], and it controls the region of field enhancement for surface and tip enhanced spectroscopic techniques. Both penetration depth and bulk sensitivity depend on SPR wavelength. As a result, surface sensitivity may be optimized by tuning SPR wavelength and penetration depth. In addition to changing wavelength, the use of different nanostructured sensing substrates offers variable SP characteristics.[206] This chapter presents the characterization and optimization of various nanohole array parameters and is the first study to our knowledge of nanohole arrays in Kretschmann configuration in the NIR region.

5.2 Experimental methods

5.2.1 SPR spectroscopy measurements

Spectroscopic measurements were acquired on a Bruker Optics (Billerica, MA) Vertex 70 FTIR spectrometer with an IR-SPR accessory based on a NIR-SPR accessory as previously described in chapter 3 and section 4.2.1. A constant angle setup was used in which the response was measured as a shift in wavelength ($\Delta\lambda_{SPR}$) at a fixed angle. The λ_{SPR} is determined by fitting a second order polynomial to SPR dip and solving for the zero of the derivative of the curve. The shift in wavelength is relative to λ_{SPR} for the bare, non-functionalized substrate in water.

5.2.2 Gold nanohole array sensor surface preparation

Rectangular glass coverslips (Electron Microscopy Sciences, Ft. Washington, PA, 10.5×35 mm) were cleaned by immersion in boiling piranha solution (3:1 (v/v) concentrated H_2SO_4: 30% H_2O_2) (Fisher Scientific, Fair Lawn, NJ) for at least one hour and triplicate rinsing and sonication in deionized water for one minute. The slides were sonicated in a 5:1:1 (v/v) mixture of water, hydrogen peroxide, and ammonium hydroxide followed by washing with deionized water. The nanosphere lithography procedure from section 2.3 was utilized to produce a set of nanohole array substrates with varying periodicity and diameter. Samples were kept under vacuum prior to metallization until use.

5.2.3 Sensitivity measurements

Bulk sensitivity ($m = \Delta\lambda_{SPR}/\Delta\eta$) was calculated from response to RI calibration standards of varying sucrose ($\geq$ 99.5%, Sigma-Aldrich, St. Louis, MO) concentrations ($0 - 3\%$) according to the procedure outlined in section 4.2.3. Triplicate samples were measured for each nanohole array set. For each sample, λ_{SPR} was measured in air at every angle, then for the series of sucrose solutions at each angle before proceeding to the next angle ($\theta_{inc} = 61.85 - 64.32°$).

Surface sensitivity was calculated by equation 5.1 with values for bulk sensitivity calculated as detailed above, adsorbate thickness set to match desired analyte, and penetration depth evaluated as follows. Penetration depth was calculated from response to sequential buildup of known thicknesses of polyelectrolyte multilayers (PEM) of polyallylamine hydrochloride (PAH) and polystyrene sulfonate (PSS). A detailed procedure is presented in section 4 with the folloing changes to the procedure; the PEM solutions were prepared in deionized water and solutions were allowed to rest and form adlayers for one minute before exchange with 2 mL aliquots. This was sufficient to fully replace the solution within the flow cell (0.0048 in^3 volume). In some cases, triplicate samples were not available, rather, a third trial was attained by duplicate measurement of a sample after it was oxygen etched for one hour. The variation in the bare surface SPR

wavelength between the sample before and after etching was within experimental error. Thereby, this duplicate sample measurement serves as a reliable replicate measurement.

5.2.4 Atomic force microscopy

The physical parameters of the nanohole array substrates were determined by atomic force microscopy with a Nanoscope IV AFM (Bruker AXS, Santa Barbara, CA). A silicon TAP-300-G probe (Innovative Solutions Bulgaria Ltd., Sofia, Bulgaria) was used in tapping mode in air. For each nanohole array set, three spots on three separate samples were evaluated. A 5×5 μm^2 image was acquired and analyzed with Nanoscope software.

5.3 Physical characterization

Sets of nanohole arrays with various diameter and periodicity were fabricated and analyzed by AFM to determine the height, diameter and periodicity. To investigate effects of periodicity and diameter, sets of various periodicity (490-3000 nm) with same diameter to periodicity ratio (D/P) (0.36 ± 0.02) and sets of various D/P (0.27-0.44) with same periodicity (820 nm) were fabricated (refer to Figure 5.2). The diameter varied between nearest sets by 40-56%. Considering the variation in D/P (standard deviation of $0.01 - 0.03$), the sets remain statistically different with 95% confidence ($t_{calc} = 2.9 - 3.8$ where $t_{table} = 2.78$). The gold was 78 ± 5 nm thick.

5.4 Nanohole array SPR features

Various surface plasmons on the nanohole arrays may be excited in the NIR and are easily visualized in different dielectric media. Fundamental characterization of the SPs provides insight for improving field enhanced spectroscopy and SPR spectroscopy sensitivity. Understanding the SP features is important to full exploitation of their interaction, tunability, and subsequent application. With the nanohole array in air, Bragg SPs of various resonance orders are observed as shallow SPR dips (Figure 5.3). At incident angles between 61.8-64.3° in water, the SPR dip arising from the propagating plasmon overwhelms the shallower Bragg SPs and obscures it from view (Figure

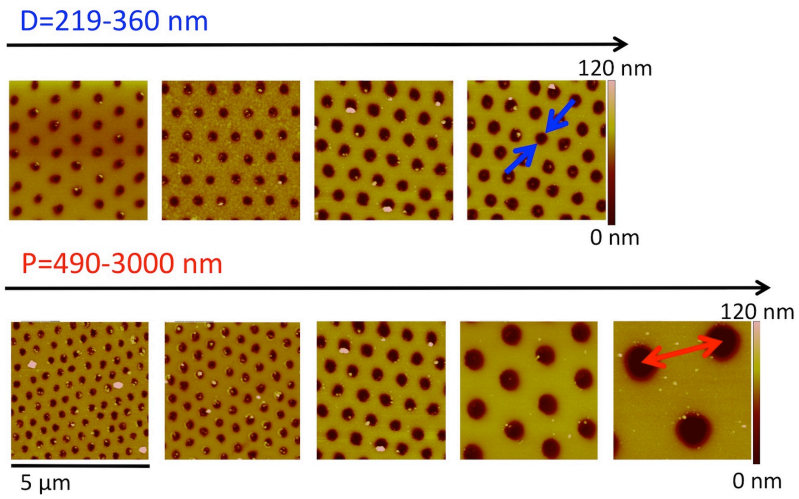

Figure 5.2: AFM images of nanohole arrays with various diameter (D) and periodicity (P).

5.3), however they are still prevalent. The Bragg SP λ_{SPR} generally shifts minimally with change in sample RI and incident angle. Some of the SPR dips arise from Bragg SPs on the nanohole array-prism interface, therefore a change in sample RI on the topside does not affect these specific SPR features. Conversely, some Bragg SPs are supported on the nanohole array-sample interface and exhibit a range of sensitivities to sample RI. These Bragg SPs may be used for sensing purposes and interaction with propagating SPs.[100, 115, 122]

Features which demonstrate sensitivity to changes in sample refractive index and may affect SPR sensing are highlighted in figure 5.4(b). These Bragg SPs were assessed in various sample media by SPR spectroscopy at higher incident angles, where the propagating SP is blue shifted out of the measured range to allow evaluation of otherwise obscured Bragg SPs. In this manner, measurements at θ_{inc}=69.9° established the RI sensitivity of the Bragg SPs from a change in water to air (Figure 5.5(b)). The sensitivities are presented in table 5.1.

The λ_{SPR} of Bragg SPs is primarily periodicity dependent (refer to equation (2.5)), so it may be tuned by changing the nanohole periodicity. Contrastingly, nanohole

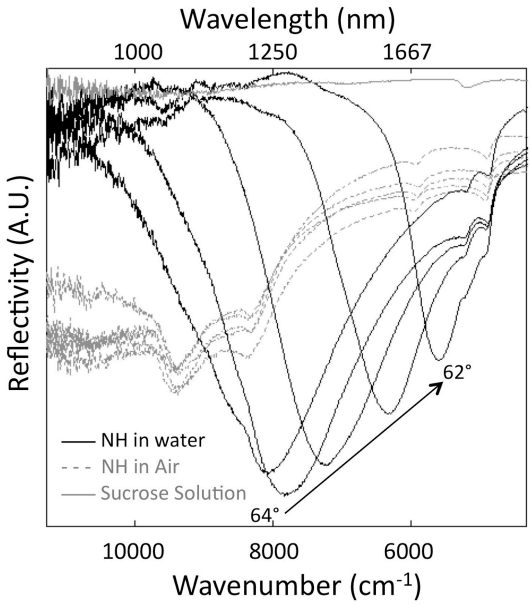

Figure 5.3: Representative nanohole array SPR spectra ($\theta_{inc} = 64-62°$) demonstrating Bragg SPs (in air) and propagating SPs (in water). A spectrum of sucrose is included to visualize potentially convoluting absorptions from the analyte.

diameter has little affect on λ_{SPR} of Bragg SPs. For example, for varying D/P (0.27 to 0.44) and P=820 nm, the Bragg SPs are consistently excited in air at λ_{SPR}=1050, 1250, 1695, and 2040 nm with little variation (standard deviation <20 nm) (Figure 5.4(a)). Additionally, there is negligible change in the Bragg SP λ_{SPR} with angle (61.8°<θ_{inc} <64.3°). For changing periodicity (490-3000 nm) and same D/P, the Bragg SP features vary greatly. The lower periodicity nanohole arrays (P=490-820 nm) exhibit several sharp features at different wavelengths (Figure 5.4(b)), whereas the larger periodicity (P=1500 nm and 3000 nm) structures exhibit broad features.

Theoretical Bragg SP λ_{SPR} values were calculated for various Bragg resonance orders with consideration for the angle between the incident light vector and x-axis of the nanohole array reciprocal lattice, i.e. the azimuthal angle (ϕ) (Figure 5.5 and 5.6). A more accurate model of the Bragg SP λ_{SPR} which accounts for the azimuthal angle has recently been developed by Masson et. al. [164], refer to equation (2.5). Analysis

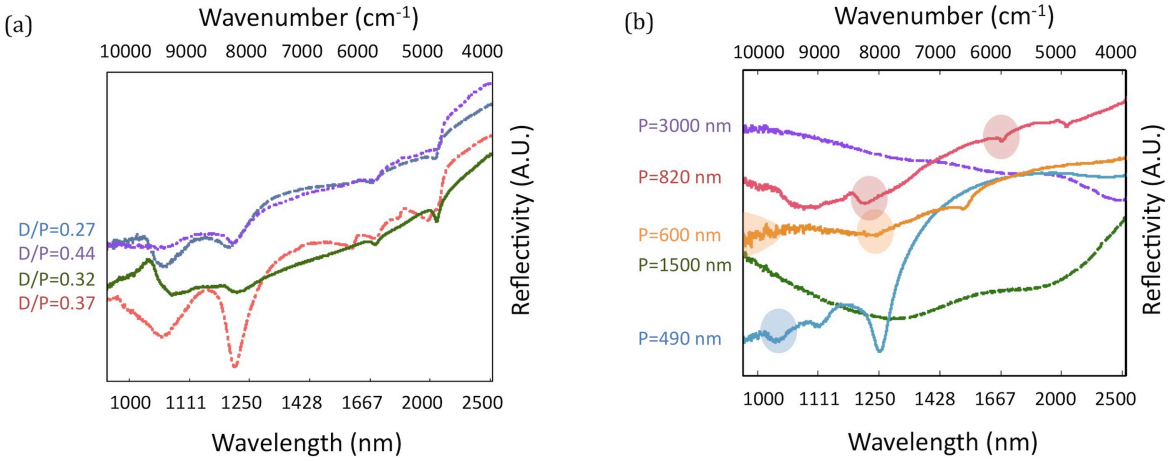

Figure 5.4: Nanohole array SPR spectra in air demonstrating Bragg SPs for various nanohole (a) D/P and (b) P. Bragg SPs that demonstrate sensitivity to sample refractive index are highlighted in (b).

of the features within the first $\phi = 30°$ represents the possible Bragg SP λ_{SPR}'s for the low Bragg resonance orders (as pictured in figure 5.5 and 5.6). The modeled Bragg SP λ_{SPR} are displayed for $\phi = 0 - 60°$, because the features repeat symmetrically every 60°. Furthermore, each $\Delta\phi = 30°$, the features are reflected, so the Bragg SP λ_{SPR} are considered for $\phi = 0 - 30°$. The Bragg SP λ_{SPR}'s fluctuate moderately over this ϕ range, therefore Bragg SP features are proportionally broadened for measurement of an area including several azimuthal orientations of the nanohole array. In this case, the nanohole arrays are continuous without dislocations or grain boundaries for approximately 20 μm^2 area (Table 2.2), and the spot size is approximately 4 mm^2. Therefore, a single SPR spectrum collected with this setup is representative of several nanohole array orientations. The experimental features are expected to be broader than measurements of an area with a smaller range in azimuthal orientation. Also, there are some modeled values for P=1500 nm which do not follow the curve and may be disregarded. They result from the wavelength dropping below the boundaries of the model (700-2300 nm), which returns erroneous λ_{SPR} calculations.

For each Bragg SP observed in the experimental spectra there is a corresponding theoretical Bragg SP at a given interfacing medium (glass or sample) (Figure 5.6). In

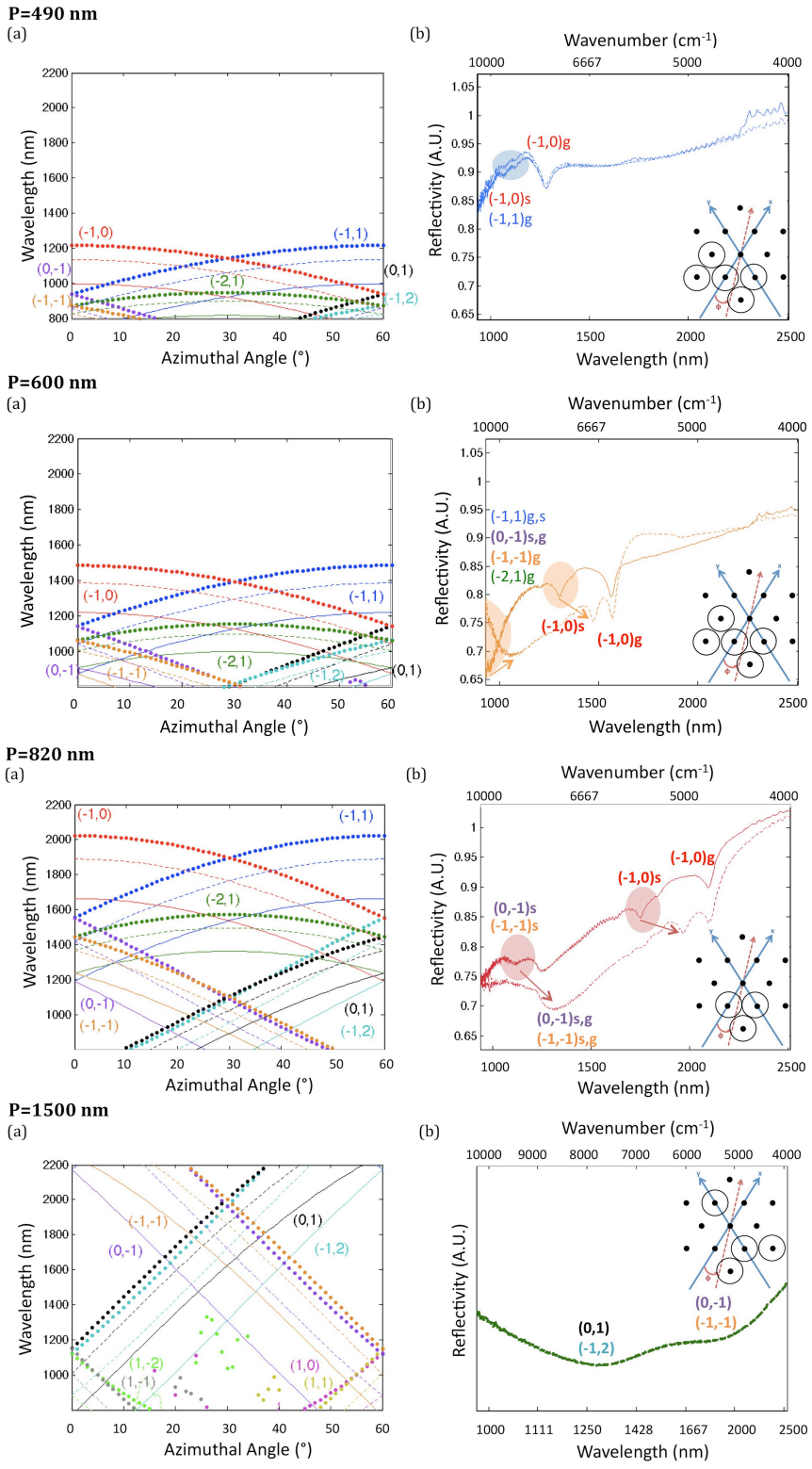

Figure 5.5: Bragg SPs supported on various periodicity nanohole arrays; (a) Theoretical λ_{SPR} vs. ϕ for glass (···), water (- - -), and air (—) and (b) experimental spectra in water (- - -), and air (—). Bragg resonance orders are labeled with the interfacing medium (sample (s) or glass (g)) in (b), and inset figure illustrates the reciprocal space nanohole array lattice with the excited orders circled.

general, the experimental λ_{SPR} are approximately 80-100 nm red shifted from the modeled λ_{SPR}, most likely due to both differences in complex permittivity values and lack of accounting for SP interaction. Accounting for this difference, modeling indicates the Bragg resonance orders (relative to ϕ) of the experimental SPR features. There are several patterns which substantiate the Bragg resonance order designations. Similar Bragg resonance orders are excited for various periodicity nanohole arrays with a red shifting of each Bragg SP feature with increasing periodicity. The resonance orders closest to the incident light vector are excited more intensely, meaning they appear as sharper peaks in spectra, and the λ_{SPR} for these orders varies less with ϕ than those further away. Also, the Bragg SPs excited on the sample side exhibit change with measurement in water vs. air.

Accordingly, the spectral features are labeled by their respective Bragg resonance orders. A relatively sharp feature arising from the (-1,0) resonance order is measured for the lower periodicity arrays. This corresponds to the resonance order most closely aligned with the incident light vector for the investigated ϕ range (0-30°). The Bragg SPs from the next nearest lattice orders in the direction of the azimuthal rotation, (0,-1) and (-1,-1), prominently appear in the spectra as well. The experimental peaks for P=600 nm and P=490 nm that coincide with Bragg SPs from (-1,1) and (-2,1) lack consistency across different periodicity nanohole arrays, therefore these designations are solely inferred from wavelength matching. Furthermore, these peaks coincide with λ_{SPR} from orders that are closer to the incident light vector as well, which suggests they may rather result from these other resonance orders. The Bragg SPs from lattice orders excluding (-1,0) may be excited at overlapping wavelengths and manifest as composite features (apparent in figure 5.5 at lower wavelengths than the (-1,0) peak). Spectrally, they appear as broader peaks that slightly shift and broaden with sample change. As demonstrated for P=1500 nm, features exist at lower wavelengths which correspond to Bragg SPs from orders further from the incident light vector axis, (-1,2) and (0,-1), and the Bragg SP peaks are generally broader for higher periodicity due to large $\Delta\lambda_{SPR}$ with ϕ.

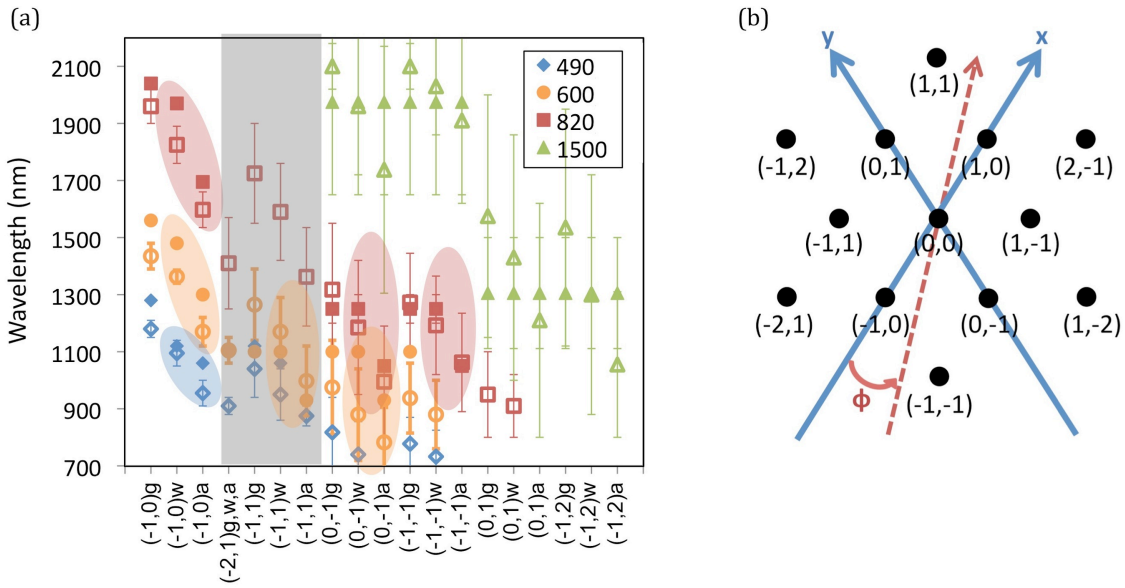

Figure 5.6: (a) Theoretical (open markers) and experimental (filled markers) Bragg SP λ_{SPR} for various periodicity nanohole arrays ($\sim$ nm), Bragg resonance orders, and interfacing dielectric (glass (g), water (w), and air (a)). Error bars represent the SPR peak width (FWHM) determined from theoretical variation in λ_{SPR} with $\phi = 0 - 30°$or experimental FWHM and the gray band designates features which are not consistent across different periodicity nanohole arrays and may result from different resonance orders. Bragg SPs that exhibit measured RI sensitivity are highlighted. (b) Reciprocal space nanohole array lattice illustrating Bragg resonance orders and azimuthal angle, ϕ.

Many of the Bragg SPs are sample sensitive; however, the propagating SPs are more sensitive than these Bragg SPs by over an order of magnitude. Table 5.1 presents the RI sensitivity of the Bragg SPs. The theoretical values have been included for comparison, but the sensitivities are not consistent in every case. This is most likely due to sample inhomogeneity and a lack of accounting for SP interactions, gold thickness, hole diameter, and surface roughness in the model. The propagating SP may interact with the Bragg SPs which increases sensitivity and excitation wavelength. This interaction and the Bragg SPs affect the spectral profile and understanding of the nanohole array plasmonics, but the main focus of the sensitivity assessment are the propagating SPs. Hence, the $\Delta\lambda_{SPR}$ of the propagating SPs is measured in the forthcoming studies. For specific conditions, the Bragg SP features may convolute the propagating SP. In this case, the λ_{SPR} is determined by fitting a second order polynomial to the broader propagating SPR dip with the Bragg SP region removed. Absorptions from the analyte are not of concern for potential convolutions, because the sucrose solutions utilized in bulk sensitivity calibration show minimal absorptions within the NIR region investigated (Figure 5.3). The following studies evaluate the sensitivity of the propagating SPs with consideration of Bragg SP effects.

Table 5.1: Theoretical and experimental sensitivity of sample sensitive Bragg SPs supported on various periodicity nanohole arrays. Bragg SP resonance orders which are not consistent across different periodicity nanohole arrays and may result from different resonance orders are represented in grey.

Periodicity (nm)	Bragg Resonance Order	λ_{SPR} in Air (nm)		λ_{SPR} in Water (nm)		Bulk Sensitivity (nm/RIU)	
		Exptl.	Theor.	Exptl.	Theor.	Exptl.	Theor.
490	(-1,0)	1060	955	1120	1095	180	425
600	(-1,0)	1300	1170	1480	1363	545	585
600	(-1,1), (0,-1)	930	998, 783	1100	1170, 880	515	521, 294
820	(-1,0)	1695	1598	1970	1825	830	690
820	(0,-1), (-1,-1)	1050	995, 1063	1260	1185, 1195	640	580, 400

5.5 Bulk sensitivity

The bulk sensitivity (m) of the nanohole arrays depends on the λ_{SPR} and the physical parameters of the nanohole array (diameter, thickness, and periodicity). By manipulating the experimental parameters, the bulk sensitivity may be tuned and optimized. The bulk sensitivity for various D/P and P is investigated throughout the near-infrared and compared to conventional continuous gold. The gold thickness is kept consistent for the nanohole array substrates (78 ± 5 nm), and the thickness of the continuous gold samples is 50 ± 2 nm. The λ_{SPR} is controlled by changing the angle of incidence (θ_{inc}) and increases as incident angle decreases from 64.3-61.8°.

The bulk sensitivity of nanohole arrays deviates from the angle dependent behavior of continuous gold as D/P is increased. Figure 5.7(a) demonstrates the deviation from the bulk sensitivity profile of continuous gold as D/P increases. The local maximum in bulk sensitivity occurs at θ_{inc}=62.5° for D/P=0 to 0.32 (where D/P=0 represents continuous gold) and deviates to higher incident angles for larger D/P ((θ_{inc}= 63.1° and 62.8° for D/P=0.37 and 0.44, respectively). As the hole size increases, the nanohole array deviates from behavior of continuous gold. The different sensitivity-angle profiles arise from a change in λ_{SPR} at a given θ_{inc}. The λ_{SPR} increases with D/P as demonstrated in figure 5.7(b). The peak bulk sensitivity aligns with the same λ_{SPR} for each nanohole array (1634 ± 31 nm), whereas the peak bulk sensitivity for continuous gold occurs at $\lambda_{SPR} = 1412 \pm 12$nm. The maximum bulk sensitivity of the nanohole array substrates (P=820 nm) occurs at a different λ_{SPR} than for continuous gold substrates and the λ_{SPR} red-shifts with D/P, indicating effects of the nanohole array structures and possible interactions with Bragg SPs.

The λ_{SPR} for maximum bulk sensitivity lies between two sample sensitive Bragg SP λ_{SPR} which may affect the propagating SP (Figure 5.7(b)). These Bragg SPs appear at λ_{SPR} of 1970 nm and 1260 nm in water and are sensitive to sample refractive index, whereas the other Bragg plasmon (within the 900-2200 nm range) is not sensitive (depicted as grey dashed line in figure 5.7(b)). The refractive index sensitivity of Bragg SPs indicates excitation at the nanohole array-sample interface and supports

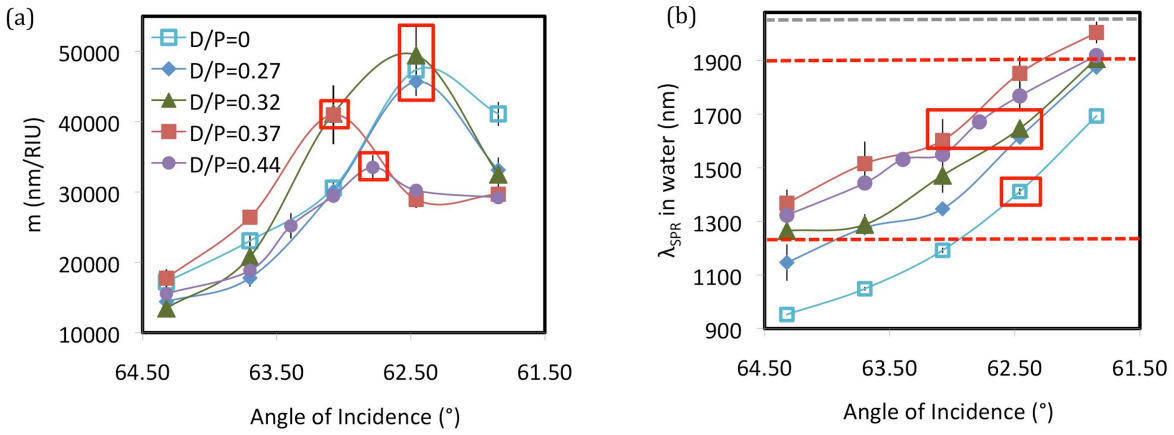

Figure 5.7: (a) Bulk sensitivity and (b) λ_{SPR} of various diameter nanohole arrays (P=820 nm) as a function of incident angle. D/P=0 nm represents continuous gold. The points of maximum bulk sensitivity for each sample are outlined and the λ_{SPR} of the Bragg SPs are represented by dashed lines.

the potential for coupling to the propagating SP on the same nanohole array interface. Coupling has been observed for nanohole arrays [100] and nanovoid arrays [147] in the visible range when the propagating λ_{SPR} is approximately coincident with or 100 nm redshifted from the Bragg λ_{SPR}. Coexcitation of propagating and Bragg SPs on the nanohole array-sample interface at similar NIR wavelengths may lead to coupled SPs and increased bulk sensitivity. Effectively, the difference in excitation wavelength for maximum sensitivity between continuous gold and nanohole array substrates may be a combination of coupling between the Bragg SPs and propagating SP, gold thickness effects[44, 69], and comparatively red-shifted λ_{SPR}.

The dependence of the λ_{SPR} position for maximum sensitivity on sensor structure is further illustrated by the offset wavelength-sensitivity profiles of continuous gold vs. nanohole array in figure 5.8. The λ_{SPR} for maximum sensitivity with the nanohole array remains consistent for all D/P and lies between the λ_{SPR} of the sample sensitive Bragg SPs (represented as bold dashed lines) in figure 5.8. The λ_{SPR} for maximum bulk sensitivity is unchanging for the P=820 nm nanohole arrays, however the bulk sensitivity value decreases with decreasing D/P.

The magnitude and wavelength of maximal bulk sensitivity also depends on

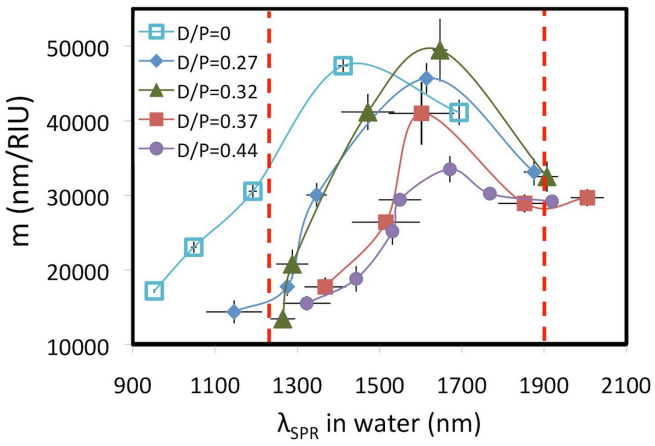

Figure 5.8: Bulk sensitivity of various diameter nanohole arrays (P=820 nm) as a function of λ_{SPR}. D/P=0 nm represents continuous gold. The λ_{SPR} of the sample sensitive Bragg SPs are represented by red dashed lines.

the periodicity of nanohole arrays. The bulk sensitivity peaks at a different incident angle and wavelength for various periodicity nanohole arrays (Figure 5.9), most likely due to effects from the sample sensitive Bragg SP λ_{SPR} if within range (highlighted in figure 5.9(b)) and variable λ_{SPR}. For P=600 nm, maximum bulk sensitivity occurs at $\lambda_{SPR} = 1542 \pm 43$ nm, which is 60 nm red shifted from a sample sensitive Bragg SP at λ_{SPR}=1480 nm. The P=490 nm nanohole arrays do not support any sample sensitive Bragg SPs within the wavelength range investigated. The nearest Bragg SP is excited at $\lambda_{SPR} = 1115$ nm. Consequently, its bulk sensitivity profile reflected that of continuous gold (Figure 5.9(a)) with an offset in wavelength. The larger periodicity (P=1500 nm and 3000 nm) structures exhibit broad Bragg SP features that severely convolute the propagating SP of interest; therefore, analysis across the entire angle region was impeded and the sensitivity for these structures was not fully investigated. The λ_{SPR} position for maximum sensitivity depends on the periodicity and only deviated from continuous gold when Bragg SPs are present, suggesting tunability and SP coupling.

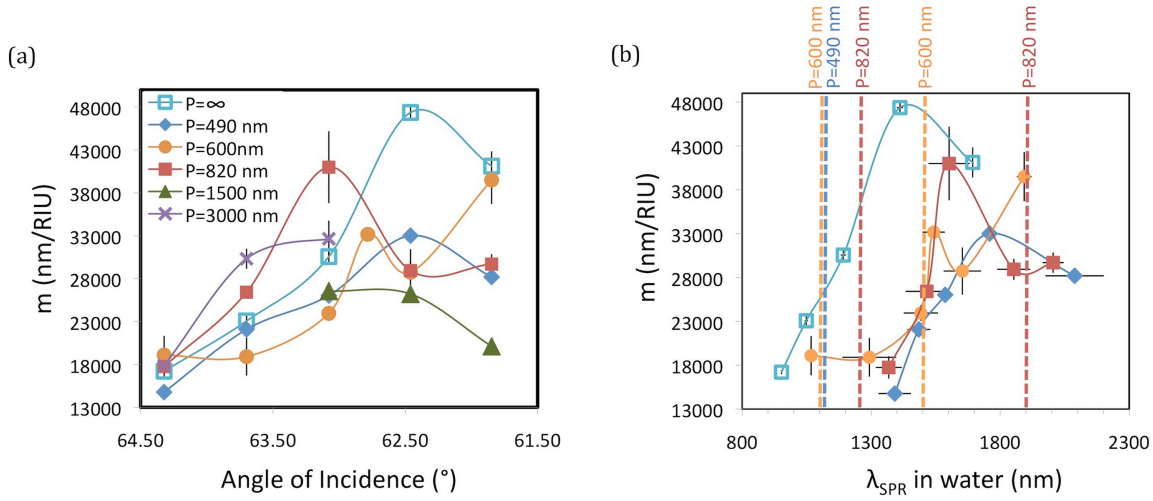

Figure 5.9: Bulk sensitivity of various periodicity (D/P= 0.36 ± 0.02) nanohole arrays as a function of (a) incident angle and (b) λ_{SPR}. P=∞ represents continuous gold. The λ_{SPR} of sample sensitive Bragg SPs are represented by dashed lines in (b).

5.6 Surface sensitivity

The surface sensitivity of nanohole arrays of various diameter, periodicity, and wavelength was measured and compared to continuous gold to determine optimal nanohole array parameters for sensing in NIR Kretschmann configuration and to investigate the fundamental l_d characteristics. Sensitivity was calculated for specific analyte thicknesses; d=10, 100, and 500 nm, with negligible linkage layer thickness. These thicknesses represent a range of SPR analytes, such as proteins, cell membranes, protein scaffolds, viruses, etc... The measured response to a 10 nm adlayer is also presented, because this thickness regime represents the majority of SPR studies based on protein binding. Furthermore, measurements are executed in aqueous environments with an adsorbate of similar RI to a protein, which mimics the environment of biosensing conditions.

It is necessary to determine wavelength dependent η_{PEM} values for accurate calculation of SP penetration depth (l_d) and subsequently, surface sensitivity ($\mathrm{m_{surf}}$) of nanohole arrays. The η_{PEM} was calculated according to the previously presented method in section 4.4 which utilizes measured $\Delta\lambda_{\mathrm{SPR}}$ for sequential buildup of five PEM

bilayers on continuous gold, measured PEM thickness, and previously determined l_d. The PEM thickness (d) of five bilayers was determined by AFM in water (via procedure presented in section 4.2.6), then d for 1-4 bilayers was calculated from the established linear thickness vs. bilayer number relationship (refer to section 4.4) [97]. The l_d values used in this study are calculated from the previously determined relationship for l_d and wavelength (refer to section 4.3);

$$l_d = 6.308\text{E–}4\,\lambda_{\text{SPR}}^2 + 2.352\text{E–}1\,\lambda_{\text{SPR}} - 128.0 \tag{5.2}$$

The prior measurements were performed on gold with a self assembled monolayer precursor to PEM buildup. Therefore, l_d was affected by the thiol bonding of this monolayer to the surface. Contrastingly, the PEMs for this investigation bind directly to the gold by electrostatic interaction, so l_d values should be corrected to represent non-functionalized gold by reducing l_d measurements from thiolated gold by a theoretical estimate of 5%. This reduction rate is determined by comparing theoretical results from Maxwell's equations where gold complex permittivity values[176] are implemented as unaltered values or reduced according to the conductivity drop from thiol attachment to gold as measured by Zhang et. al.[184] Differences in l_d due to effective refractive index of the solution and PEM layer with and without the thin monolayer is minimal (<0.1%), as expected. Therefore, a total 5% difference in l_d is considered and results in a negligible difference (0.14%) in η_{PEM}, so that l_d values measured from thiolated gold are acceptable for η_{PEM} calculation. The PEM refractive index was determined at five different λ_{SPR} ranging from 1070 ± 15 nm to 2050 ± 19 nm and a second order polynomial was fit to the five data points, $R^2 = 0.943$;

$$\eta_{PEM} = 4.63\text{E–}8\,\lambda_{\text{SPR}}^2 - 1.70\text{E–}4\,\lambda_{\text{SPR}} + 1.41 \tag{5.3}$$

η_{PEM} from this equation is used for m_{surf} calculations at specific wavelengths.

The m_{surf} for nanohole arrays with various nanohole diameter and consistent

P=820 nm was calculated by equation (5.1) at λ_{SPR} = 1440 nm, and a decrease with D/P is observed. Despite decreasing l_d with increasing D/P as illustrated in figure 5.10(a), the m_{surf} also decreases with increasing D/P due to variable bulk sensitivity. The resulting m_{surf} is displayed in figure 5.10(b) for analytes with thickness of d=10, 100, and 500 nm. There is no statistical difference in m_{surf} for the smallest D/P nanohole array substrate and continuous gold ($7 \pm 8\%$ difference for 10 nm analyte), and m_{surf} decreases with increasing D/P. The measured $\Delta\lambda_{SPR}$ for two PEM bilayers represents an experimental metric of m_{surf} for a 10 nm analyte (Figure 5.10(a)). The most sensitive D/P is 0.27, but at the given wavelength, does not exhibit improved m_{surf} over continuous gold.

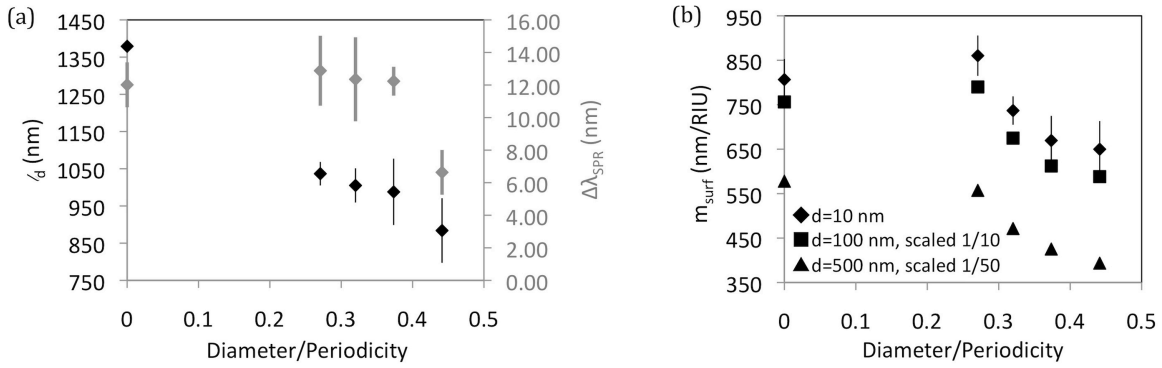

Figure 5.10: SP (a) l_d, $\Delta\lambda_{SPR}$ for two PEM bilayers (d=10 nm), and (b) surface sensitivity of various D/P nanohole array substrates (P=820 nm, λ_{SPR} = 1440 nm). D/P=0 represents continuous gold. Error bars on l_d represent standard deviation of l_d calculated from different thicknesses (1-5 bilayers). Error bars on $\Delta\lambda_{SPR}$ and surface sensitivity represent standard deviation of triplicate measurements.

The dependency of nanohole array m_{surf} on nanohole periodicity was investigated at λ_{SPR} = 1460 nm for various periodicity nanohole arrays with consistent D/P (0.36 ± 0.2). The l_d increases with periodicity where continuous gold is characterized by infinite periodicity. The $\Delta\lambda_{SPR}$ for two PEM bilayers indicates similar m_{surf} for 10 nm PEM, regardless of periodicity (Figure 5.11(a)). However, the calculated m_{surf} demonstrates an apparent increase with periodicity from P=600 - ∞ nm (Figure 5.11(b)). At

D/P=0.36 ± 0.2 nm and λ_{SPR} = 1460 nm, m_{surf} is highest for continuous gold, followed by P=820 nm.

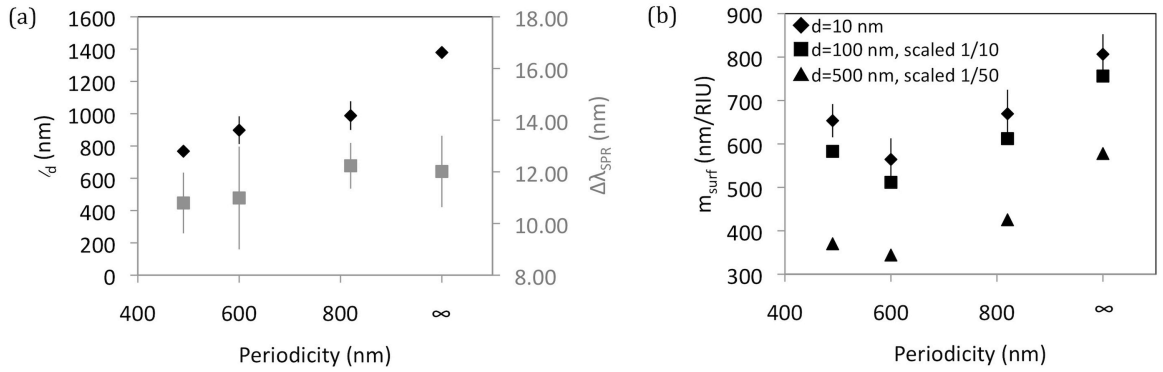

Figure 5.11: SP (a) l_d, $\Delta\lambda_{SPR}$ for two PEM bilayers (d= 10 nm), and (b) surface sensitivity of various periodicity nanohole array substrates (D/P=0.36 ± 0.2 nm). P=∞ represents continuous gold. Error bars on l_d represent standard deviation of l_d calculated from different thicknesses (1-5 bilayers). Error bars on $\Delta\lambda_{SPR}$ and surface sensitivity represent standard deviation of triplicate measurements

The m_{surf} and l_d may be further optimized by controlling λ_{SPR}. The wavelength profile of m_{surf} of a nanohole array with P=820 nm, D/P=0.37, and 78 ± 5 nm thick was investigated and compared to continuous gold. l_d increases with wavelength and is consistently lower than l_d of SPs on continuous gold (Figure 5.12(a)). Despite smaller l_d, the reduced m causes m_{surf} for the nanohole array to remain less than or equal to that of continuous gold (Figures 5.12). The local m_{surf} maximum occurs at λ_{SPR}=1550 nm for the nanohole array and at λ_{SPR}=1300 nm for continuous gold. For the nanohole array, there is an improvement of 201±18% in m_{surf} to a 10 nm analyte measured at λ_{SPR}=1550 nm compared to measurement at λ_{SPR}=1310 nm. Interestingly, for continuous gold, there is an improvement of 202±42% in m_{surf} to a 10 nm analyte measured at λ_{SPR}=1300 nm over measurement within the conventionally used visible region (λ_{SPR}=700 nm). Thus, highest m_{surf} is achieved at λ_{SPR}=1300 nm for continuous gold (50 ± 2 nm thick) and at λ_{SPR}=1550 nm for a nanohole array of the given parameters.

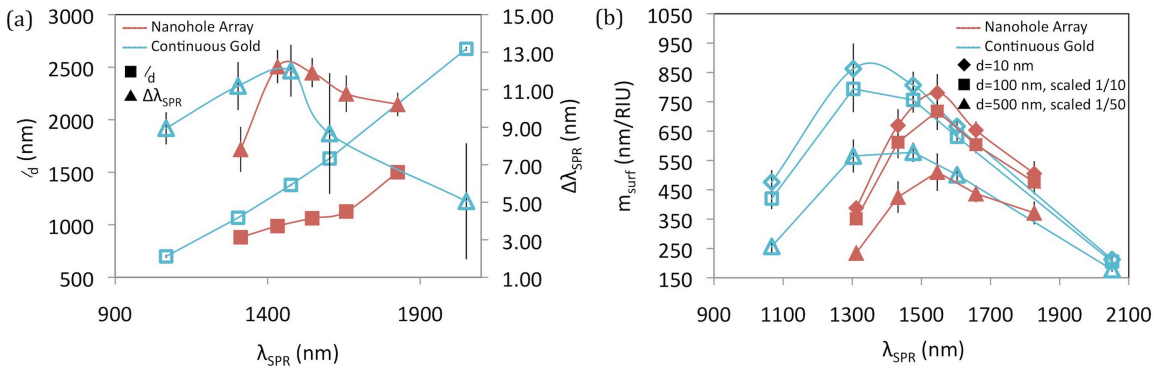

Figure 5.12: SP (a) l_d, $\Delta\lambda_{SPR}$ for two PEM bilayers (d=10 nm), and (b) m_{surf} of continuous gold (open red markers) and nanohole array substrates (P=820nm, D/P=0.36 $\pm$ 0.2 nm) (filled blue markers) at various wavelengths. Lines are added to guide the eye. Error bars on l_d represent standard deviation of l_d calculated from different thicknesses (1-5 bilayers). Error bars on $\Delta\lambda_{SPR}$ and m_{surf} represent standard deviation of triplicate measurements

The analysis of the m_{surf} as a function of D/P, P, and λ_{SPR} has established optimal nanohole array parameters as measured; D/P=0.27, P=820 nm, and λ_{SPR}=1550 nm. m_{surf} for these optimized nanohole array parameters is compared to continuous gold at its most sensitive λ_{SPR} (1300 nm) for different analyte thicknesses (Table 5.2). The nanohole array substrate demonstrates an improvement of 130 $\pm$ 16% for d=10 nm, a thickness representative of experiments based on protein-protein interaction. Considering adjustments to thiol-functionalized, continuous gold l_d to represent non-functionalized, continuous gold, the improvement is reduced to 124$\pm$15% for d=10 nm. The optimized nanohole array exhibits a larger sensitivity over continuous gold sensing substrates.

The nanohole array m_{surf} calculations are validated by comparing predicted and measured $\Delta\lambda_{SPR}$ for a 106 nm thick PEM at λ_{SPR}=1440 nm. $\Delta\lambda_{SPR}$ was measured for formation of 19 PEM bilayers (106 $\pm$ 1 nm) on a nanohole array (D/P=0.32, P=820 nm). $\Delta\lambda_{SPR}$ was predicted from m_{surf} by $\Delta\lambda_{SPR} = m_{surf}(\eta_{PEM} - \eta_{water})$. There is no statistical difference between predicted and measured $\Delta\lambda_{SPR}$. The predicted shift for analyte adsorption to continuous gold was 157.5 $\pm$ 0.9 nm, and the measured shift

Table 5.2: Comparison of optimized continuous gold and nanohole array surface sensitivity at various analyte thicknesses.

Analyte Thickness (nm)	Continuous Gold m_{surf} (nm/RIU)	Nanohole Array m_{surf} (nm/RIU)	Improvement (%)
10	860 ± 40	1120 ± 130	130 ± 16
100	7940 ± 370	10,200 ± 1250	129 ± 17
500	28,300 ± 1300	34,800 ± 5700	123 ± 21
1500	43,700 ± 2000	50,600 ± 15,700	116 ± 36

Conditions were optimized for continuous gold (λ_{SPR} = 1300 nm) and nanohole array substrates (λ_{SPR} = 1550 nm, D/P=0.27, P=820 nm) accordingly. Improvement is given for increase in m_{surf} of nanohole array as compared to continuous gold. The m_{surf} for analyte thicknesses > 500 nm are statistically similar.

was 164 ± 6 nm. The values agree within experimental error with 95% confidence (t=1.8, t_{table}=4.3). The predicted shift for analyte adsorption to the nanohole array (D/P=0.32, P=820 nm) was 146.6 ± 0.7 nm, and the measured shift was 120 ± 18 nm. Again, the values agree within experimental error with 95% confidence (t=2.5, t_{table}=4.3). The disparity in expected compared to measured shift is due to the deviation in the measured shift; 15% relative standard deviation (RSD), whereas there was 0.3% RSD for continuous gold.

5.7 Adsorbate attachment effect on nanohole array l_d and m_{surf}

The $\Delta\lambda_{SPR}$ due to adsorbate effects on gold permittivity, $\Delta\lambda_{SPR,\epsilon m}$, perturbs l_d and m_{surf}, thus $\Delta\lambda_{SPR,\epsilon m}$ was considered in all presented calculations. As previously described in chapter 4, bonding of the adsorbate to the gold greatly affects the gold permittivity and its plasmonic characteristics. The extent of this effect is represented by $\Delta\lambda_{SPR,\epsilon m}$, and may be quantified by solving the linear fit of $\Delta\lambda_{SPR}$ vs. d for d=0 (refer to section 4.3). Similarly, but to a lesser extent than bonding, electrostatic adsorption of PEM layers directly to the gold surface induces a change in gold permittivity. For continuous gold at various wavelengths, $\Delta\lambda_{SPR,\epsilon m}$ ranges from -3.5 to 0.4

nm ($\overline{\Delta\lambda}_{\mathrm{SPR},\epsilon m} = -2.2 \pm 1.7$ nm). For nanohole arrays of various parameters, $\Delta\lambda_{\mathrm{SPR},\epsilon m}$ ranges from -3.5 to 2.1 nm ($\overline{\Delta\lambda}_{\mathrm{SPR},\epsilon m} = 0.5 \pm 0.6$ nm). Although the $\Delta\lambda_{\mathrm{SPR},\epsilon m}$ is effectively zero, the effect at smaller thicknesses is substantial. In this case, $\Delta\lambda_{\mathrm{SPR},\epsilon m}$ is a greater proportion of the total measured $\Delta\lambda_{\mathrm{SPR}}$. The RSD for l_d calculated from analyte thicknesses of 5-23 nm improves by an average of 137±24% when $\Delta\lambda_{\mathrm{SPR},\epsilon m}$ is included, and there is an additional gain in accuracy and precision for increased sampling at the five different thicknesses required for determining $\Delta\lambda_{\mathrm{SPR},\epsilon m}$ rather than one thickness.

The importance of including $\Delta\lambda_{\mathrm{SPR},\epsilon m}$ in l_d and $\mathrm{m_{surf}}$ calculations increases for conditions involving adsorbate bonding, nanostructured surfaces, and/or increasing wavelength. The effects of Au-S bonding on gold permittivity of a nanohole array are increased compared to continuous gold (refer to section 4.5). For a nanohole array (D/P=0.29, P=820 nm) at $\lambda_{\mathrm{SPR}} = 883$ nm, $\Delta\lambda_{\mathrm{SPR},\epsilon m} = -31.3 \pm 3.8$ nm for Au-S bonding. This magnitude is three times larger than $\Delta\lambda_{\mathrm{SPR},\epsilon m}$ for Au-S bonding to continuous gold under the same conditions (-10.2 ± 1.4 nm). The RSD for nanohole array l_d calculated from analyte thicknesses of 9-70 nm improves by 2750% when $\Delta\lambda_{\mathrm{SPR},\epsilon m}$ is included (8% RSD compared to 220% RSD). Furthermore, the magnitude of $\Delta\lambda_{\mathrm{SPR},\epsilon m}$ for continuous gold increases with wavelength from -5.6 ± 0.2 nm at $\lambda_{\mathrm{SPR}} = 700$ nm to -16 ± 3 nm at $\lambda_{\mathrm{SPR}} = 1150$ nm. Thereby, consideration of $\Delta\lambda_{\mathrm{SPR},\epsilon m}$ for nanohole array l_d and $\mathrm{m_{surf}}$ becomes extremely important for situations were bonding occurs and/or higher wavelengths are implemented.

5.8 Conclusion

The SP characteristics of nanohole arrays have been investigated throughout the NIR region as a function of D/P, P, and λ_{SPR} to establish trends and optimize surface sensitivity to specific analytes. Various Bragg SPs are supported in the NIR and depend on array periodicity. The maximum bulk sensitivity of the nanohole array propagating SP is affected by interactions with these Bragg SPs. Consequently, the bulk sensitivity may be tuned by the periodicity. Bulk sensitivity decreases with

nanohole array diameter, however penetration depth must also be considered in assessing the m_{surf} to different analyte thicknesses. Consideration of adsorbate effects on gold permittivity was implemented to increase accuracy and precision in penetration depth and subsequent m_{surf} values. Surface sensitivity was greatest for P=820 nm, D/P=0.27, and λ_{SPR}=1550 nm, within the given investigated conditions. This nanohole array structure demonstrated a $130 \pm 16\%$ increase in surface sensitivity for 10 nm analyte over continuous gold at its optimal λ_{SPR} (1300 nm).

Chapter 6

PLASMONIC INTERACTION BETWEEN A SINGLE NANOPARTICLE AND A NANOHOLE ARRAY

6.1 Introduction

Current SPR spectroscopy research seeks to increase the control of the plasmonic field enhancement and environmental sensitivity, one predominant means of which is the use of nanostructured materials that support surface plasmons (SPs).[52, 43] The primary difference between SPs supported on nanostructures versus continuous films is that SPs propagate along the surface in continuous films of plasmonic materials, whereas in plasmonic nanostructures, the SP exists as a standing wave that is confined to the nanostructure. Thus, SPs on nanostructures are localized to the structure (a "localized surface plasmon" (LSP)) and amplify the local field intensity.[66, 62] Fundamentally, both types of SPs are collective oscillations of electrons at the interface of plasmonic and dielectric materials, and the SPs are excited when the momentum of incident light matches that of the SP, i.e. surface plasmon resonance (SPR) occurs. For propagating SPs excited at a specific incident angle and for LSPs, SPR manifests as an extinction band at a specific wavelength of light in a broadband spectrum, known as the SPR wavelength (λ_{SPR}). Also, both propagating SPs and LSPs exist as evanescent waves, which leads to confinement of the field and sensitivity to changing conditions near the surface.[44] In particular, SPR spectroscopy measurements can a detect change in refractive index of the surrounding dielectric sample as a shift in the SPR response, which, is wavelength ($\Delta\lambda_{\mathrm{SPR}}$) in this case. This is the basis for SPR sensing. The refractive index sensing capability as well as the field enhancement may be increased when SPs of nearby plasmonic structures interact.[62, 112] Within this chapter, a

technique for mapping the interaction of a nanoparticle and plasmonic substrate SP is demonstrated which could be applied to optimizing interaction and field intensification.

The relative position and gap distance of plasmonic structures affect the sensing capability and field intensification.[62, 112, 207] Under specific conditions, nearby SPs couple together and the electric field between the structures is further amplified and localized (details may be found in chapter 1.6), which may be exploited for sensing purposes and surface enhanced techniques, such as tip enhanced Raman spectroscopy (TERS) or surface enhanced Raman spectroscopy (SERS).[208, 62, 122] Plasmonic coupling decreases exponentially with distance between structures, whereby greatest coupling is achieved at gap distances of less than 0.2× the diameter of the nanostructure.[62, 112] Within this distance regime, gap mode enhancement may occur where the field intensity between nanostructures is greatly intensified by up to five orders of magnitude.[62] In addition to increased field intensity, a shift in the SPR wavelength and broadening of the peak occurs due to coupling.[207, 209] In this manner, the coupling of SPs may be evaluated. The fundamental study of plasmon coupling as a function of gap distance and relative location may be used for optimizing field amplification and ultimately combining TERS and SERS substrates or increasing biosensor sensitivity. In particular, this chapter investigates the development of a technique for mapping the interaction of a nanosphere affixed to an AFM probe (effectively a TERS probe) over a plasmonic nanohole array and presents the results of these interactions.

As discussed in the preceding chapters, nanohole arrays uniquely support both propagating SPs between the holes as well as LSPs within the holes leading to extensive investigation for numerous applications. Of particular interest, they may be used for biosensing [76, 149, 153, 136] and SERS [127, 128]. The coupling of nanostructures to the nanohole array could further increase the function of these sensors. An SPR sensor utilizing the coupling between nanohole arrays and nanoparticles has not been demonstrated in current literature, but other gap mode SPR sensors based on multiple nanoparticles or a nanoparticle and thin film have shown increased sensitivity over isolated structures. [1, 113, 114] Therefore, the superior sensitivity of the nanohole

array, over both nanoparticles and thin films,[55] suggests gap mode coupling capability with nanohole arrays could also surpass sensors based on these architectures. A related SERS study exhibited a 100-fold increase in SERS signal for a nanohole-nanoparticle substrate compared to traditional nanoparticle aggregates has been achieved [210], and could be further improved by optimizing gap distance [62, 112].

Darkfield imaging of the nanohole array SPR wavelength and intensity with varying single nanoparticle (SNP) probe-nanohole positions can elucidate the location specific SP interaction and optimal enhancement conditions. Different optical modes may be used to excite and directly observe the nanohole array SPs.[126, 138, 144, 205, 142] Darkfield spectroscopy was chosen for this study, wherein the reradiated light coupled to SPs was measured, and the characteristic SPR wavelength shift ($\Delta\lambda_{SPR}$) was evaluated as a direct indicator of the SPR conditions including surrounding refractive index and SP coupling. This study offers experimental investigation of SP coupling as a function of controlled relative location that is complementary to available finite differential time domain (FDTD) simulations [210, 211]. Studies of nanostructure interactions with a similar nanostructure or with a continuous metal film where the relative position is controlled by scanning probe microscopy has been examined in literature.[212, 213, 214, 215] However, the current literature lacks investigation of more complex nanostructures such as nanohole array-nanoparticle interaction and the imaging of such interactions has not been well documented. The imaging of transmission through standalone nanohole arrays in the farfield [216, 217] and nearfield [17, 18, 218, 219] has been established where low divergence of light ($<3^{\circ}$) and beaming or increased directionality of the light occurs[17, 18, 218, 220]. These images focus solely on the intensity with the exception of the study by Bohn et. al.[217] in which the dispersion curves were mapped for various conditions. This chapter seeks to image the intensity as well as the location specific λ_{SPR} of a nanohole array with and without interaction of a SNP by integrating scanning probe microscopy (SPM) with darkfield spectroscopy. Software controlled hyperspectral imaging of the nanohole array is demonstrated in addition to the SNP-nanohole array surface plasmon interaction

at a single nanohole array position. This chapter presents the first empirical observations of SPM controlled gap mode enhancement of more complex nanostructures and allows for optimization of positioning prior to sensing applications. The SPM-SPR instrument has great implications to the field for analysis of several structures in a similar manner.

6.2 Experimental methods

6.2.1 Nanohole array fabrication

Circular glass coverslips (Fisher Scientific, Fairlawn, NJ, 25 mm diameter) were cleaned by immersion in boiling piranha solution (3:1 (v/v) concentrated H_2SO_4 : 30% H_2O_2) (Fisher Scientific, Fair Lawn, NJ) for at least one hour, triplicate rinsing and sonication in deionized water for one minute, and drying with nitrogen gas (Keen Compressed Gas Co., Wilmington, DE). *Caution: boiling piranha solution is very corrosive and should be handled with extreme care.* The clean coverslips were sputter coated in a DC magnetron sputterer (Cressington Scientific Instruments Ltd., model 308R, Watford, UK) with a 5 nm chromium (99.95 + %, Kurt J. Lesker Co., Clairton, PA) adhesion layer and 60 nm gold (99.99%, ESPI Metals, Ashland, OR) layer.

The nanohole array perforations were formed by focused ion beam (FIB) milling a gold-coated glass cover slip to form a 100 μm $\times$ 100 μm, hexagonally patterned nanohole array with 490 nm hole center-to-center separation and 224 nm hole diameter. FIB milling was performed at a beam current of 460 pA and an acceleration voltage of 30 eV. Nanohole arrays may be fabricated easily and homogeneously over large-scale areas (mm) by a nanosphere lithography technique for application [221, 222] (section 2.3), however, to ensure a well-defined, defect-free area for this fundamental study, focused ion beam milling was employed.

6.2.2 Atomic force microscopy

The physical parameters of the nanohole array substrate were determined by atomic force microscopy (AFM). A Bruker Optics (Billerica, MA) Dimension AFM

equipped with a silicon TAP-300-G probe (Innovative Solutions Bulgaria Ltd., Sofia, Bulgaria) was used in tapping mode in air. Three $5 \times 5\,\mu m^2$ images were acquired and the average depth, diameter, and periodicity for > 90 nanoholes per image was calculated using Bruker Optics Nanoscope software.

6.2.3 Integrated AFM-darkfield measurements

A MV2000 scanning probe microscope (SPM) (Nanonics Imaging Ltd., Jerusalem, Israel) was used for atomic force microscopy (AFM) measurements integrated with darkfield spectroscopy measurements acquired on a Bruker Optics (Billerica, MA) SENTERRA microscope spectrometer. The source was a Xenon arc light (Ushio, Tokyo, Japan), and the collected light was dispersed with a 1200 grooves/mm grating (0.1 nm resolution). The spectra were acquired from 532-812 nm with 20 s integration time and 3 co-additions. A 50 μm aperture was utilized in the confocal setup, which allows for a collection spot size of $\approx 2\,\mu$m. The MV2000 allows independent piezoelectric movement of both the sample and probe and provides a free optical path in which the nanohole array and probe were positioned for collection of scattered light (Figure 6.1). Within the microscope optical train, a darkfield condenser (Olympus, Center Valley, PA) was focused on the underside of the nanohole array sample and a 100× long working distance objective (Nikon, Tokyo, Japan) was focused on the opposing side of the sample for collection of light scattered from the sample. The darkfield condenser ($NA = 0.92 - 0.8$) produces a hollow cone of illumination, which lies outside the cone of acceptance of the objective ($NA = 0.7$), so that only scattered light is collected. Thereby, light scattered from the interaction point of the nanohole array sample and a SNP probe (a 200 nm diameter gold nanosphere affixed to a AFM probe, effectively a TERS probe) was measured where the SPM was used to position the SNP probe (Nanonics Imaging Ltd., Jerusalem, Israel) in relation to the nanohole array sample. The position was measured and controlled by an oscillation feedback mechanism of the tuning fork attached to the SNP probe.

The light scattered from the nanohole array was collected by the spectrometer

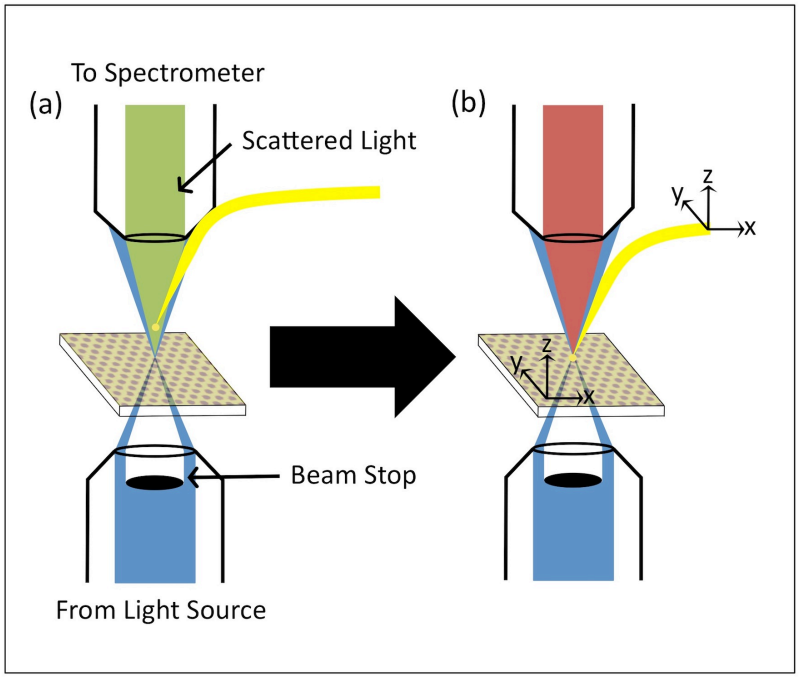

Figure 6.1: Simplified integrated scanning probe microscope and optical spectrometer schematic demonstrating measurement of scattered light from nanohole array sample with SNP probe out of contact (a) and in near-contact (b) with the nanohole array.

at specific SNP-nanohole array positions. The SPM system can control the motion of both the SNP and sample in the X, Y and Z directions. As the SNP is brought into and out of near-contact with the nanohole array, a change in the wavelength of scattered light may be detected (Figure 6.1). The SPM operates in tapping mode, where the probe oscillation is approximately 5 nm; therefore, near-contact refers to an oscillating tip-sample distance of 0-5 nm. The SPM and optical measurements are integrated to enable automatic triggering of spectral acquisition at specified points of stationary rest throughout the AFM scan. In this manner, location specific darkfield scatter spectra are compiled to form a raster image of the nanohole array spectral features. Specifically, a second order polynomial was fit to the darkfield scatter peak and the zero of the derivative of the curve was solved to determine the darkfield spectrum maximum. The wavelength corresponding to this maximum for the spectral series was assembled into a hyperspectral image using MATLAB software.

The instrument is capable of imaging by movement of either the nanohole array or SNP, while holding the other component stationary. Either the piezoelectrics supporting the sample or the probe may be used for XY scanning and Z feedback. However, in the current electronic configuration, XY scanning by the sample piezoelectrics is necessary for software controlled integrated measurements, therefore manual positioning of the SNP is necessary when utilizing raster scanning of the probe, not the nanohole array. A spectral image of the nanohole array with the SNP positioned outside of the field of view was collected to demonstrate imaging capability of the nanohole array without SNP interaction (Figure 6.4). To observe SNP-nanohole array interaction, the nanohole array was kept stationary while the SNP was manually scanned across the nanohole array with near-contact maintained throughout the scan (Figures 6.5 and 6.6). In this instance, the spectra represent the same sample position with varying SNP position.

6.3 Darkfield spectroscopy of nanohole array substrate

The darkfield spectrum of a nanohole array exhibits a peak in intensity that corresponds to the surface plasmon resonance excitation wavelength (λ_{SPR}) (Figure 6.2, black). The λ_{SPR} depends on the dimensions of the nanohole array, which are as follows for this particular sample; 224 nm nanohole diameter, 481 nm hole-to-hole periodicity, 41 nm depth of glass milled within the hole, and λ_{SPR} of 621.6±0.5 nm. The darkfield spectrum was determined by normalizing the sample spectrum by a reference spectrum of elastically scattered light from a scratched glass slide that is of similar intensity to the sample spectrum. A spectrum of the system dark noise was collected with the optics shuttered and this spectrum was subtracted from both the reference and sample spectra prior to analysis. A background spectrum is represented by the ratio of two reference spectra (Figure 6.2, grey).

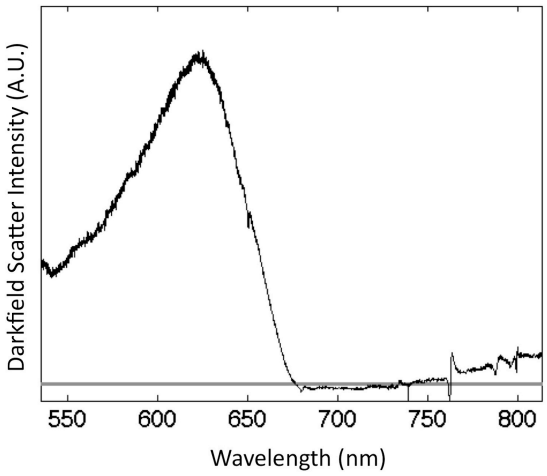

Figure 6.2: Representative normalized darkfield spectrum of nanohole array (black), $\lambda_{SPR} = 622$ nm, and background spectrum (gray).

The scatter mostly arises from the LSP, but the short range SPs couple with and greatly affect the LSP and the peak [205, 142, 211], thereby the peak represents a composite of the interaction of the short range SPs and the LSP of the hole within the wavelength region. Angle spread of the incident angle may cause a broadening of the measured peak due to angle dependency of the short range SPs.[126, 216] For this

setup, the hollow cone of incident light spans an angle range of 53° to 67°, so that the observed peak may be broader than that of a smaller angle range. The observed SP is sensitive to the surrounding refractive index, which in this case is glass (substrate supporting the nanohole array) and air (above the nanohole array). A shift in λ_{SPR} ($\Delta\lambda_{SPR}$) of the spectrum may arise from either a change in the refractive index or coupling of surface plasmons.

6.4 Integrated AFM-darkfield spectroscopic imaging

Location specific darkfield spectra were acquired to compile a hyperspectral image of the nanohole array. A 5×5 μm^2 AFM image of the nanohole array was collected to locate a region of interest (Figure 6.3). A small section of the AFM scan is selected for integrated AFM and optical measurements.

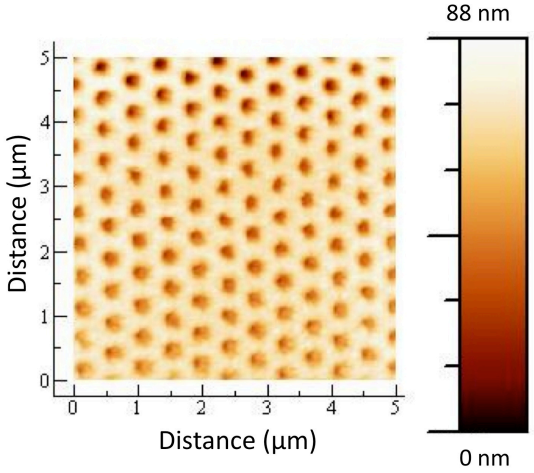

Figure 6.3: AFM image of nanohole array acquired with SNP probe.

Hyperspectral SPR imaging of the nanohole array was collected without interactions by the SNP. A 1.95 μm^2 AFM scan was attained (Figure 6.4(a)) with darkfield spectra acquired at points corresponding to an 11×11 grid throughout the scan. The λ_{SPR} was measured at each of 121 (X,Y) locations (Figure 6.4(b)) and converted to an optical λ_{SPR} mapping of the nanohole array (Figure 6.4(c)). The location was controlled by AFM where the probe was outside the collection spot, so the measured λ_{SPR}

of 621.6 ± 0.5 nm across the image represents the nanohole array without any interaction of a SNP. There is an apparent $\Delta\lambda_{SPR}$ (≈ 1 nm) laterally across the image (Refer to Figure 6.4(c) and periodic oscillations in Figure 6.4(b)) that most likely results from a change in incident angle[126, 216] caused by a slight change in position relative to the darkfield illumination cone and tilt of the sample within the illumination spot. The consistency in wavelength vertically across the image indicates minimal spatial drift, as the fast scan axis was in the X-direction.

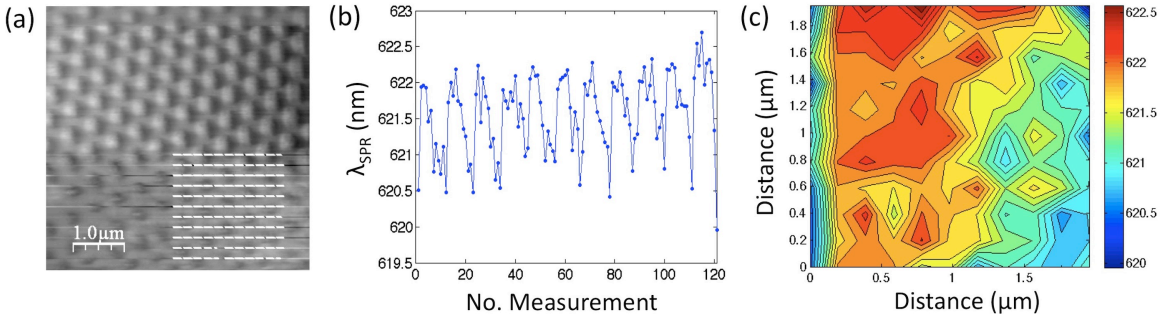

Figure 6.4: (a) AFM image acquired simultaneously with darkfield spectral acquisition where SPR measurement points within the scan are indicated by white dash marks. (b) corresponding λ_{SPR} at each measurement point (line added as guide) (c) SPR image of nanohole array λ_{SPR}(nm) (pixel spacing=195 nm).

6.5 SNP-nanohole array interaction

The interaction of a SNP with the nanohole array was investigated by scanning the probe over the stationary nanohole array. The SNP probe was scanned in a $10 \times 8\,\mu m^2$ area around the collection spot. Darkfield spectra were acquired at points spaced by 1 μm and the spectral range was reduced to 603-710 nm in order to capture the SPR feature but reduce acquisition time. The average λ_{SPR} across the image was 620 ± 3 nm. An increase in λ_{SPR} occurs when the SNP is in near-contact with the nanohole array within the collection spot (Figure 6.5). The increase in λ_{SPR} was constrained to a $1 \times 2\,\mu m^2$ region presented in figure 6.5(a) where five points centered at the focal spot demonstrate a $\Delta\lambda_{SPR}$ maximum of 8 nm and average of 6 ± 1 nm. This $\Delta\lambda_{SPR}$ is significant, as it is 12$\times$ larger than the λ_{SPR} deviation for the scanned nanohole array

without tip interaction (0.5 nm). The increase in λ_{SPR} indicates the region of SNP interaction with the nanohole array within the collection spot. The average λ_{SPR} for the single spot on the nanohole array without SNP interaction is determined by excluding the $1 \times 2\,\mu m^2$ region of SNP interaction where the SNP was within the collection spot. The nanohole array $\lambda_{SPR} = 619 \pm 2$ nm without SNP interaction. Relative to this λ_{SPR} rather than the average λ_{SPR}, the maximum $\Delta\lambda_{SPR}$ for interaction increases to 9 nm. Furthermore, this SPR image matches the scattering profile (Figure 6.5(b)), in which the scatter intensity is greater at the points of SNP-nanohole array interaction, indicating field enhancement and SP coupling. The scatter intensity was increased by $21 \pm 4\%$ when the SNP and nanohole array were in near-contact. Both the intensity and the λ_{SPR} increased when the SNP was in near-contact with the nanohole array within the collection spot.

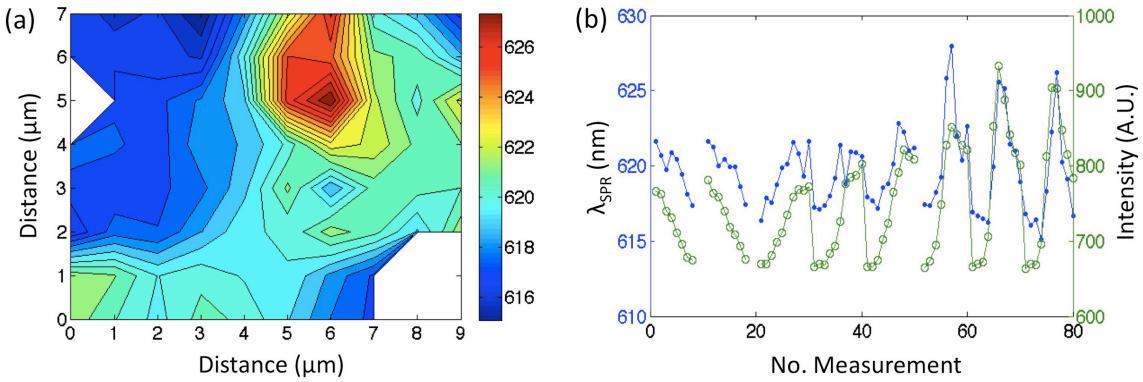

Figure 6.5: λ_{SPR} of stationary nanohole array with SNP probe positioned at various spots (spacing= $1\,\mu m$) represented as (a) spatial image where white space represents five missing data points and (b) corresponding λ_{SPR} (blue dots) and scatter intensity (green open circles) at each measurement point (line added as guide).

The field intensity of a nanohole array is greatest within the hole centers [128], thus the greatest interaction is expected when the probe is positioned within the hole as demonstrated by FDTD simulations by He et. al.[211] The location specific interaction of the SNP position within the hole compared to between the holes was investigated by imaging the SNP-nanohole interaction over a $1.2 \times 1.8\,\mu m^2$ region with 200 nm pixel

spacing. This spacing allows for spectral collection with the SNP in various (X,Y) positions relative to the center of several nanoholes within the collection spot. The average λ_{SPR} over the entire image is 617 ± 6 nm. Relatively large $\Delta\lambda_{SPR}$ from the average was confined to three points of variation, labeled 1-3 in figure 6.6, where SNP-nanohole array interaction exhibited a maximum $\Delta\lambda_{SPR}$ of 13 nm ($\lambda_{SPR} = 630$ nm) and an average $\Delta\lambda_{SPR}$ of 11 ± 7 nm ($\lambda_{SPR} = 628 \pm 4$ nm). The greatly shifted regions correspond to the SNP residing in or near the hole. The conversion of the voltage manually applied to the piezos for scanning of the tip cannot account for hysteresis in this case, which may induce up to 16% and 40% increase in the apparent distance along the x and y axis, respectively. With this consideration, the scanned area is reduced to $1.5 \times 0.72\,\mu m^2$, but potential effects of nonlinear motion are not compensated for. Within this area, it is deduced that the three spots of increased λ_{SPR} correspond to three nanoholes within the collection spot, refer to figure 6.6(b). Therefore, the average λ_{SPR} determined with the points of greatest variation removed represent the SNP-nanohole array interaction where the SNP resides at the gold between the nanoholes and is calculated to be 616 ± 3 nm. This scan was repeated and a maximum $\Delta\lambda_{SPR}$ of 17 nm was measured from an average λ_{SPR} of 618 ± 5 nm (Table I) and λ_{SPR} for SNP between nanoholes was 616 ± 3 nm. Again, an increase in intensity coincided with the $\Delta\lambda_{SPR}$ (Figure 6.6(b)), which further supports the coupling observation. The scatter intensity was increased by 31 ± 4% when the SNP was within the nanohole, with a maximum increase of 37%. The $\Delta\lambda_{SPR}$ for SNP within the nanohole measured from λ_{SPR} where SNP was between the nanoholes is significant, as it is more than 22× larger than the λ_{SPR} deviation for the scanned nanohole array without tip interaction (0.5 nm) and increased the scatter intensity. Both the field intensity and the λ_{SPR} increased for instances where the SNP was within the nanohole as compared to between holes.

The SNP occupies approximately 1% of the collection area. Thereby the measured darkfield spectrum is mainly representative of nanohole array region without direct SNP contact, however, the LSP and short range SPs interact so that the SNP affects SPs in surrounding regions and may cause a $\Delta\lambda_{SPR}$ for the entire collection area.

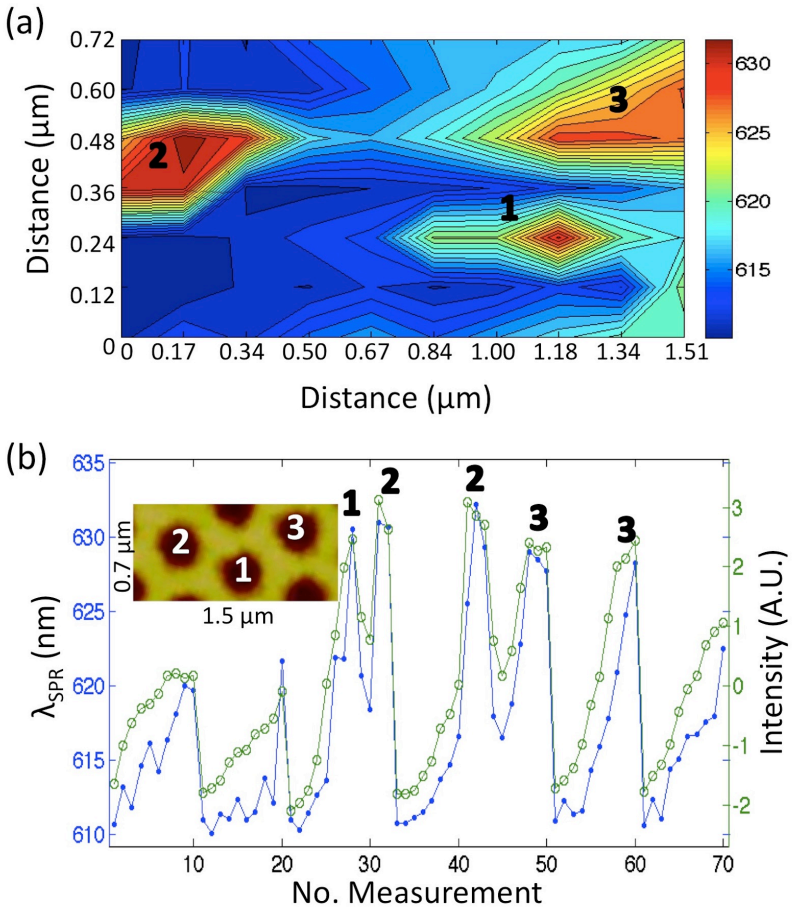

Figure 6.6: λ_{SPR} of stationary nanohole array with SNP positioned at various spots represented as (a) spatial image and (b) corresponding λ_{SPR} (blue dots) and mean centered scatter intensity (green open circles) at each measurement point (line added as guide) and inset AFM image of nanohole array outlining proposed scanned area and corresponding nanoholes with distance adjusted for hysteresis.

Nonetheless, the greatest effect occurs within the region where the probe resides, so a greater $\Delta\lambda_{SPR}$ could be measured by reducing the spot size toward the nanosphere size. The current technique remains useful for relative comparison in coupling efficiency and illustrates the composite SPR spectrum of the SNP-nanohole array LSP and several surrounding holes. For absolute comparison of scatter intensity increase, a correction factor for the ratio of the collection area to nanosphere area (100:1) is applied and increases the determined local scatter intensity enhancement to 137×. The collection area is determined from the spot size, and the nanosphere area is determined from its radius.

Table 6.1: $\Delta\lambda_{SPR}$ from average λ_{SPR} observed for SNP (TERS) probe or AFM probe in near-contact with stationary nanohole array (n > 40).

Probe	Pixel Spacing (μm)	Maximum $\Delta\lambda_{SPR}$ (nm)	Average λ_{SPR} (nm)
TERS	1	8	620 ± 3
TERS	0.2	13	617 ± 6
TERS	0.2	17	618 ± 5
AFM (Uncoated)	0.2	1	613 ± 1
AFM (Cr-coated)	0.2	4	613 ± 1

The observed increase in λ_{SPR} with SNP interaction was not due simply to increased local refractive index change near the nanohole array, but rather from plasmonic coupling. Two AFM probes without nanoparticles affixed to the end were scanned across the stationary nanohole array to observe $\Delta\lambda_{SPR}$ due to refractive index change from air to the probe material, which was silica or chromium-coated silica (Table I). Similar parameters to the SNP scan with 0.2 μm pixel spacing across the stationary nanohole array were implemented. For an uncoated AFM probe, approximating the

SNP probe without nanosphere, a maximum $\Delta\lambda_{SPR}$ of 1 nm was observed. The gold nanosphere on the uncoated single nanoparticle affixed AFM probe induced a 17× higher $\Delta\lambda_{SPR}$ than just the silica AFM probe residing within the hole. Likewise, a sharper, chromium-coated AFM probe (tip diameter = 20 nm) induced a maximum $\Delta\lambda_{SPR}$ of 4 nm. The chromium coating and sharper tip simulated a higher refractive index and deeper penetration into the hole, yet the $\Delta\lambda_{SPR}$ remained significantly less than that measured for the SNP probe interaction.

Furthermore, the measured $\Delta\lambda_{SPR}$ is significantly larger than the predicted $\Delta\lambda_{SPR}$ due to refractive index change from the nanoparticle. The expected shift, $\Delta\lambda_{SPR}$, is approximated for a RI change from air, η_{air} = 1.0003 RIU at λ_{SPR} =632 nm [223], to an effective refractive index, η_{eff}, composed of both the nanoparticle and surrounding air;

$$\Delta\lambda_{SPR} = m(\eta_{eff} - \eta_{air}) \tag{6.1}$$

The RI sensitivity of the nanohole array, m (226 nm/RIU), was obtained from Murray-Methot et. al.[156] and η_{eff} is determined from the sensing volume fraction that the nanoparticle occupies ($V_{sensing}/V_{NP}$);

$$\eta_{eff} = \eta_{air}(1 - V_{sensing}/V_{NS}) + \eta_{NP}(V_{sensing}/V_{NS}) \tag{6.2}$$

The sensing volume, $V_{sensing}$, is calculated from the spot size and SP penetration depth determined by Couture et. al.[55], and the volume of the nanosphere residing within the SP penetration depth, V_{NS}, is considered. The refractive index of a gold nanoparticle deviates from that of continuous gold, so η_{NP} (3.184 RIU at λ_{SPR} = 632 nm) is estimated as an average value from two literature sources [224, 225] approximating the given experimental conditions. By equation (6.2), the estimated $\Delta\lambda_{SPR}$ for η_{air} to η_{eff} is 3.7 nm, whereas the measured $\Delta\lambda_{SPR}$ ranges from 8-17 nm. The significantly larger measured $\Delta\lambda_{SPR}$ value indicates additional effects from SP coupling. Furthermore, the expected $\Delta\lambda_{SPR}$ due to RI change is similar to that observed for the

non-plasmonic chromium-coated probe (4 nm).

It should be noted that the variation in λ_{SPR} across trials without SNP interaction (from 622 to 613 nm) may be due to slight tilt in the sample which changes the angle of incidence and shifts λ_{SPR}.[126, 216] However, this does not affect the study of interaction as $\Delta\lambda_{SPR}$ is measured relative to the particular trial and sample position. Future studies may establish spot specific non-coupled λ_{SPR} by incorporating spectral collection at each point with the SNP outside of the interaction distance range.

6.6 Additional instrumentation characterization

The stability and capability of the integrated SPM optical instrumentation is important to determine the system capability and has been characterized accordingly. Stage drift was less than 0.44 μm/16 h and linearization coefficients accounted for piezo hysteresis to within 1.5% and 1.1% in the x and y directions. The measurable spectral range for the given setup was $532-1000$ nm with manual concatenation necessary for spanning ranges > 100 nm. For software controlled integrated measurements, the electronic configuration is such that the XY raster scanning and Z offset must all be performed by the same piezo (upper or lower). Thereby, when scanning the sample, it is also offset in the Z direction during automated offset measurements where rastered measurements are acquired with the sample and SPM probe in contact, then retracted to a specified offset distance. To investigate the effects on intensity, Raman signal with the sample positioned within the Z collection volume (714 nm by Abbe resolution) was measured with a 20 μm aperture. A negligible 3% reduction in Raman intensity was observed when the sample was retracted by 200 nm. Furthermore, the darkfield scatter peak for the FIB milled nanohole sample (613.6 ± 0.8 nm) is not statistically different from when the sample is retracted 200 nm (613.5 ± 0.9 nm; $t_{calc} = 0.22 < t_{table} = 2.53(n = 14)$. However, for a larger retraction of 1 μm, an 11.2% reduction in Raman signal was observed.

6.7 Conclusion

The coupling of surface plasmons on a nanohole array and a nanosphere affixed to a AFM probe at various lateral locations has been demonstrated in addition to the ability for hyperspectral imaging of the nanohole array. This chapter presents the first empirical observations of SPM controlled gap mode enhancement of more complex nanostructures and allows for optimization of positioning prior to sensing applications. The findings for greatest enhancement with the nanoparticle positioned within the nanohole are validated by agreement with theoretical studies on nanohole array-nanoparticle gap mode enhancement.[211, 210] The SPM-SPR instrument has great implications to the field for analysis of several structures in a similar manner. The system is capable of hyperspectral imaging, similar to figure 6.4, where the SNP is held at a specified distance above the sample during the optical measurement. In this manner, future studies may be performed with the SNP in focus where interaction with the nanohole array is imaged at varying gap distance from 5-100s of nanometers to discern the gap distance for greatest gap mode field enhancement. Also, the $\Delta\lambda_{SPR}$ and increased scatter due to interaction can be isolated by determining $\Delta\lambda_{SPR}$ as a difference from λ_{SPR} with the nanoparticle-affixed AFM probe retracted from the sample (outside the coupling distance). Furthermore, the use of polarized light could increase the enhancement [62] and evidence of coupling could be supplemented by observing the FWHM of the peaks by collecting the full spectral peak.[207, 209] Additionally, the SPM-SPR instrument may be used for combined Raman enhancement of SERS and TERS, which has only been previously studied for TERS measurements of benzenethiol on roughened ($>$ 2 nm) gold surfaces (SERS substrate) with a 10-fold enhancement observed at sharp edges.[226]

Chapter 7

CONCLUSION

7.1 Main Conclusions

This dissertation established novel analytical methods to evaluate the tunable properties and increased sensitivity of nanohole array SPR sensing substrates both in the near infrared and in interaction with other nanostructures. Increased surface sensitivity will improve sensing capability for discriminating small changes in concentration, detecting proteins with poor binding affinity, and detecting even lower concentration biomarkers.[44, 45, 6, 7] The available nanohole array SPR modes were presented and measurement of propagating modes in Kretschmann configuration was substantiated as the foremost mode for SPR sensing. The tunability of SPR excitation wavelength (by incident and azimuthal angles) and physical parameters (nanohole array diameter and periodicity) for sensitivity optimization and tailoring toward SP coupling was also demonstrated. An instrument accessory for Kretschmann configuration measurements in the NIR and a technique to improve the reliability of assessing SP properties, namely penetration depth, were developed. The instrument and technique were applied to evaluation of nanohole array sensing substrates with different physical parameters. The most sensitive nanohole array structure (820 nm periodicity, 0.27 diameter/periodicity, and λ_{SPR}=1550 nm) was found to improve surface sensitivity to protein-protein binding conditions by $130 \pm 16\%$ compared to using a continuous gold film substrate. Further enhancement of the SP field was enabled by development of an instrument for integrating scanning probe microscopy (SPM) control of a plasmonic nanostructure and SPR spectroscopy measurements. By these means, gap mode enhancement of the plasmic field between a nanohole array and nanosphere was observed at various lateral positions

between the structures. It has potential for measurements at various axial distances as well. These studies have implications for improved sensing capability and refined evaluation of SP properties, and they provide the basis for novel instrumentation and sensor architectures as discussed in the following sections.

7.2 Empirical findings

SPR active nanohole arrays support several types of SPs, all of which depend on physical parameters of the nanohole array. Chapter 2 discusses the SP types (propagating, Bragg, and localized surface plasmons) and excitation modes. Bragg SPs are excitable in each mode; whereas, propagating SPs require additional momentum matching (e.g. a prism), and LSPs are primarily excited in transmission. The choice of Kretschmann configuration over transmission mode is established for sensing purposes. Furthermore, chapter 2 presents the tunability of SPs by changing the azimuthal angle between the incident light wavevector and the x-axis of the nanohole array and by adjusting physical nanohole array parameters. The facile fabrication method allows for simple adjustment of nanohole array parameters which may be investigated in various optical configurations accordingly.

The development of a second generation (v2) instrument enabling surface plasmon resonance (SPR) spectroscopic measurements in the infrared (IR) range is described in chapter 3. The new design uses the optical train (optics and detector) within conventional FTIR spectrometers by confining dimensions of the accessory to space available within the sample compartment of the spectrometer. The v2 accessory builds upon knowledge gained from a previous version based on a modified commercial variable angle spectroscopic accessory, and it addresses observed limitations of the original design. The v2 accessory improves temporal stability and measurement acquisition speed, crucial to biomolecular binding studies, as well as optical flexibility which allows for investigation of novel plasmon-supporting materials. Different aspects of the accessory, including temporal stability, mechanical resilience and sensitivity to changes in refractive index of a sample are evaluated and presented.

In chapter 4, the significance of incorporating an adsorbate-metal bonding effect in the calculation of SP penetration depth is demonstrated in theory and in practice. The SP penetration depth is commonly determined from the observed response for adsorbate loading on gold surface plasmon resonance (SPR) substrates; however, changes in the SPR spectrum may originate from both changes in the effective refractive index near the metal surface and changes in the metal permittivity following covalent binding of the adsorbate layer. The bonding effect should be considered as well as the change in refractive index. Accordingly, the bonding effect is determined from the non-zero intercept of a SPR shift vs. adsorbate thickness calibration and incorporated into the calculation of penetration depth at various excitation wavelengths. Comparison of determinations of plasmon penetration depth with and without the bonding response for alkanethiolate-gold show a significant difference for a thiol monolayer adsorbate system. Additionally, plasmon penetration depth evaluated with bonding effect compensation exhibits greater consistency over different adsorbate thicknesses and better agreement with theory derived from Maxwell's equation, particularly for adsorbate thicknesses that are much smaller ($< 5\%$) than the plasmon penetration depth. The method is also extended to a more practically applicable polyelectrolyte multilayer adsorbate system and applied to the study of nanohole array SPR substrates.

Chapter 5 investigates the SPR characteristics and surface sensitivity of various nanohole arrays with the aim of tuning the parameters for optimal sensing capability. Nanohole arrays exhibit unique surface plasmon resonance (SPR) characteristics according to hole periodicity, diameter, and excitation wavelength (λ_{SPR}). Both the Bragg SPs arising from diffraction by the periodic holes and the traditional propagating SPs are characterized with emphasis on sensing capability of the propagating SPs. Several trends in bulk sensitivity and penetration depth are established, and the surface sensitivity is calculated from bulk sensitivity and penetration depth of the SPs for different analyte thicknesses. Increased accuracy and precision in penetration depth values is achieved by incorporating adsorbate effects on substrate permittivity according to the method developed in chapter 4. The optimal nanohole array conditions for highest

surface sensitivity were determined (820 nm periodicity, 0.27 diameter/periodicity, and λ_{SPR}=1550 nm), which demonstrated an increase in surface sensitivity for biosensing conditions over a continuous gold film at its optimal λ_{SPR} (1300 nm).

The interaction of surface plasmons supported on a nanohole array and a single nanoparticle affixed to an atomic force microscopy (AFM) probe is studied in chapter 6 for optimizing gap mode enhancement of the plasmonic field. Scanning probe microscopy controls the AFM probe position, and the location specific interaction of the single nanoparticle probe (SNP)-nanohole array surface plasmons is measured by darkfield surface plasmon resonance spectroscopy. Raster scanned darkfield imaging of the surface plasmons on the nanohole array is demonstrated, as well as image formation from measuring the SNP interaction at various (x.y) probe locations relative to the nanohole. Coupling of the nanoparticle to the nanohole array exhibits a maximum when the SNP resides within a nanohole, which resulted in a maximum SPR wavelength shift of 17 nm and an increase in scatter intensity. This technique may be expanded to mapping nanostructure coupling across three dimensions to determine optimal coupling conditions for use in biosensing and surface enhanced spectroscopy applications.

7.3 Implications

There are numerous studies on the transmission spectroscopy of nanohole arrays; however this dissertation presents one of the few studies in Kretschmann mode, and the first in the near infrared, where greater surface sensitivity was observed (maximum experimental surface sensitivity at $\lambda_{SPR} = 1550$ nm, Chapter 5). The observed trends in SP properties with nanohole array parameters were not all consistent with those presented by Live et. al. [54] in the visible wavelength range. The surface sensitivity was observed to decrease with diameter:periodicity (D/P) in chapter 5, whereas it increased with D/P in [54]. However, penetration depth decreased with D/P in both, so presumably, the observed difference is mainly an effect of the variable bulk sensitivity present in the NIR. Additionally, a similar increase over continuous gold was observed

for studies in the visible [54, 55] and NIR (chapter 5), however in the case studied in chapter 5, the wavelength was optimized. The IR-SPR instrument allowed for the vast experimental tunability of wavelength that may be utilized for other SPR studies in the NIR through the infrared with a change in optical materials accordingly.

NIR-SPR measurements with nanohole array SPR substrates offer a viable SPR system for increasing sensitivity. It accesses the increased sensitivity of higher wavelengths in an easily approachable system that fits into a commercial FTIR sample compartment. The nanosphere lithography fabrication method for the nanohole array substrates is facile and requires few resources in addition to those required for conventional thin film SPR. There are added advantages as discussed below and in chapter 1.5, and this technique maintains the characteristic SPR features that are important to the study of biomolecular binding mechanisms (real-time analysis, label-free detection, and high selectivity). Other techniques in addition to those investigated in this dissertation are available for increasing sensitivity over conventional thin film SPR, however exhibit some drawbacks. Long range surface plasmon (LRSP) resonance spectroscopy utilizes coupled SPs from opposite sides of a thin metal film between dielectrics and has demonstrated up to 20% increase in surface sensitivity. However, LRSP propagation length and penetration depth are much longer, and in some cases the the LRSPR spectral peak is much broader. More research is necessary to refine selection of dielectric support materials.[50, 51] Another technique involving phase modulation may double the sensitivity, however these setups involve interferometry which requires much more complicated analysis and optical components.[7]

An SPR sensor utilizing the coupling between nanohole arrays and nanoparticles has not be demonstrated in current literature. Other gap mode SPR sensors based on multiple nanoparticles or a nanoparticle and thin film have shown increased sensitivity over isolated structures. [1, 113, 114] Therefore, the superior sensitivity of the nanohole array, over both nanoparticles and thin films, suggests gap mode coupling capability with nanohole arrays would also surpass sensors based on these architectures. This dissertation presents the first empirical observations of SPM controlled

gap mode enhancement of more complex nanostructures and allows for optimization of positioning prior to sensing applications. The findings for greatest enhancement with the nanoparticle positioned within the nanohole are validated by agreement with theoretical studies on nanohole array-nanoparticle gap mode enhancement.[211, 210] The SPM-SPR instrument has great implications to the field for analysis of several structures in a similar manner. Furthermore, the SPM-SPR instrument may be used for combined Raman enhancement of SERS and TERS, which has only been previously studied for TERS measurements of benzenethiol on roughened ($>$ 2 nm) gold surfaces (SERS substrate) with a 10-fold enhancement observed at sharp edges.[226] The probable increased sensitivity of a nanosphere TERS probe with a nanohole array SERS substrate are attested by SERS experiments with static nanohole-nanoparticle pairs. A 100-fold improvement was demonstrated for this couple as compared to parallel SERS measurements on an isolated nanoparticle or nanohole [210], and SERS studies with nanohole arrays and nanoparticles where the gap distance is controlled by varied dielectric spacer thickness demonstrate up to 100$\times$ additional enhancement at optimized vs. arbitrary separation [227, 228]. Thereby, studies of increased SERS-TERS measurements with a TERS nanosphere probe-nanohole array are promising.

The technique developed in chapter 4 improved the consistency in the penetration depth value calculated at different adsorbate thicknesses from 41-1089% RSD (without binding effect) to 2-11% RSD (with binding effect). It also improved the experimental agreement with theory; from 360-5557% difference (without binding effect) to 5-14% difference (with binding effect). This modification to the Jung method [73] should be implemented when empirically determining penetration depth. It will increase the accuracy of assessing novel plasmonic materials and nanostructures, and increase the precision in adsorbate parameters calculated from the penetration depth value. The precision in the penetration depth value dictates the precision in subsequently derived values. Commonly, several parameters related to protein binding are derived from the penetration depth, including refractive index (η_a) or thickness (d).

Thickness is subsequently used in the calculation of surface coverage, θ (mlc/cm^2):

$$\theta = \mathrm{d}\rho \tag{7.1}$$

where ρ is the protein density. The surface coverage value is used to evaluate non-specific binding of interfering proteins in sample, and it is used to calculate the affinity constant, $\mathrm{K_{eq}}$, for solution phase analyte (A) binding to surface sites (S) on the SPR surface:[73, 77, 181]

$$\begin{gathered}[\mathrm{A}-\mathrm{S}] \leftrightarrow [\mathrm{A}][\mathrm{S}] \\ \mathrm{K_{eq}} = [\mathrm{A}-\mathrm{S}]/[\mathrm{A}][\mathrm{S}] = \theta\{(1-\theta)[\mathrm{A}]\}\end{gathered} \tag{7.2}$$

7.4 Future directions

Several of the studies presented in this dissertation may be expounded upon and implemented in various forms. The NIR-SPR instrument can be used for investigation of unconventional plasmonic materials (metal oxides, overlayers, graphene...). In particular, metal oxides have been measured on this instrument in collaboration with the Franzen research group. ["Infrared surface plasmon resonance on aluminum zinc oxide: relation to materials properties", manuscript in preparation] The tunability of penetration depth with excitation wavelength throughout the IR may also be used to measure larger analytes and unconventional attachment schemes (Figure 3.1). Additionally, the tunable λ_{SPR}, and therefore tunable l_d, could be used to probe analytes at different depths and compose an SPR depth profile. Additionally, the NIR-SPR instrument may be used for surface enhanced IR absorption spectroscopy. The SPR wavelength can be tuned to specific IR absorptions for enhancement.

The nanohole array SPR sensing substrates can replace conventional gold thin films for biosensing applications with the advantages of increased surface sensitivity, localization of field, reduced binding area (and potential absolute detection limit), and SP tunability. The detection limit may be further decreased in future endeavors by using data processing methods such as principal component analysis and singular value

decomposition to denoise the spectra, and by controlled binding to specific areas on the on the nanohole arrays. Increased binding efficiency in regions of greatest field intensity, i.e. hotspots, across the sensor surface may decrease detection limit. Studies by Correia-ledo et. al. [128] located the greatest field intensity on nanohole array surfaces with D/P= 0.63-0.54 and D/P<0.5 at the rim of hole and within the hole, respectively. Binding analyte to the sensor surface accordingly may increase sensitivity. Surface chemistry may be controlled such that biorecognition elements are attached primarily to the hotspots. Studies performed in transmission mode with increased binding within the hole achieved by flow through technology [149] or by blocking the planar surface such that binding occurred solely within the holes [148] showed improved sensitivity.

The TERS probe-nanohole interaction findings in chapter 6 can be expanded to optimize gap mode enhancement parameters, to perform empirical biosensing studies, and to investigate other optical excitation modes. SPM-SPR measurements acquired at various axial distances and with nanohole arrays of different hole diameters (Figure 7.1) can elucidate the greatest SPR enhancement between the structures in addition to the previously determined lateral position. An increase in SPR sensitivity to RI between the nanohole arrays and nanosphere is expected for axial distances within the gap mode coupling region. Gap mode enhanced SPR sensing is promising; however, currently, the main practical problem is highly controllable, reproducible fabrication of dimers.[62] The SNP probe-nanohole array setup overcomes this by fine control of the gap distance by the AFM feedback system. Highly localized, tip-enhanced SPR spectroscopy can be performed above the nanohole arrays. This lends to multiplexing and extremely low detection limit studies. The nanoholes can act as a nano-well plate, similar to studies by Storhoff et. al [61], and specific analyses within different holes can be performed with high lateral and spectral resolution. This setup can also be used for sensitive detection of interactions within a single hole. Similarly, combined SERS-TERS measurements can be performed as discussed in section 7.3. TERS probe-nanohole interaction with excitation in Kretschmann configuration could also be investigated with this instrument by adding prism based optics to the underside

of the Nanonics SPM system. This would expand the capability to probing interaction of the nanohole arrays in the most sensitive excitation regime so that findings can be applied to this optical mode.

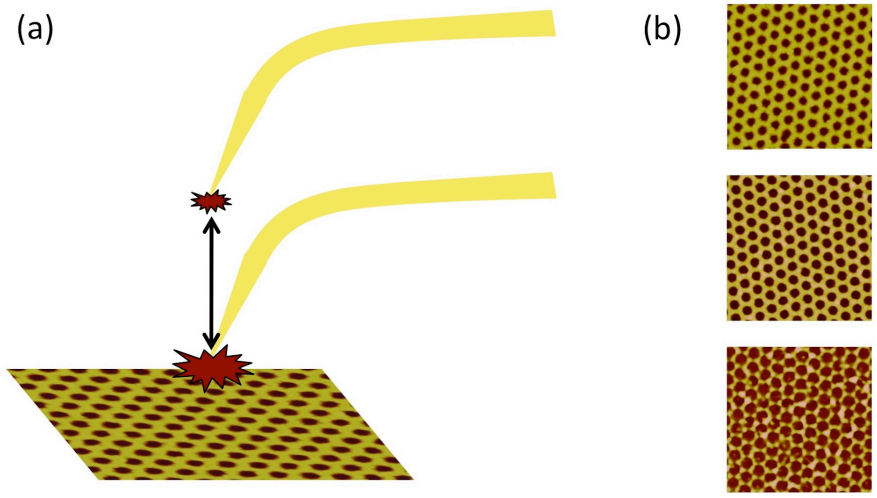

Figure 7.1: Toward mapping different TERS probe-nanohole array (a) distances and (b) hole diameters. The nanohole arrays in (b) have been focus ion beam milled (section 6.2.1) to different diameters ($229 \pm 5, 272 \pm 5, 369 \pm 6$ nm) and each has a duplicate structure with 89 ± 6 nm milled into the underlying glass substrate through the holes, so that the interaction above and below the hole may be observed.

Combined nanohole array-nanoparticle structures offer interesting sensor architectures without scanning probe microscope control as well. Nanoparticles attached within the hole can be used to amplify the SPR signal. A sensor which can switch the gap mode enhancement on and off with analyte adsorption would produce large responses. One such scheme could use nanoparticles attached within the hole of the nanohole arrays where the spacer layer attaching the two structures changes with analyte adsorption. In this case, a large signal would be transduced if the analyte adsorption correlated to a large distance (change or correlated to a length change from within gap mode enhancement region (d_{res}) to beyond the gap mode distance ($d > D$). One type that can be investigated is a "solenoid sensor" in which the analyte adsorbs into

and swells a selective polymer spacer layer between the nanoparticles and the bottom of the nanoholes (Figure 7.2(a)). Another type could be a sandwich assay in which the analyte adsorption and secondary antibody scaffold are spaced according to the optimal gap mode distance(Figure 7.2(b)). A sandwich assay with gold nanoparticles performed by Sharpe et. al. [136] demonstrated a 3-fold increase in sensitivity without gap distance optimization.

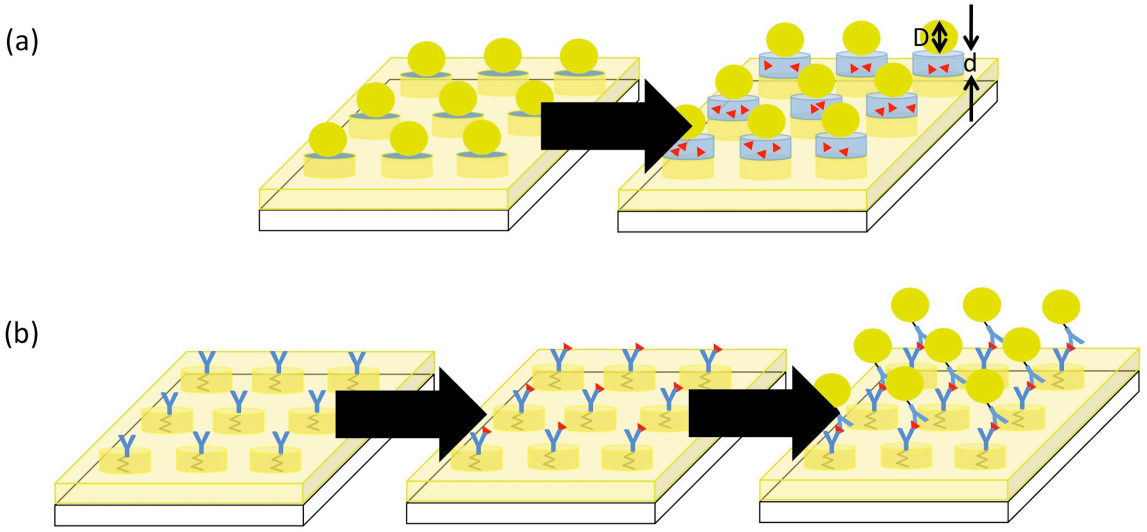

Figure 7.2: Proposed nanohole array-nanoparticle sensor with variable gap distance transduction system; (a) with swellable polymer and (b) with sandwich assay. The analyte is represented by red triangles. Gap mode enhancement occurs when $d < D$.

Additionally, other types of nanostructures affixed to the AFM probe tip for SPM-SPR measurements can be investigated. More complex nanostructures support various LSPs with geometry-specific electric field hotspots (refer to chapter 1.3 and figure 7.3). The shape specific hotspots illustrated in figure 7.3(b) were determined from FDTD and DDA modeling [88, 87] and likely lend to different levels of enhancement (sensitivity) and confinement (spatial resolution). Currently, Nanonics, Ltd. solely manufactures nanosphere functionalized AFM probes, but in-house fabrication of probes with different nanostructure geometries is possible. Colloidal nanofabrication techniques of various nanostructures is widely available [52, 62] and the nanoparticle

may be attached to sharply pointed fibers produced with a fiber puller (Figure 7.3(c)). FDTD analysis of the plasmonic fields would complement both this study and the previous studies, and future studies could be directed by preliminary FDTD analysis.

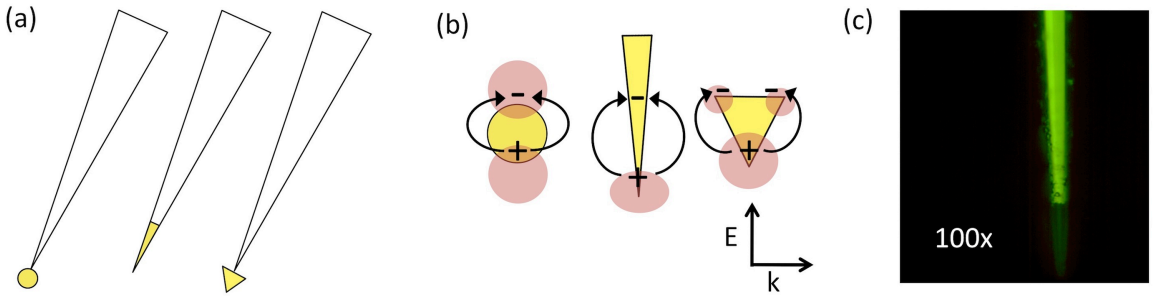

Figure 7.3: Illustration of (a) different SPM probe nanoparticle geometries and (b) corresponding SP field localization. (c) Micrograph of pulled fiber coated with gold for in house probe fabrication.

BIBLIOGRAPHY

[1] Jain, P. K.; El-Sayed, I. H.; El-Sayed, M. A. *Nano Today* **2007**, *2*, 18–29.

[2] Saenko, E. L.; Scandella, D.; Yakhyaev, A. V.; Greco, N. J. *Journal of Biological Chemistry* **1998**, *273*, 27918–27926.

[3] Wang, W.; Smith, D. K.; Moulding, K.; Chen, H. M. *Journal of Biological Chemistry* **1998**, *273*, 27438–27448.

[4] McDonnell, J. M. *Current Opinion in Chemical Biology* **2001**, *5*, 572–577.

[5] Scarano, S.; Scuffi, C.; Mascini, M.; Minunni, M. *Biosensors & Bioelectronics* **2010**, *26*, 1380–1385.

[6] Couture, M.; Zhao, S. S.; Masson, J. F. *Physical Chemistry Chemical Physics* **2013**, *15*, 11190–11216.

[7] Homola, J. *Chemical Reviews* **2008**, *108*, 462–493.

[8] Yu, D. H.; Blankert, B.; Vire, J. C.; Kauffmann, J. M. *Analytical Letters* **2005**, *38*, 1687–1701.

[9] Retra, K.; Geitmann, M.; Kool, J.; Smit, A. B.; de Esch, I. J. P.; Danielson, U. H.; Irth, H. *Analytical Biochemistry* **2010**, *407*, 58–64.

[10] Huber, W.; Mueller, F. *Current Pharmaceutical Design* **2006**, *12*, 3999–4021.

[11] Lakowicz, J. R.; Geddes, C. D.; Gryczynski, I.; Malicka, J.; Gryczynski, Z.; Aslan, K.; Lukomska, J.; Matveeva, E.; Zhang, J. A.; Badugu, R.; Huang, J. *Journal of Fluorescence* **2004**, *14*, 425–441.

[12] Larmour, I. A.; Graham, D. *Analyst* **2011**, *136*, 3831–3853.

[13] Gordon, R.; Brolo, A. G.; McKinnon, A.; Rajora, A.; Leathem, B.; Kavanagh, K. L. *Physical Review Letters* **2004**, *92*, year.

[14] Koerkamp, K. J. K.; Enoch, S.; Segerink, F. B.; van Hulst, N. F.; Kuipers, L. *Physical Review Letters* **2004**, *92*, year.

[15] Gordon, R.; Brolo, A. G.; Sinton, D.; Kavanagh, K. L. *Laser & Photonics Reviews* **2010**, *4*, 311–335.

[16] Strelniker, Y. M.; Stroud, D.; Voznesenskaya, A. O. *European Physical Journal B* **2006**, *52*, 1–7.

[17] Egorov, D.; Dennis, B. S.; Blumberg, G.; Haftel, M. I. *Physical Review B* **2004**, *70*, 4.

[18] Chowdhury, M. H.; Lindquist, N. C.; Lesuffleur, A.; Oh, S.-H.; Lakowicz, J. R.; Ray, K. *Journal of Physical Chemistry C* **2012**, *116*, 19958–19967.

[19] Kawata, S.; Inouye, Y.; Verma, P. *Nature Photonics* **2009**, *3*, 388–394.

[20] Zijlstra, P.; Chon, J. W. M.; Gu, M. *Nature* **2009**, *459*, 410–413.

[21] Hermann, C.; Kosobukin, V. A.; Lampel, G.; Peretti, J.; Safarov, V. I.; Bertrand, P. *Physical Review B* **2001**, *64*, 11.

[22] Mansuripur, M.; Zakharian, A. R.; Lesuffleur, A.; Oh, S. H.; Jones, R. J.; Lindquist, N. C.; Im, H.; Kobyakov, A.; Moloney, J. V. *Optics Express* **2009**, *17*, 14001–14014.

[23] Ferry, V. E.; Sweatlock, L. A.; Pacifici, D.; Atwater, H. A. *Nano Letters* **2008**, *8*, 4391–4397.

[24] Qiao, L.; Wang, D.; Zuo, L.; Ye, Y.; Qian, J.; Chen, H.; He, S. *Applied Energy* **2011**, *88*, 848–852.

[25] Barnes, W. L. *Philosophical Transactions of the Royal Society a-Mathematical Physical and Engineering Sciences* **2011**, *369*, 3431–3433.

[26] Masson, J. F.; Battaglia, T. M.; Khairallah, P.; Beaudoin, S.; Booksh, K. S. *Analytical Chemistry* **2007**, *79*, 612–619.

[27] Besselink, G. A. J.; Kooyman, R. P. H.; van Os, P.; Engbers, G. H. M.; Schasfoort, R. B. M. *Analytical Biochemistry* **2004**, *333*, 165–173.

[28] Wu, L. P.; Li, Y. F.; Huang, C. Z.; Zhang, Q. *Analytical Chemistry* **2006**, *78*, 5570–5577.

[29] Rojo, N.; Ercilla, G.; Haro, I. *Current Protein & Peptide Science* **2003**, *4*, 291–298.

[30] Lee, J. W.; Sim, S. J.; Cho, S. M.; Lee, J. *Biosensors & Bioelectronics* **2005**, *20*, 1422–1427.

[31] Choi, S. H.; Lee, J. W.; Sim, S. J. *Biosensors & Bioelectronics* **2005**, *21*, 378–383.

[32] Yi, X. Y.; Hao, Y. Q.; Xia, N.; Wang, J. X.; Quintero, M.; Li, D.; Zhou, F. M. *Analytical Chemistry* **2013**, *85*, 3660–3666.

[33] Goodrich, T. T.; Lee, H. J.; Corn, R. M. *Analytical Chemistry* **2004**, *76*, 6173–6178.

[34] Lee, H. J.; Li, Y.; Wark, A. W.; Corn, R. M. *Analytical Chemistry* **2005**, *77*, 5096–5100.

[35] Ladd, J.; Boozer, C.; Yu, Q. M.; Chen, S. F.; Homola, J.; Jiang, S. *Langmuir* **2004**, *20*, 8090–8095.

[36] Habauzit, D.; Chopineau, J.; Roig, B. *Analytical and Bioanalytical Chemistry* **2007**, *387*, 1215–1223.

[37] Wang, J.; Banerji, S.; Menegazzo, N.; Peng, W.; Zou, Q.; Booksha, K. S. *Talanta* **2011**, *86*, 133–141.

[38] Banerji, S.; Peng, W.; Kim, Y. C.; Menegazzo, N.; Booksh, K. S. *Sensors and Actuators B-Chemical* **2010**, *147*, 255–262.

[39] Menegazzo, N.; Boyne, D.; Bui, H.; Beebe, J., Thomas P.; Booksh, K. S. *Analytical Chemistry* **2012**, *84*, 5770–5777.

[40] Minunni, M.; Mascini, M. *Analytical Letters* **1993**, *26*, 1441–1460.

[41] Mouvet, C.; Harris, R. D.; Maciag, C.; Luff, B. J.; Wilkinson, J. S.; Piehler, J.; Brecht, A.; Gauglitz, G.; Abuknesha, R.; Ismail, G. *Analytica Chimica Acta* **1997**, *338*, 109–117.

[42] Gobi, K. V.; Tanaka, H.; Shoyama, Y.; Miura, N. *Sensors and Actuators B-Chemical* **2005**, *111*, 562–571.

[43] Bolduc, O. R.; Masson, J. F. *Analytical Chemistry* **2011**, *83*, 8057–8062.

[44] Schasfoort, R.; Tudos, A. *Handbook of Surface Plasmon Resonance*; RSC Publishing: Cambridge, UK, 2008.

[45] Homola, J. *Surface Plasmon Resonance Based Sensors*; Springer: Berlin, 2006.

[46] Vaisocherova, H.; Faca, V. M.; Taylor, A. D.; Hanash, S.; Jiang, S. *Biosensors & Bioelectronics* **2009**, *24*, 2143–2148.

[47] Campbell, K.; Huet, A.-C.; Charlier, C.; Higgins, C.; Delahaut, P.; Elliott, C. T. *Journal of Chromatography B-Analytical Technologies in the Biomedical and Life Sciences* **2009**, *877*, 4079–4089.

[48] Menegazzo, N.; Kegel, L. L.; Kim, Y. C.; Booksh, K. S. *Applied Spectroscopy* **2010**, *64*, 1181–1186.

[49] Menegazzo, N.; Kegel, L. L.; Kim, Y. C.; Allen, D. L.; Booksh, K. S. *Review of Scientific Instruments* **2012**, *83*, 095113.

[50] Nenninger, G. G.; Tobiska, P.; Homola, J.; Yee, S. S. *Sensors and Actuators B-Chemical* **2001**, *74*, 145–151.

[51] Wark, A. W.; Lee, H. J.; Corn, R. M. *Analytical Chemistry* **2005**, *77*, 3904–3907.

[52] Anker, J. N.; Hall, W. P.; Lyandres, O.; Shah, N. C.; Zhao, J.; Van Duyne, R. P. *Nature Materials* **2008**, *7*, 442–453.

[53] Shalabney, A.; Abdulhalim, I. *Laser & Photonics Reviews* **2011**, *5*, 571–606.

[54] Live, L. S.; Bolduc, O. R.; Masson, J. F. *Analytical Chemistry* **2010**, *82*, 3780–3787.

[55] Couture, M.; Live, L. S.; Dhawan, A.; Masson, J. F. *Analyst* **2012**, *137*, 4162–4170.

[56] Yonzon, C. R.; Jeoungf, E.; Zou, S. L.; Schatz, G. C.; Mrksich, M.; Van Duyne, R. P. *Journal of the American Chemical Society* **2004**, *126*, 12669–12676.

[57] Svedendahl, M.; Chen, S.; Dmitriev, A.; Kall, M. *Nano Letters* **2009**, *9*, 4428–4433.

[58] Otte, M. A.; Sepulveda, B.; Ni, W. H.; Juste, J. P.; Liz-Marzan, L. M.; Lechuga, L. M. *Acs Nano* **2010**, *4*, 349–357.

[59] Yu, F.; Ahl, S.; Caminade, A. M.; Majoral, J. P.; Knoll, W.; Erlebacher, J. *Analytical Chemistry* **2006**, *78*, 7346–7350.

[60] Karlsson, R. *Journal of Molecular Recognition* **2004**, *17*, 151–161.

[61] Storhoff, J. J.; Marla, S. S.; Bao, P.; Hagenow, S.; Mehta, H.; Lucas, A.; Garimella, V.; Patno, T.; Buckingham, W.; Cork, W.; Muller, U. R. *Biosensors & Bioelectronics* **2004**, *19*, 875–883.

[62] Jain, P. K.; El-Sayed, M. A. *Chemical Physics Letters* **2010**, *487*, 153–164.

[63] De Leebeeck, A.; Kumar, L. K. S.; de Lange, V.; Sinton, D.; Gordon, R.; Brolo, A. G. *Analytical Chemistry* **2007**, *79*, 4094–4100.

[64] Scarano, S.; Mascini, M.; Turner, A. P. F.; Minunni, M. *Biosensors & Bioelectronics* **2010**, *25*, 957–966.

[65] Bally, M.; Halter, M.; Voeroes, J.; Grandin, H. M. *Surface and Interface Analysis* **2006**, *38*, 1442–1458.

[66] Stewart, M. E.; Anderton, C. R.; Thompson, L. B.; Maria, J.; Gray, S. K.; Rogers, J. A.; Nuzzo, R. G. *Chemical Reviews* **2008**, *108*, 494–521.

[67] Otto, A. *Physica Status Solidi* **1968**, *26*, K99–+.

[68] Kretschmann, E.; Raether, H. *Zeitschrift Fur Naturforschung Part a-Astrophysik Physik Und Physikalische Chemie* **1968**, *A 23*, 2135–&.

[69] Maier, S. A. *Plasmonics: Fundamentals and Applications*; Springer Science and Business Media LLC: New York, 2007.

[70] Breault-Turcot, J.; Masson, J. F. *Analytical and Bioanalytical Chemistry* **2012**, *403*, 1477–1484.

[71] Debruijn, H. E.; Kooyman, R. P. H.; Greve, J. *Applied Optics* **1992**, *31*, 440–442.

[72] Berger, C. E. H.; Kooyman, R. P. H.; Greve, J. *Review of Scientific Instruments* **1994**, *65*, 2829–2836.

[73] Jung, L. S.; Campbell, C. T.; Chinowsky, T. M.; Mar, M. N.; Yee, S. S. *Langmuir* **1998**, *14*, 5636–5648.

[74] Chinowsky, T. M.; Soelberg, S. D.; Baker, P.; Swanson, N. R.; Kauffman, P.; Mactutis, A.; Grow, M. S.; Atmar, R.; Yee, S. S.; Furlong, C. E. *Biosensors & Bioelectronics* **2007**, *22*, 2268–2275.

[75] Zou, Q. J.; Menegazzo, N.; Booksh, K. S. *Analytical Chemistry* **2012**, *84*, 7891–7898.

[76] Haes, A. J.; Chang, L.; Klein, W. L.; Van Duyne, R. P. *Journal of the American Chemical Society* **2005**, *127*, 2264–2271.

[77] Battaglia, T. M.; Masson, J. F.; Sierks, M. R.; Beaudoin, S. P.; Rogers, J.; Foster, K. N.; Holloway, G. A.; Booksh, K. S. *Analytical Chemistry* **2005**, *77*, 7016–7023.

[78] Oshannessy, D. J.; Brighamburke, M.; Soneson, K. K.; Hensley, P.; Brooks, I. *Analytical Biochemistry* **1993**, *212*, 457–468.

[79] Steunou, S.; Chich, J.-F.; Rezaei, H.; Vidic, J. *Biosensors & Bioelectronics* **2010**, *26*, 1399–1406.

[80] Lyon, L. A.; Musick, M. D.; Natan, M. J. *Analytical Chemistry* **1998**, *70*, 5177–5183.

[81] Lyon, L. A.; Musick, M. D.; Smith, P. C.; Reiss, B. D.; Pena, D. J.; Natan, M. J. *Sensors and Actuators B-Chemical* **1999**, *54*, 118–124.

[82] Kubitschko, S.; Spinke, J.; Bruckner, T.; Pohl, S.; Oranth, N. *Analytical Biochemistry* **1997**, *253*, 112–122.

[83] Li, Y.; Lee, H. J.; Corn, R. M. *Analytical Chemistry* **2007**, *79*, 1082–1088.

[84] Mayer, K. M.; Hafner, J. H. *Chemical Reviews* **2011**, *111*, 3828–3857.

[85] Mie, G. *Annalen Der Physik* **1908**, *25*, 377–445.

[86] Kreibig, U.; Vollmer, M. *Optical Properties of Metal Clusters*; Springer: Berlin, 1995; Vol. 25.

[87] Liu, M. Z.; Guyot-Sionnest, P.; Lee, T. W.; Gray, S. K. *Physical Review B* **2007**, *76*, 235428.

[88] Kelly, K. L.; Coronado, E.; Zhao, L. L.; Schatz, G. C. *Journal of Physical Chemistry B* **2003**, *107*, 668–677.

[89] Nehl, C. L.; Hafner, J. H. *Journal of Materials Chemistry* **2008**, *18*, 2415–2419.

[90] Yang, W. H.; Schatz, G. C.; Vanduyne, R. P. *Journal of Chemical Physics* **1995**, *103*, 869–875.

[91] Sosa, I. O.; Noguez, C.; Barrera, R. G. *Journal of Physical Chemistry B* **2003**, *107*, 6269–6275.

[92] Shlager, K. L.; Schneider, J. B. *Ieee Antennas and Propagation Magazine* **1995**, *37*, 39–57.

[93] Gray, S. K.; Kupka, T. *Physical Review B 68*, 045415.

[94] Li, L. *J. Opt. Soc. Am. A* **1997**, *14*, 2758.

[95] Malinsky, M. D.; Kelly, K. L.; Schatz, G. C.; Van Duyne, R. P. *Journal of the American Chemical Society* **2001**, *123*, 1471–1482.

[96] Larsson, E. M.; Alegret, J.; Kall, M.; Sutherland, D. S. *Nano Letters* **2007**, *7*, 1256–1263.

[97] Kegel, L. L.; Menegazzo, N.; Booksh, K. S. *Analytical Chemistry* **2013**, *85*, 4875–4883.

[98] Petryayeva, E.; Krull, U. J. *Analytica Chimica Acta* **2011**, *706*, 8–24.

[99] Cobley, C. M.; Chen, J.; Cho, E. C.; Wang, L. V.; Xia, Y. *Chemical Society Reviews* **2011**, *40*, 44–56.

[100] Live, L. S.; Dhawan, A.; Gibson, K. F.; Poirier-Richard, H. P.; Graham, D.; Canva, M.; Vo-Dinh, T.; Masson, J. F. *Analytical and Bioanalytical Chemistry* **2012**, *404*, 2859–2868.

[101] Liu, Y.; Xu, S.; Li, H.; Jian, X.; Xu, W. *Chemical Communications* **2011**, *47*, 3784–3786.

[102] Stark, P. R. H.; Halleck, A. E.; Larson, D. N. *Methods* **2005**, *37*, 37–47.

[103] Lesuffleur, A.; Im, H.; Lindquist, N. C.; Lim, K. S.; Oh, S.-H. *Optics Express* **2008**, *16*, 219–224.

[104] Alleyne, C. J.; Kirk, A. G.; McPhedran, R. C.; Nicorovici, N.-A. P.; Maystre, D. *Optics Express* **2007**, *15*, 8163–8169.

[105] Dhawan, A.; Canva, M.; Vo-Dinh, T. *Optics Express* **2011**, *19*, 787–813.

[106] Chien, F. C.; Lin, C. Y.; Yih, J. N.; Lee, K. L.; Chang, C. W.; Wei, P. K.; Sun, C. C.; Chen, S. J. *Biosensors & Bioelectronics* **2007**, *22*, 2737–2742.

[107] Roh, S.; Kim, H.; Lee, B. *Journal of the Optical Society of America B-Optical Physics* **2011**, *28*, 1661–1667.

[108] Yu, C.; Irudayaraj, J. *Analytical Chemistry* **2007**, *79*, 572–579.

[109] Yu, C.; Nakshatri, H.; Irudayaraj, J. *Nano Letters* **2007**, *7*, 2300–2306.

[110] Wang, C.; Irudayaraj, J. *Small* **2008**, *4*, 2204–2208.

[111] Konopsky, V. N. *Optics Communications* **2000**, *185*, 83–93.

[112] Hayashi, S. *Near-Field Optics and Surface Plasmon Polaritons*; Springer-Verlag Berlin: Berlin, 2001; Vol. 81, pp 71–95.

[113] Jain, P. K.; Huang, W.; El-Sayed, M. A. *Nano Letters* **2007**, *7*, 2080–2088.

[114] Hao, E.; Schatz, G. C. *Journal of Chemical Physics* **2004**, *120*, 357–366.

[115] Teperik, T. V.; Popov, V. V.; de Abajo, F. J. G.; Abdelsalam, M.; Bartlett, P. N.; Kelf, T. A.; Sugawara, Y.; Baumberg, J. J. *Optics Express* **2006**, *14*, 1965–1972.

[116] Mustafa, D. E.; Yang, T. M.; Xuan, Z.; Chen, S. Z.; Tu, H. Y.; Zhang, A. D. *Plasmonics* **2010**, *5*, 221–231.

[117] Acimovic, S. S.; Kreuzer, M. P.; Gonzalez, M. U.; Quidant, R. *Acs Nano* **2009**, *3*, 1231–1237.

[118] Riskin, M.; Tel-Vered, R.; Lioubashevski, O.; Willner, I. *Journal of the American Chemical Society* **2009**, *131*, 7368–7378.

[119] Zhao, W.; Brook, M. A.; Li, Y. *Chembiochem* **2008**, *9*, 2363–2371.

[120] Sonnichsen, C.; Duch, A. C.; Steininger, G.; Koch, M.; von Plessen, G.; Feldmann, J. *Applied Physics Letters* **2000**, *76*, 140–142.

[121] Reinhard, B. M.; Sheikholeslami, S.; Mastroianni, A.; Alivisatos, A. P.; Liphardt, J. *Proceedings of the National Academy of Sciences of the United States of America* **2007**, *104*, 2667–2672.

[122] Du, L.; Zhang, X.; Mei, T.; Yuan, X. *Optics Express* **2010**, *18*, 1959–1965.

[123] Verma, P.; Yamada, K.; Watanabe, H.; Inouye, Y.; Kawata, S. *Physical Review B* **2006**, *73*, year.

[124] Hayazawa, N.; Ishitobi, H.; Taguchi, A.; Tarun, A.; Ikeda, K.; Kawata, S. *Japanese Journal of Applied Physics Part 1-Regular Papers Brief Communications & Review Papers* **2007**, *46*, 7995–7999.

[125] Homola, J. *Sensors and Actuators B-Chemical* **1997**, *41*, 207–211.

[126] Ebbesen, T. W.; Lezec, H. J.; Ghaemi, H. F.; Thio, T.; Wolff, P. A. *Nature* **1998**, *391*, 667–669.

[127] Brolo, A. G.; Arctander, E.; Gordon, R.; Leathem, B.; Kavanagh, K. L. *Nano Letters* **2004**, *4*, 2015–2018.

[128] Correia-Ledo, D.; Gibson, K. F.; Dhawan, A.; Couture, M.; Vo-Dinh, T.; Graham, D.; Masson, J. F. *Journal of Physical Chemistry C* **2012**, *116*, 6884–6892.

[129] Liu, Y. D.; Blair, S. *Optics Letters* **2003**, *28*, 507–509.

[130] Brolo, A. G.; Kwok, S. C.; Moffitt, M. G.; Gordon, R.; Riordon, J.; Kavanagh, K. L. *Journal of the American Chemical Society* **2005**, *127*, 14936–14941.

[131] Guo, P.-F.; Wu, S.; Ren, Q.-J.; Lu, J.; Chen, Z.; Xiao, S.-J.; Zhu, Y.-Y. *Journal of Physical Chemistry Letters* **2010**, *1*, 315–318.

[132] Rodriguez, K. R.; Shah, S.; Williams, S. M.; Teeters-Kennedy, S.; Coe, J. V. *Journal of Chemical Physics* **2004**, *121*, 8671–8675.

[133] Masson, J. F.; Murray-Methot, M. P.; Live, L. S. *Analyst* **2010**, *135*, 1483–1489.

[134] Reilly, T. H.; van de Lagemaat, J.; Tenent, R. C.; Morfa, A. J.; Rowlen, K. L. *Applied Physics Letters* **2008**, *92*, 243304.

[135] Krishnan, A.; Thio, T.; Kima, T. J.; Lezec, H. J.; Ebbesen, T. W.; Wolff, P. A.; Pendry, J.; Martin-Moreno, L.; Garcia-Vidal, F. J. *Optics Communications* **2001**, *200*, 1–7.

[136] Sharpe, J. C.; Mitchell, J. S.; Lin, L.; Sedoglavich, H.; Blaikie, R. J. *Analytical Chemistry* **2008**, *80*, 2244–2249.

[137] *Web of Knowledge*, http://wcs.webofknowledge.com, (Accessed August 26, 2013).

[138] Live, L. S.; Masson, J. F. *Journal of Physical Chemistry C* **2009**, *113*, 10052–10060.

[139] Live, L. S.; Murray-Methot, M. P.; Masson, J. F. *Journal of Physical Chemistry C* **2009**, *113*, 40–44.

[140] Thio, T.; Ghaemi, H. F.; Lezec, H. J.; Wolff, P. A.; Ebbesen, T. W. *Journal of the Optical Society of America B-Optical Physics* **1999**, *16*, 1743–1748.

[141] Lee, K. L.; Wang, W. S.; Wei, P. K. *Plasmonics* **2008**, *3*, 119–125.

[142] Alaverdyan, Y.; Hempe, E.-M.; Vamivakas, A. N.; E, H.; Maier, S. A.; Atatüre, M. *Applied Physics Letters* **2009**, *94*, 3536–3540.

[143] Genet, C.; Ebbesen, T. W. *Nature* **2007**, *445*, 39–46.

[144] Chang, S. H.; Gray, S. K.; Schatz, G. C. *Optics Express* **2005**, *13*, 3150–3165.

[145] Yin, L.; Vlasko-Vlasov, V. K.; Rydh, A.; Pearson, J.; Welp, U.; Chang, S. H.; Gray, S. K.; Schatz, G. C.; Brown, D. B.; Kimball, C. W. *Applied Physics Letters* **2004**, *85*, 467–469.

[146] Rindzevicius, T.; Alaverdyan, Y.; Dahlin, A.; Hook, F.; Sutherland, D. S.; Kall, M. *Nano Letters* **2005**, *5*, 2335–2339.

[147] Kelf, T. A.; Sugawara, Y.; Cole, R. M.; Baumberg, J. J.; Abdelsalam, M. E.; Cintra, S.; Mahajan, S.; Russell, A. E.; Bartlett, P. N. *Physical Review B* **2006**, *74*, 245415.

[148] Ferreira, J.; Santos, M. J. L.; Rahman, M. M.; Brolo, A. G.; Gordon, R.; Sinton, D.; Girotto, E. M. *Journal of the American Chemical Society* **2009**, *131*, 436–+.

[149] Eftekhari, F.; Escobedo, C.; Ferreira, J.; Duan, X.; Girotto, E. M.; Brolo, A. G.; Gordon, R.; Sinton, D. *Analytical Chemistry* **2009**, *81*, 4308–4311.

[150] McMahon, J. M. Ph.D. thesis, 2011.

[151] Jain, P. K.; El-Sayed, M. A. *Chemical Physics Letters* **2010**, *487*, 153–164.

[152] Haes, A. J.; Zhao, J.; Zou, S. L.; Own, C. S.; Marks, L. D.; Schatz, G. C.; Van Duyne, R. P. *Journal of Physical Chemistry B* **2005**, *109*, 11158–11162.

[153] Ji, J.; O'Connell, J. G.; Carter, D. J. D.; Larson, D. N. *Analytical Chemistry* **2008**, *80*, 2491–2498, Times Cited: 45.

[154] Haynes, C. L.; Van Duyne, R. P. *Journal of Physical Chemistry B* **2001**, *105*, 5599–5611.

[155] Murray, W. A.; Astilean, S.; Barnes, W. L. *Physical Review B* **2004**, *69*, 7.

[156] Murray-Methot, M. P.; Menegazzo, N.; Masson, J. F. *Analyst* **2008**, *133*, 1714–1721.

[157] Bolduc, O. R.; Live, L. S.; Masson, J. F. *Talanta* **2009**, *77*, 1680–1687.

[158] Garcia-Vidal, F. J.; Martin-Moreno, L.; Ebbesen, T. W.; Kuipers, L. *Reviews of Modern Physics 82*, 729–787.

[159] Lee, S. H.; Bantz, K. C.; Lindquist, N. C.; Oh, S. H.; Haynes, C. L. *Langmuir* **2009**, *25*, 13685–13693.

[160] Degiron, A.; Ebbesen, T. W. *Journal of Optics a-Pure and Applied Optics* **2005**, *7*, S90–S96.

[161] Genet, C.; van Exter, M. P.; Woerdman, J. P. *Optics Communications* **2003**, *225*, 331–336.

[162] Sarrazin, M.; Vigneron, J. P.; Vigoureux, J. M. *Physical Review B* **2003**, *67*, 085415.

[163] Parsons, J.; Hendry, E.; Burrows, C. P.; Auguie, B.; Sambles, J. R.; Barnes, W. L. *Physical Review B* **2009**, *79*, 4.

[164] Couture, M.; Liang, Y.; Poirier Richard, H.; Faida, R.; Peng, W.; Masson, J. F. *Nanoscale* **2013**.

[165] Ren, X. F.; Guo, G. P.; Huang, Y. F.; Wang, Z. W.; Guo, G. C. *Applied Physics Letters* **2007**, *90*, 161112.

[166] Huang, B.; Yu, F.; Zare, R. N. *Analytical Chemistry* **2007**, *79*, 2979–2983.

[167] Franzen, S. *Journal of Physical Chemistry C* **2008**, *112*, 6027–6032.

[168] Henzie, J.; Lee, J.; Lee, M. H.; Hasan, W.; Odom, T. W. *Annual Review of Physical Chemistry* **2009**, *60*, 147–165.

[169] Ju, L.; Geng, B. S.; Horng, J.; Girit, C.; Martin, M.; Hao, Z.; Bechtel, H. A.; Liang, X. G.; Zettl, A.; Shen, Y. R.; Wang, F. *Nature Nanotechnology* **2011**, *6*, 630–634.

[170] Masson, J. F.; Kim, Y. C.; Obando, L. A.; Peng, W.; Booksh, K. S. *Applied Spectroscopy* **2006**, *60*, 1241–1246.

[171] Lirtsman, V.; Golosovsky, M.; Davidov, D. *Journal of Applied Physics* **2008**, *103*, 014702.

[172] Frutos, A. G.; Weibel, S. C.; Corn, R. M. *Analytical Chemistry* **1999**, *71*, 3935–3940.

[173] *GWC Technologies*, http://www.gwcinstruments.com/gwcSPR100.htm, (Accessed July 23, 2012).

[174] Lide, D. *Handbook of Chemistry and Physics*, 90th ed.; CRC Press: Boca Raton, FL, 2009.

[175] Segelstein, D. J. M.Sc. thesis, University of Missouri: Kansas City, 1981.

[176] Johnson, P. B.; Christy, R. W. *Physical Review B* **1972**, *6*, 4370–4379.

[177] *Schott Glass*, http://www.us.schott.com/advanced_optics/english/our_products/materials/data_tools/index.html, (Accessed July 23, 2012).

[178] Im, H.; Sutherland, J. N.; Maynard, J. A.; Oh, S.-H. *Analytical Chemistry* **2012**, *84*, 1941–1947.

[179] Nordin, H.; Jungnelius, M.; Karlsson, R.; Karlsson, O. P. *Analytical Biochemistry* **2005**, *340*, 359–368.

[180] Bain, C. D.; Troughton, E. B.; Tao, Y. T.; Evall, J.; Whitesides, G. M.; Nuzzo, R. G. *Journal of the American Chemical Society* **1989**, *111*, 321–335.

[181] Masson, J. F.; Battaglia, T. M.; Cramer, J.; Beaudoin, S.; Sierks, M.; Booksh, K. S. *Analytical and Bioanalytical Chemistry* **2006**, *386*, 1951–1959.

[182] Nath, N.; Chilkoti, A. *Analytical Chemistry* **2004**, *76*, 5370–5378.

[183] Nusz, G. J.; Curry, A. C.; Marinakos, S. M.; Wax, A.; Chilkoti, A. *Acs Nano* **2009**, *3*, 795–806.

[184] Zhang, Y.; Terrill, R. H.; Bohn, P. W. *Journal of the American Chemical Society* **1998**, *120*, 9969–9970.

[185] Alloway, D. M.; Hofmann, M.; Smith, D. L.; Gruhn, N. E.; Graham, A. L.; Colorado, R.; Wysocki, V. H.; Lee, T. R.; Lee, P. A.; Armstrong, N. R. *Journal of Physical Chemistry B* **2003**, *107*, 11690–11699.

[186] Linnert, T.; Mulvaney, P.; Henglein, A. *Journal of Physical Chemistry* **1993**, *97*, 679–682.

[187] Haes, A. J.; Zou, S. L.; Schatz, G. C.; Van Duyne, R. P. *Journal of Physical Chemistry B* **2004**, *108*, 109–116.

[188] Bukasov, R.; Ali, T. A.; Nordlander, P.; Shumaker-Parry, J. S. *Acs Nano* **2010**, *4*, 6639–6650.

[189] Kedem, O.; Tesler, A. B.; Vaskevich, A.; Rubinstein, I. *Acs Nano* **2011**, *5*, 748–760.

[190] Palik, E. *Handbook of Optical Constants of Solids*; Academic Press: San Diego, 1998; Vol. I,II, and III.

[191] *Sopra Materials Database*, http://www.sopra-sa.com, (Accessed July 1, 2012).

[192] Seybold, J. S. *Introduction to RF Propagation*; John Wiley & Sons, Inc.: Hoboken, New Jersey, 2005.

[193] Xu, Z. X.; Hu, C. Y.; Hu, G. X. *Thin Solid Films* **2011**, *519*, 4324–4328.

[194] Ladam, G.; Schaad, P.; Voegel, J. C.; Schaaf, P.; Decher, G.; Cuisinier, F. *Langmuir* **2000**, *16*, 1249–1255.

[195] Ruths, J.; Essler, F.; Decher, G.; Riegler, H. *Langmuir* **2000**, *16*, 8871–8878.

[196] Sannomiya, T.; Balmer, T. E.; Heuberger, M.; Voros, J. *Journal of Physics D-Applied Physics* **2010**, *43*, 405302.

[197] Dejeu, J.; Membrey, F.; Diziain, S.; Bainier, C.; Spajer, M.; Charraut, D.; Foissy, A. *Journal of Physical Chemistry C* **2008**, *112*, 10531–10537.

[198] Nabok, A. V.; Hassan, A. K.; Ray, A. K. *Materials Science & Engineering C-Biomimetic and Supramolecular Systems* **1999**, *8-9*, 505–508.

[199] Ramsden, J. J.; Lvov, Y. M.; Decher, G. *Thin Solid Films* **1995**, *254*, 246–251.

[200] Buscher, K.; Graf, K.; Ahrens, H.; Helm, C. A. *Langmuir* **2002**, *18*, 3585–3591.

[201] Caruso, F.; Niikura, K.; Furlong, D. N.; Okahata, Y. *Langmuir* **1997**, *13*, 3422–3426.

[202] Buchner, K.; Ehrhardt, N.; Cahill, B. P.; Hoffmann, C. *Thin Solid Films* **2011**, *519*, 6480–6485.

[203] Lvov, Y.; Haas, H.; Decher, G.; Mohwald, H.; Kalachev, A. *Journal of Physical Chemistry* **1993**, *97*, 12835–12841.

[204] Shiratori, S. S.; Rubner, M. F. *Macromolecules* **2000**, *33*, 4213–4219.

[205] Prikulis, J.; Hanarp, P.; Olofsson, L.; Sutherland, D.; Kall, M. *Nano Letters* **2004**, *4*, 1003–1007.

[206] Tellez, G. A. C.; Ahmed, A.; Gordon, R. *Applied Physics a-Materials Science & Processing* **2012**, *109*, 775–780.

[207] Hu, M.; Ghoshal, A.; Marquez, M.; Kik, P. G. *Journal of Physical Chemistry C* **2010**, *114*, 7509–7514.

[208] Gunnarsson, L.; Bjerneld, E. J.; Xu, H.; Petronis, S.; Kasemo, B.; Kall, M. *Applied Physics Letters* **2001**, *78*, 802–804.

[209] Muskens, O. L.; Giannini, V.; Sanchez-Gil, J. A.; Rivas, J. G. *Optics Express* **2007**, *15*, 17736–17746.

[210] Wei, H.; Hakanson, U.; Yang, Z. L.; Hook, F.; Xu, H. X. *Small* **2008**, *4*, 1296–1300.

[211] He, M. D.; Gong, Z. Q.; Li, S.; Luo, Y. F.; Liu, J. Q.; Chen, X. S.; Lu, W. *Journal of Applied Physics* **2010**, *108*, 6.

[212] Fischer, U. C.; Pohl, D. W. *Physical Review Letters* **1989**, *62*, 458–461.

[213] Olk, P.; Renger, J.; Wenzel, M. T.; Eng, L. M. *Nano Letters* **2008**, *8*, 1174–1178.

[214] Garcia-Etxarri, A.; Romero, I.; de Abajo, F. J. G.; Hillenbrand, R.; Aizpurua, J. *Physical Review B* **2009**, *79*, 125439.

[215] Hakanson, U.; Agio, M.; Kuhn, S.; Rogobete, L.; Kalkbrenner, T.; Sandoghdar, V. *Physical Review B* **2008**, *77*, 155408.

[216] Docter, M. W.; Young, I. T.; Piciu, O. M.; Bossche, A.; Alkemade, P. F. A.; van den Berg, P. M.; Garini, Y. *Optics Express* **2006**, *14*, 9477–9482.

[217] Branagan, S. P.; Bohn, P. W. *Optics Express* **2009**, *17*, 18995–19005.

[218] Ctistis, G.; Patoka, P.; Wang, X.; Kempa, K.; Giersig, M. *Nano Letters* **2007**, *7*, 2926–2930.

[219] Gao, H. W.; Henzie, J.; Odom, T. W. *Nano Letters* **2006**, *6*, 2104–2108.

[220] Lezec, H. J.; Degiron, A.; Devaux, E.; Linke, R. A.; Martin-Moreno, L.; Garcia-Vidal, F. J.; Ebbesen, T. W. *Science* **2002**, *297*, 820–822.

[221] Deckman, H. W.; Dunsmuir, J. H. *Applied Physics Letters* **1982**, *41*, 377–379.

[222] Haginoya, C.; Ishibashi, M.; Koike, K. *Applied Physics Letters* **1997**, *71*, 2934–2936.

[223] Ciddor, P. E. *Applied Optics* **1996**, *35*, 1566–1573.

[224] Jain, P. K.; Eustis, S.; El-Sayed, M. A. *Journal of Physical Chemistry B* **2006**, *110*, 18243–18253.

[225] Li, X.; Tamada, K.; Baba, A.; Knoll, W.; Hara, M. *Journal of Physical Chemistry B* **2006**, *110*, 15755–15762.

[226] Zhang, W.; Cui, X.; Yeo, B.-S.; Schmid, T.; Hafner, C.; Zenobi, R. *Nano Letters* **2007**, *7*, 1401–1405.

[227] Wen, X. L.; Xi, Z.; Jiao, X. J.; Yu, W. H.; Xue, G. S.; Zhang, D. G.; Lu, Y. H.; Wang, P.; Blair, S.; Ming, H. *Plasmonics* **2013**, *8*, 225–231.

[228] Wen, X. L.; Yi, M. F.; Zhang, D. G.; Wang, P.; Lu, Y. H.; Ming, H. *Nanotechnology* **2011**, *22*, 085203.

Appendix A

LIST OF ACRONYMS AND SYMBOLS

A.1 Acronyms

D: diameter

LRSP: long range surface plasmon

LSP: localized surface plasmon

P: periodicity

PEM: polyelectrolyte multilayer

RD: relative deviation

RSD: relative standard deviation

SP: surface plasmon

SPR: surface plasmon resonance

A.2 Symbols

k_{sp}: SP wave vector

λ_{SPR}: SPR wavelength

$\Delta\lambda_{\mathrm{SPR}}$: SPR wavelength shift

θ_{inc}: incident angle

l_d: penetration depth

m: Bulk sensitivity, $\Delta\lambda_{\mathrm{SPR}}$ for given refractive index ($\sim$nm/RIU)

m_{surf}: Surface sensitivity

$\Delta\lambda_{\mathrm{SPR},\epsilon m}$: SPR wavelength shift due to change in complex permittivity of metal

ϵ: Complex permittivity

ϵ_m: Complex permittivity of metal

ϵ_s: Complex permittivity of sample

η: Refractive index

η_a: Refractive index of adsorbate

η_s: Refractive index of solution or sample

η_{PEM}: Refractive index of polyelectrolyte multilayer

d: adsorbate layer thickness or gap distance

ϕ: azimuthal angle

Appendix B

CURRICULUM VITAE

Profile

- Adept at advanced optical spectroscopy and material characterization techniques, quantitative/statistical evaluation and interpretation of analysis, and dissemination of results
- Broad experience in analytical techniques (including FTIR, Raman, SPR, GC-MS, HPLC, fluorescence, electrochemistry, NIR, AAS, XPS, SEM, TEM, AFM, etc..) and sample preparation techniques
- Creative problem-solver toward growth and application of analytical techniques and instrumentation
- Motivated team member and leader with demonstrated aptitude for multitasking, effective communication, and plan conceptualization

Education

Ph.D. in Analytical Chemistry
University of Delaware, Newark, DE
Graduation date: September 2013, GPA: 3.97/4.00
Dissertation title: "Characterization of surface plasmon resonance (SPR) active nanohole array sensing platforms: Development and application of novel instrumentation and methodology"

B.S. in Chemistry
Millersville University, Millersville, PA
Graduation Date: May 2008, with Honors, GPA: 3.71/4.00, Major GPA: 3.78/4.00
Thesis title: "Electrochemical characterization of poly(terphenylene vinylene)"

Technical Skills

- Analytical techniques: spectroscopy (surface plasmon resonance, infrared, Raman, UV-Vis, fluorescence, AAS, XPS), surface and tip enhancement methods, GC-MS, HPLC, electrochemistry, SEM, TEM, and AFM
- Material characterization: atomic force microscopy, electron microscopy, and electroanalytical methods

- Sample preparation: wet chemistry, sputter deposition, nanosphere lithography, thin film fabrication, thermal evaporation, photolithography, plasma etching, electrochemistry, and metallic nanostructure synthesis
- Quantitative/statistical data analysis
- Computer applications: Microsoft Office, MATLAB, Coreldraw, LaTeX, basic Adobe Illustrator, basic Labview, various instrumental control interfaces and AFM analysis software

Additional Skills

- Proficient facilitation, support, and cooperative collaboration of/with laboratory coworkers and interdisciplinary associates
- Strong verbal and written communication skills
- Leadership in research and educational settings
- Writing and editing scientific papers and proposals
- Self motivated, goal oriented plan development
- Critical thinking
- Organizational skills and adaptability leading to high efficiency

Research Experience

Doctoral Research, University of Delaware, Newark, DE
Advisor: Karl Booksh, Ph.D., August 2008-Present
Characterized nanostructured Surface Plasmon Resonance (SPR) sensing platforms for use as biosensors; Developed SPR instrumentation and methods for improved spatial and spectral resolution (published in Applied Spectroscopy and patent granted); Extensive use of various optical (FTIR, SPR, Raman, UV-Vis spectroscopies) and physical (atomic force and electron microscopies) characterization methods; Utilized quantitative/statistical data analysis; Executed lab equipment maintenance, troubleshooting, and training; Effectively planned for efficient research on concurrent project goals; Presented at various regional and national meetings (7 presentations, awarded for FACSS poster presentation)

Research Experience for Undergraduates Program, University of Oregon, Eugene, OR
Advisor: Mark Lonergan, Ph.D., June 2007-August 2007
Electrochemically characterized anionic poly(terphenylene vinylene) ($PTPV_a$) to determine potential for usage as a light emitting electrochemical cell; Investigated electrochemical doping conditions and subsequent conductivity of $PTPV_a$ thin films in various electrode architectures; Presented at ACS National Meeting and Millersville University Chemistry Department seminar; Wrote undergraduate honors thesis

Honors Research, Millersville University, Millersville, PA
Advisor: Robert Wismer, Ph.D., January 2007-May 2007
Investigated an inexpensive, homebuilt conductivity meter for potential usage as a

water purity test device; Self-driven goals with results presented in weekly progress reports; Adapted device and wrote procedure for undergraduate physical chemistry lab

Research and Development Internship, Stoner, Inc., Quarryville, PA
Mentor: Robert Sweger, Ph.D., May 2006-August 2006
Product research and development internship at cleaner, lubricant, and coating chemical company; Supported numerous production activities and product improvements; Discussed and presented progress, findings, and future direction in weekly research meetings with technical team

Teaching Experience

Laboratory Teaching Assistant, University of Delaware, Newark, DE, Spring/Fall 2008-2013
Instructed students in quantitative analysis and instrumental analysis laboratory courses; Facilitated understanding and use of proper lab technique and instrumentation (FTIR, UV-Vis, GC-MS, HPLC, fluorescence, electrochemistry, NIR, AAS); Effective communication and organization of topics supported by student evaluations at end of semester; 4 courses, 8-15 students

Chemistry Tutor, Millersville University, Millersville, PA, Spring/Fall 2005-2006
Instructed and supported small groups of students in general and organic chemistry; Addressed broad course topics and individual problems from students; 2h/week, 1-8 students

Professional Service

Mentoring Undergraduate Research Assistants, University of Delaware, 2010-2013
Guided proficiency and confidence in undergraduate students in laboratory research techniques and aspects of ongoing projects including spectroscopic methods, fiber optic sensor fabrication, nanostructure fabrication, and surface plasmon resonance spectroscopy

Instrument Training and Maintenance, University of Delaware, 2010-2013
Trained and worked with incoming graduate students and interdisciplinary (Material Science, Biology, Geology, Physics) researchers on Raman microscopy, FTIR (transmission, reflection, attenuated total reflectance) spectroscopy, custom surface plasmon resonance spectroscopy, and atomic force microscopy instruments; Involved heavily in the maintenance of optimal working condition of the instruments

Chemistry and Biochemistry Student Recruitment, University of Delaware, 2009-2013

Discussed general and specific aspects of graduate life and research with prospective students in large group and individual visits; Analytical division representative in student-lead forum addressing questions from prospective students; Worked with new graduate students to initiate research projects

Peer Article Review, *Analytical Letters*, August 2012

Lab Technique Demonstration, University of Delaware, July 2009 and 2010
Demonstrated and presented sputtering of gold and FTIR of polymers to groups of high school students as part of Historically Black Colleges and Universities Undergraduates Program (HBCU-UP) in preparation for further study in STEM fields

Awards & Honors

- Federation of Analytical Chemistry and Spectroscopy Societies Student Poster Award at SciX, Oct. 2012
- Professional Development Award, awarded by University of Delaware for participation in professional conferences, award based on written proposal, Oct. 2012
- Great Rivers Affiliate American Heart Association (AHA) Predoctoral Fellowship awarded by the Research Committee of the AHA based on evaluation of the investigator, sponsor/training plan, and written research proposal, 25.9% success rate for 2009 applicants, 2009-2011
- Undergraduate American Institute of Chemists Award in recognition of "demonstrated ability, leadership, and professional promise", 300 awardees in 2008, May 2008
- University and Departmental Honors by completion of honors thesis and required coursework, May 2008
- Amos L. Schopf Endowment Scholarship, 2004-2008

Publications

Published

Kegel, L. L., Menegazzo, N., Booksh, K. S., "Adsorbate-metal bond effect on empirical determination of surface plasmon penetration depth", Analytical Chemistry, 2013, 85, 4875-4883. DOI:10.1021/ac400006j.

Kim, Y.-C., Cramer, J., Battaglia, T., Jordan, J. A., Banerji, S., Wei Peng, W., **Kegel, L. L.**, Booksh, K. S.,"Investigation of In Situ Surface Plasmon Resonance Spectroscopy for Environmental Monitoring in and around Deep-Sea Hydrothermal Vents", Analytical Letters, 2013, 46, 1607-1617. DOI:10.1080/00032719.2012.757701.

Kegel, L. L.*, Menegazzo, N.*, Kim, Y.-C., Allen, D., Booksh, K. S., "Adaptable infrared surface plasmon resonance spectroscopy accessory", Rev. Sci. Instr., 2012, 83/9, 095113. DOI: 10.1063/1.4752463. *Denotes equal contribution.

Menegazzo, N., **Kegel, L. L.**, Kim, Y. C.; Booksh, K. S., "Characterization of a variable angle reflectance FT-IR accessory modified for surface plasmon resonance spectroscopy", Appl. Spectrosc. 2010, 64, 1181-1186. DOI: 10.1366/000370210792973451.

Recently Submitted

Kegel, L. L., Boyne, D., Booksh, K. S., "Tailoring nanohole array sensing substrates for optimizing surface sensitivity", Analytical Chemistry, submitted.

Kegel, L. L., Kim, S.-S., Mizaikoff, B., Kranz, C., Booksh, K. S., "Interaction of TERS probe-nanohole array localized surface plasmons", Plasmonics, submitted.

Guske, J., **Kegel, L.**, Menegazzo, N., Sachet, E., Booksh, K., Maria, J.-P., Franzen, S., "Infrared surface plasmon resonance on aluminum zinc oxide: relation to materials properties", Surf. Sci., submitted.

Zou, Q.-J., Menegazzo, N., **Kegel, L. L.**, Booksh, K. S.,"Electrografted Diazonium Salt Layers for Antifouling on the Surface of SPR Biosensors", Anal. Chem., in revisions.

Patents

Booksh, K. S.; Menegazzo, N.; Kim, Y-C.; **Kegel, L. L.**; Derrick, A.; "Apparatus and method for performing surface plasmon resonance (SPR) with an infrared (IR) spectrometer", PCT/US2011/054716.

Presentations

"Tailoring nanostructure surface plasmons for optimal sensor substrate selection", PITTCON, Philadelphia, PA (March 2013). Talk.

"Tailoring surface plasmon resonance wavelength and penetration depth", EAS, Somerset, NJ (Nov. 2012). Talk.

"Evaluating plasmonic substrates by improved surface plasmon penetration depth calculations and extended vis-NIR wavelength range", SciX, Kansas City, MO (Oct. 2012). Poster.

"Tailoring nanostructure surface plasmons for optimal sensor substrate selection", ACS, Philadelphia, PA (August 2012). Talk.

"Adsorbate-gold bond effect on empirical surface plasmon penetration depth in the near infrared", MARMACS, (June 2012). Talk.

"Near infrared spectroscopy of localized and propagating surface plasmon resonance in nanohole arrays" FACSS, Raleigh, NC (Oct. 2010) Poster.

"Tuning of nanohole array surface plasmon resonance wavelength by varying nanohole diameter and array periodicity", MARMACS (April 2010). Poster.

"Electrical characterization of anionic poly(terphenylenevinylene)", ACS, New Orleans, LA (April 2008). Poster.

Professional Affiliations

- Member, Society of Applied Spectroscopy (SAS), 2010-Present
- Member, American Chemical Society, 2007-Present

Selected Relevant Graduate Coursework

- Chemometrics, Spring 2009
- Surface Analysis, Spring 2009
- Practical Electron Microscopy, Spring 2009
- Electroanalytical Chemistry, Fall 2008
- Chemical Sensors, Fall 2008

Appendix C

PERMISSION FOR MATERIAL REPRINT

Portions of chapter 3 are modified or reprinted with permission from "Menegazzo, N.*; Kegel, L. L.*; Kim, Y. C.; Allen, D. L.; Booksh, K. S. Review of Scientific Instruments 2012, 83, 095113." Copyright 2012, AIP Publishing LLC. DOI:10.1063/1.4752463

Portions of chapter 4 are reproduced in part with permission from "Kegel, L. L.; Menegazzo, N.; Booksh, K. S. Analytical Chemistry 2013, 85, 4875-4883". Copyright 2013, American Chemical Society. DOI: 10.1021/ac400006j

Portions of chapters 6 and 5 are publications in consideration and should await publication before dissemination with UMI.